Wright State University

CORE Scholar

Browse all Theses and Dissertations | Theses and Dissertations

2012

Characterization of Ceramic Matrix Composite Materials using Millimeter-Wave Techniques

Matthew Lee Bischoff
Wright State University

Follow this and additional works at: https://corescholar.libraries.wright.edu/etd_all

Part of the Physics Commons

Repository Citation

Bischoff, Matthew Lee, "Characterization of Ceramic Matrix Composite Materials using Millimeter-Wave Techniques" (2012). *Browse all Theses and Dissertations*. 683.
https://corescholar.libraries.wright.edu/etd_all/683

This Thesis is brought to you for free and open access by the Theses and Dissertations at CORE Scholar. It has been accepted for inclusion in Browse all Theses and Dissertations by an authorized administrator of CORE Scholar. For more information, please contact library-corescholar@wright.edu.

CHARACTERIZATION OF CERAMIC MATRIX COMPOSITE MATERIALS USING MILLIMETER-WAVE TECHNIQUES

A thesis submitted in partial fulfillment of the
requirements for the degree of
Master of Science

By

MATTHEW LEE BISCHOFF
B.S., The University of Maine, 2002
M.S., Purdue University, 2006

2012
Wright State University

WRIGHT STATE UNIVERSITY

GRADUATE SCHOOL

November 19, 2012

I HEREBY RECOMMEND THAT THE THESIS PREPARED UNDER MY SUPERVISION BY Matthew Lee Bischoff ENTITLED Characterization of Ceramic Matrix Composite Materials Using Millimeter-Wave Techniques BE ACCEPTED IN PARTIAL FULFILLMENT OF THE REQUIREMENTS FOR THE DEGREE OF Master of Science.

Douglas T. Petkie, Ph.D.
Thesis Director

Douglas T. Petkie, Ph.D.
Chair, Department of Physics

Committee on Final Examination

Douglas T. Petkie, Ph. D.

Jason A. Deibel, Ph.D.

Gary Farlow Ph.D.

Andrew Hsu, Ph.D.
Dean, Graduate School

COPYRIGHT BY
MATTHEW L. BISCHOFF
2012

ABSTRACT

Bischoff, Matthew L. M.S. Department of Physics, Wright State University, 2012.
Characterization of Ceramic Matrix Composite Materials using Millimeter-wave Techniques.

This thesis describes studies that were carried out on Ceramic Matrix Composite (CMC) materials. These materials were provided by the Air Force Research Laboratory for evaluation in the millimeter-wave frequency region with the goal of developing Non-Destructive Evaluation techniques. This thesis centers on describing the measured reflections from an Oxide/Oxide and SiC/SiNC CMC materials. Models were derived from the Fresnel equations to account for the reflected and transmitted waves in these materials. System models were developed to describe the power coupling of the spectra measured in three separate measurement systems. Using these models the complex index of refraction was determined for the Oxide/Oxide material, and the front surface reflectance was determined for the SiC/SiNC material. A discussion of changes in sample optical properties due to material fatiguing will be included. This document will conclude with the complete spectra and statistical analyses of the Oxide/Oxide, and SiC/SiNC materials at 140-220, and 585-630 GHz.

TABLE OF CONTENTS

Section	Title	Page
I.	INTRODUCTION AND PURPOSE……………………………………..	1
	1.1. Introduction to CMC materials……………………………………	1
	1.2. Initial Results……………………………………………………	2
II.	MEASUREMENT SYSTEMS……………………………………..…..	4
	2.1. Literature Review of Various Characterization Systems…………...	4
	2.2. Measurement Systems Used………………..……………………...	7
III.	MODELING…………………………………………………………..	15
	3.1. Material Modeling………………………………………………..	15
	3.2. System Model…………………………………………………….	20
	3.3. Combined Models………………………………………………..	24
IV.	MEASURMENT TECHNIQUES……………………………………….	26
	4.1. Error Propagation………………………………………………...	28
	4.2. SiC/SiNC Measurements………………………………………...	32
	4.3. Oxide/Oxide Measurements……………………………………...	33
V.	MEASUREMENT RESULTS…………………………………………..	41
	5.1. SiC/SiNC Results………………………………………………...	43
	5.2. Oxide/Oxide Results……………………………………………..	45
	5.3. Discussion………………………………………………………..	48
VI.	CONCLUSION……………………………………………………...	49
	APPENDICES………………………………………………………	52
	Appendix A………………………………………………………..	52
	Appendix B………………………………………………………	71
	BIBLIOGRAPHY…………………………………………………...	75

LIST OF FIGURES

Figure	Title	Page
1.	Image of C/SiC, SiC/SiNC, and Oxide/Oxide CMC………………………	1
2.	Initial transmission results…………………………………………………	3
3.	Reflectance/Transmittance System…..………………………………......	9
4.	Beam Waist Measurements….……………………………………………	11
5.	CW400 Beam Waist Measurement…………….......................................	12
6.	Multiple Reflection/Transmission Wave……………………………......	16
7.	Modeled and Measured Data……………………………………………	19
8.	Surface of Stressed and Baseline Samples………………………………	20
9.	Simple Optical Transmission System…………………………………...	21
10.	Simple Transmission System Results…………………………………...	23
11.	Metal References………………………………………………………....	29
12.	Reflectance of Metal References from 200 & 600 GHz Systems…………	30
13.	Raw Reflectance of SiC/SiNC sample at 200 & 600 GHz………………...	32
14.	Calculated Reflectance of SiC/SiNC sample………………………………	32
15.	Finalized Reflectance of SiC/SiNC sample……………………………..	33
16.	Raw Measures of Oxide/Oxide sample at 200 & 600 GHz…………..….	34
17.	Calculated Measures of Oxide/Oxide sample…………………………...	34
18.	Finalized Reflectance of Oxide/Oxide sample…………………………..	35
19.	CW400 Oxide/Oxide Measure System Power and FFT…………………...	36
20.	Measured Transmittance of Oxide/Oxide from CW400…………………...	37
21.	Absorption of Oxide/Oxide……………………………………………....	38
22.	Fitting of Oxide/Oxide CW400 Measurements……………………………	43
23.	Baseline Reflectance of SiC/SiNC samples……………………………..	44
24.	Stressed Reflectance of SiC/SiNC samples……………………………..	44
25.	T-Values for SiC/SiNC Hypothesis testing………………………………..	47
26.	Oxide/Oxide Transmittance Features…………………………………….	48
27.	Oxide/Oxide Transmittance Features…………………………………….	48
A-1.	Heat-treated SiC/SiNC 200 GHz 1………………………………………..	53
A-2.	Heat-treated SiC/SiNC 200 GHz 2………………………………………..	53

LIST OF FIGURES cont.

Figure	Title	Page
A-3.	Heat-treated SiC/SiNC 600 GHz…………………………………….…...	53
A-4.	2nd Heat-treated SiC/SiNC 600 GHz…………………………….…...	54
A-5.	Dwell-treated SiC/SiNC 600 GHz ……………………………….....	54
A-6.	Strain-treated SiC/SiNC 200 GHz 1……………………………….....	55
A-7.	Strain-treated SiC/SiNC 200 GHz 2……………………………….....	55
A-8.	Strain-treated SiC/SiNC 600 GHz……………………………….…...	55
A-9.	Baseline SiC/SiNC 29 200 GHz………………………………………...	56
A-10.	Baseline SiC/SiNC 30 200 GHz ……………………………………..…	56
A-11.	Baseline SiC/SiNC 31 200 GHz ……………………………………..…	56
A-12.	Baseline SiC/SiNC 32 200 GHz ……………………………………..…	57
A-13.	Baseline SiC/SiNC 33 200 GHz 1…………………………………………	57
A-14.	Baseline SiC/SiNC 33 200 GHz 2…………………………………………	57
A-15.	Baseline SiC/SiNC 33 200 GHz 3…………………………………………	58
A-16.	Baseline SiC/SiNC 34 200 GHz 1…………………………………………	58
A-17.	Baseline SiC/SiNC 34 200 GHz 2…………………………………………	58
A-18.	Baseline SiC/SiNC 34 200 GHz 3…………………………………………	59
A-19.	Baseline SiC/SiNC 35 200 GHz 1…………………………………………	59
A-20.	Baseline SiC/SiNC 35 200 GHz 2…………………………………………	59
A-21.	Baseline SiC/SiNC 35 200 GHz 3…………………………………………	60
A-22.	Baseline SiC/SiNC 35 600 GHz ………………………………………..	60
A-23.	Baseline SiC/SiNC 36 200 GHz 1…………………………………………	60
A-24.	Baseline SiC/SiNC 36 200 GHz 2…………………………………………	61
A-25.	Baseline SiC/SiNC 36 200 GHz 3…………………………………………	61
A-26.	Baseline SiC/SiNC 37 200 GHz 1…………………………………………	61
A-27.	Baseline SiC/SiNC 37 200 GHz 2…………………………………………	62
A-28.	Baseline SiC/SiNC 37 200 GHz 3…………………………………………	62
A-29.	Baseline SiC/SiNC 37 600 GHz ……………………………………….	62
A-30.	Baseline SiC/SiNC 38 200 GHz 1…………………………………………	63
A-31.	Baseline SiC/SiNC 38 200 GHz 2…………………………………………	63

LIST OF FIGURES cont.

Figure	Title	Page
A-32.	Baseline SiC/SiNC 38 200 GHz 3……………………………………………	63
A-33.	Baseline SiC/SiNC 38 600 GHz ……………………………………………..	64
A-34.	Baseline SiC/SiNC 39 200 GHz 1……………………………………………	64
A-35.	Baseline SiC/SiNC 39 200 GHz 2……………………………………………	64
A-36.	Baseline SiC/SiNC 39 200 GHz 3……………………………………………	65
A-37.	Baseline SiC/SiNC 39 600 GHz ……………………………………………..	65
A-38.	Baseline SiC/SiNC 40 200 GHz 1……………………………………………	65
A-39.	Baseline SiC/SiNC 40 200 GHz 2……………………………………………	66
A-40.	Baseline SiC/SiNC 40 200 GHz 3……………………………………………	66
A-41.	Baseline SiC/SiNC 40 600 GHz ……………………………………………..	66
B-1.	Image of Multiple Reflection Problem…………………………………….	71

LIST OF TABLES

Table	Title	Page
1.	Results of system optical coupling model…………………………………	22
2.	Kappa values for Oxide/Oxide………..……………………………………	38
3.	Average SiC/SiNC reflectance……………………………………………	42
4.	Stress treatments Oxide/Oxide & SiC/SiNC………………………………	45
5.	Oxide/Oxide 200 GHz reflectance………………………………………...	46
6.	Oxide/Oxide 600 GHz reflectance………………………………………...	46
A-1.	Baseline Oxide/Oxide 200 GHz fits……………………………………….	67
A-2.	Stressed Oxide/Oxide 200 GHz fits……………………………………….	68
A-3.	Baseline Oxide/Oxide 600 GHz fits……………………………………….	68
A-4.	Stressed Oxide/Oxide 600 GHz fits……………………………………….	68
A-5.	Oxide/Oxide fits from CW400 system………………………………….....	69
A-6.	Baseline Oxide/Oxide 200 GHz reflectance………………………………	69
A-7.	Baseline Oxide/Oxide 600 GHz reflectance………………………………	70
A-8.	Condensed CW400 Oxide/Oxide fits………………………………………	70

"This thesis has been cleared for public consumption by the United States Air Force Research Laboratory. The views expressed in this work are those of the author and do not reflect the official policy or position of the United States Air Force, Department of Defense, or the U.S. Government. Case number:

88ABW-2012-5408 (Thesis)

88ABW-2012-5407 (Charts)

Special thanks to Dr. Adam Cooney of the Air Force Research Laboratory Material Directorate for the opportunity to work with these materials.

Special thanks to Dr. Petkie, and the Wright State Physics department for affording me the opportunity to study physics. I hope this work is a testament to their work.

Many thanks for my family in supporting me in this task. I sincerely hope I am able to repay in kind for all that you have given me.

I. INTRODUCTION

1.1. Introduction to CMC Materials

New materials are constantly being developed, but with the introduction of a new material come the responsibility of understanding how a material will react under load. This thesis is part of larger body of work funded by the Air Force on newly developed ceramic matrix composite (CMC) materials. It is desired that these lighter, more heat resistant materials will become the basis for component parts in future aircraft. Stress has been found to cause measurable changes in some CMC materials' dielectric constants in the infrared region, as identified by Dr. Cooney's group [7]. The purpose of this research is to detect if these changes are detectable using millimeter wave techniques as these materials are stressed mechanically and thermally. One goal of this research is to identify possible in-situ non-destructive evaluation (NDE) techniques that could be used to determine the remaining life of these materials. This thesis discusses the systems used to evaluate these materials, the models that were developed to understand the measured spectra, the results of these measurements, and conclusions that can be drawn from this work thus far.

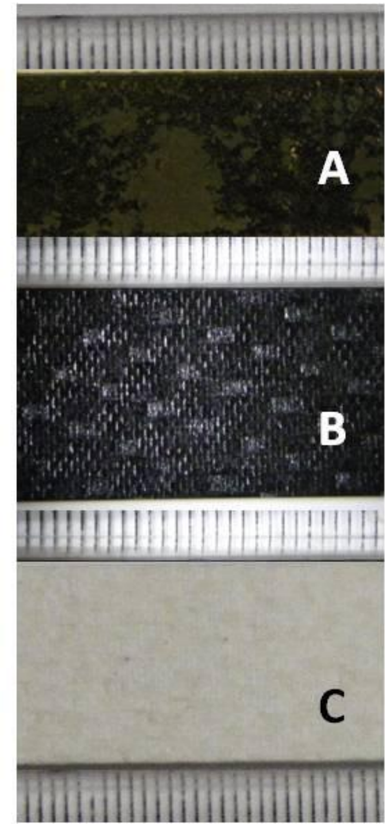

Figure 1: Image of the C/SiC (A) SiC/SiNC (B) and Oxide/Oxide (C) CMC materials. The fiber reinforced nature of the material B and C is evident from the surface pattern, and laminate structure on the sides. Material A does not show these tendencies. The shown scale is in millimeters.

Ceramic matrix composite (CMC) materials were developed nearly four decades ago for use by the military. Initially carbon-carbon composites were developed for use as brakes in military and commercial aircraft. The principle driver for use of these materials has been the Department of

Defense's effort to "lighten the force" [8]. The U.S. Department of Defense Handbook on Composite Materials provides a long but clear definition of these materials.

"A composite is defined as a material containing two or more distinct phases (crystal/material structures) combined in such a way so that each one remains distinct. Based on this broad definition of a composite, CMC's are conveniently separated into two categories: discontinuous reinforced and continuous fiber reinforced composites…Continuous fiber ceramic composites (CFCCs) have required the development of infiltration (vapor, sol, melt, liquid preceramic polymers) methods that enable the densification of various ceramic matrices in continuous fiber lay-ups and /or net shape woven fiber pre-forms. Continuous fiber reinforced CMCs are further subdivided into carbon reinforced carbon composites… and other composites." [8]

The materials studied for this thesis are a form of the fiber reinforced material with the Oxide/Oxide being an eight ply material containing little carbon, and the SiC/SiNC also being an eight ply material containing carbon as noted by this materials more absorptive nature. The use of these material's composite nature, "decrease's the susceptibility of ceramic components to catastrophic thermal-structural brittle failure" by improving the "ceramic's resistance to small flaws and crack propagation", allowing these materials to "fail gracefully" [8]. This study is a proof of concept focused on attempting to track changes in the optical properties of these materials as they were fatigued that may enable the development of non-destructive evaluation (NDE) techniques to identify these material failure points in the millimeter wave region.

1.2. INITIAL RESULTS

Three materials were initially provided to Wright State University for evaluation, a C/SiC CMC of a discontinuous reinforced construction, and two continuous reinforced CMC's labeled Oxide/Oxide and SiC/SiNC. These CMC's were evaluated in a Mach Zehnder transmission interferometer, with the resulting spectra shown in Figure 2. This interferometer was built for evaluating transmission through thin fiberglass composites [23]. Three facts were evident from this evaluation; first the CMC's were not as transmissive as the fiberglass materials, second there

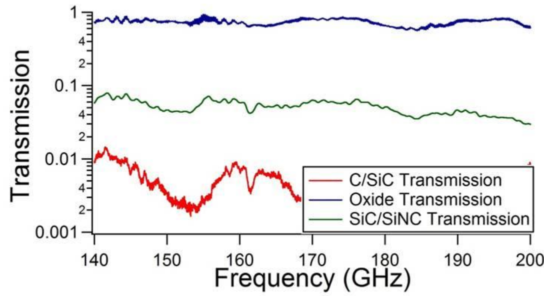

Figure 2: Transmission through the three CMC samples in the Mach-Zehnder interferometer

was an order of magnitude change in the transmission through the different materials, and third tighter focusing optics were required for evaluating these materials. The amount of variation in the material transmittance over this small frequency range was surprising. After completing the reflection measurements it became apparent that the term 'transmission' was loosely used in Figure 2. The 'transmission' measurement through the two carbon based samples was most likely standing waves that developed due to interference of the beam that diffracted around these samples and the rest of the optics system. As a result of the difficulty in making these transmission measurements and the desire to develop NDE techniques for these materials, it was decided to evaluate these materials using reflection based measurements.

This thesis will describe the measurement of reflection and transmission spectra from 12 samples each of the Oxide/Oxide, and the SiC/SiNC CMC materials. Some samples from each group were subjected to a thermal stress treatment, a mechanical strain treatment, or a dwell treatment which consisted of a combination of both treatment types. Reflection/Transmission Spectra from these materials were collected from both the original and stressed materials. This thesis will describe the measurement systems used to record the reflection/transmission spectra from these materials, the models developed to understand these measured spectra and, the determined material optical properties from the recorded spectra. Due to unforeseen manufacturing difficulties, the C/SiC CMC material was not given to Wright State in time for inclusion in this thesis.

II. MEASUREMENT SYSTEMS

2.1. LITERATURE REVIEW OF VARIOUS CHARACTERIZATION SYSTEMS

The initial transmission measures made of these materials caused the focus of this research to move to reflectivity measurements, as agreed upon by the other research groups in this collaboration: Dr. Deibel's Time-Domain Spectroscopy group at Wright State and Dr. Cooney's Infrared Spectroscopy group at Air Force Research Laboratory. An additional reason for this switch, besides the initial transmission measures, was monitoring material reflectivity would lend itself to developing in-situ NDE techniques, a stated purpose of this work. With this stated purpose in mind a system was designed to measure the reflectivity of these samples.

One of the first thoughts in developing this reflection measurement system was to develop a reflection interferometer. Using the source and detection diodes used in the Mach-Zehnder interferometer setup would enable the same computer control mechanism to be used, reducing the complexity of designing such a measurement system. The interference pattern could be used to find the complex index of refraction of the tested material, as discussed in many papers and books on the subject. In one such effort, the researchers discuss tracking the phase of the light from the sample by use of a movable mirror [18]. Another group reported using both the interference fringes of the radiation traveling multiple times through the material, and the interference pattern developed by the interferometer to develop the complex index of refraction [19]. The reports of these works describe using transmission spectra to determine the material optical properties. This is the major reason why similar system designs were not built for this work. There were a number of other groups which discussed using reflection interferometry in their reports [19, 25, 27]. Two of these groups describe using a movable mirror to track the phase of the reflection

spectra [25,27]. From the reflectance and phase measurements, these groups were able to determine the complex index of refraction of the materials. Lastly, a group at the University of Massachusetts-Lowell reported on determining the reflectivity of different metals to very high precision using a continuous wave (CW) laser source [19]. This report, while very thorough, had little impact on our eventual system design but was very informative concerning possible sources of error in the measurement systems used for this work. All of these groups reported on interferometric measurements of some form by making use of the phase of the spectra from the sample. With this phase information these groups were able to determine the complex index of refraction of the measured material. As with most interference based measurements, the majority of the systems discussed by these groups made use of a moving mirror to create and track the beam interference off of the material. While this was desired for the measurements made on the CMC materials, it was not necessary for the measurements requested.

There are many other methods of determining the reflectance from these CMC materials between 100 to 800 GHz other than interferometry. Two such methods are the use of a vector network analyzer and ellipsometry. Vector network analyzers (VNA) enable the experimenter to obtain all of the scattering parameters to the device under test, i.e. the sample. These scattering parameters are related to the impedance matrix of the test [22]. In most cases, the VNA equipment is able to track the phase of the reflected or transmitted waves allowing one to easily determine the complex index of refraction for the material tested. Drawbacks to this method are the expense of the VNA equipment and coupling a wave from the VNA into the CMC materials. The diffraction limited spot diameter for 100 GHz is 3 mm, and the samples had a target size of ~10 mm square. To effectively use a VNA technique with these materials, a tightly focused beam of radiation would be necessary, meaning the use of a standard horn antenna to propagate the radiation would require the use of further focusing optics. Also, the thickness of the sample is important. If the sample is near a multiple of one half a wavelength of the frequency tested

ambiguous results may be found from the resulting spectra [2]. This ambiguity is related to the instability of the Nicolson-Ross equation for low loss materials at multiples of one half integer wavelength [2]. The samples supplied by AFRL at the frequencies of evaluation were a half to three wavelengths thick. Due to these difficulties the use of a VNA system was not pursued for this work.

Ellipsometry is another popular method of determining optical properties from reflection geometry. This method enables one to find the complex index of refraction through a set of documented measurements. Ellipsometric measurements track changes in two complimentary polarizations of the light reflected or transmitted by the sample material [30]. These measurements can be made as a function of wavelength or as a function of the angle of incidence [30]. Thus there are two methods for applying this technique to these samples with the linearly polarized diode sources available for this work. The first is to rotate the source / detector in relation to the sample and record the change in amplitude as a result of these rotations. A second method would be to vary the angle between the sample and the source / detector system, such that there is a changing angle of incidence on the samples. In either case, a special holding apparatus would need to be built or purchased. In both cases, the fixture would need to control the simultaneous motion of the coupling optics, source and detector, or sample rotation and include a means to measure the amount of rotation of the sample to the source/detector. With no such ellipsometry equipment readily available, these types of measurements were not pursued for this work.

Based on constraints of time and money, a simple reflectivity system was built which focused a collimated radiation beam onto and off of these samples. This system was designed such that a phase arm could be added. This phase arm was found not to be necessary due to the wealth of information gathered from the simple reflection measurements. Two different systems were built for this work: a reflection system at 200 GHz, and a reflection / transmission system at 600 GHz.

2.2. MEASUREMENT SYSTEMS USED

As stated at the start of this chapter, multiple research groups were collecting data from these samples. To allow comparison across groups, eleven locations were indentified on the sample. All measurements were to be located in these specific locations, or 'spots' on the sample, which measured 9.5 by 11 mm in size. Figure 3 shows a visual relation of these spots to the beam diameter from the 200 GHz reflection system on the sample. The diffraction limited Gaussian spot diameter is approximately one wavelength when using an F#/1 optic, in the case of 200 GHz this was 1.5 mm diameter. As a result of this large spot size, and the fact that these samples were manually loaded into the reflection system for evaluation, no further attempt was made to differentiate different regions of these eleven spots. Attempts were made to mechanically scan the samples but this proved very difficult as the samples could not be considered optically flat (even for the wavelengths used in this study). Results from the mechanical scans were very confusing as the sample moved in and out of the Rayleigh range of the reflectance system. The Rayleigh range is an optical design approximation of the Gaussian beam profile in which near plane parallel beam fronts is assumed. This region is dependent on the beam spot diameter, and the F# of the focusing optic. This particular system had a Rayleigh range on the order of two spot diameters, a result of the low F# optics used. In the Oxide/Oxide material, as the radiation penetrated through the material, the sample thickness needed to be fully in the system Rayleigh range for the measurement system to have high visibility of the material standing waves. The SiC/SiNC material was more absorbing and the measurement system recorded only the reflectance from the front material surface. By assuring these rules were met for the different samples it was found that the measured spectra from these samples contained many of the system standing waves. Measurements made outside this region, would show similar effects, but the standing waves would show more variability due to the influence the curvature of the Gaussian beam has on the angle of the reflected beam. More variability in the standing waves leads to a

larger variance in the final measurements. Thus the manual placement of the sample was done to reduce the error in the material measurements. The mechanical motion of the sample was replaced by a metal stop which constrained the unsupported length of the sample over a 50 mm region. To determine the spot location of the sample a simple ruler was used to determine which particular sample spot was in the radiation beam. By constraining the relatively short sample length in the radiation beam aided in maintaining the sample placement in the Rayleigh range of the focused Gaussian beam.

The 200 GHz reflection system built was based on a VDI frequency multiplier chain and operated from 132 to 240 GHz. Radiation was collimated using a plano-convex Teflon lens to approximately 45 mm in diameter. The collimated beam was coupled into the reflection system using a mylar beam splitter. The beam splitter is an optical component made of a thin film that reflected approximately 50% of the incident light while transmitting the rest. Placing this thin film at a 45 degree angle in relation to the collimated beam balances the reflected and transmitted beams such that both the reflected and transmitted power is roughly equal. The reflected energy was dumped into the phase arm; the transmitted beam was directed to the sample. Difficulties in setting up the phase arm stemmed from the fact that the power levels in the two arms were not balanced. The majority of the beam was directed into the transmitted beam with the resulting ratio between the transmitted and reflected beams being at 3 to 2. While this discrepancy improved the intensity of the reflection measurements, it made the phase arm very difficult to set up. To successfully use such a system, power would have to be balanced in both arms. Adding the phase arm would have enabled the determination of the phase difference between both arms and aided in the determination of the complex index of refraction for both materials. The transmitted portion of the radiation propagated from the beam splitter to an off-axis parabolic mirror. This 90˚ off-axis parabolic mirror (F#/1) focused the radiation onto the sample. To successfully propagate the sample reflection back to the sensing diode, the angle of the sample

front surface in relation to the focusing mirror was very important. Normal incidence was found after many fine adjustments of the sample. To assure this alignment was maintained for all future measurements, a hard stop was placed at this location and the front surfaces of all samples were placed against this stop. As mentioned above, this stop had a 50 mm space for the sample which constrained the sample over a small portion of its length making the samples surface normal to the incident beam. Using this stop helped to control the amount of error due to variation in the

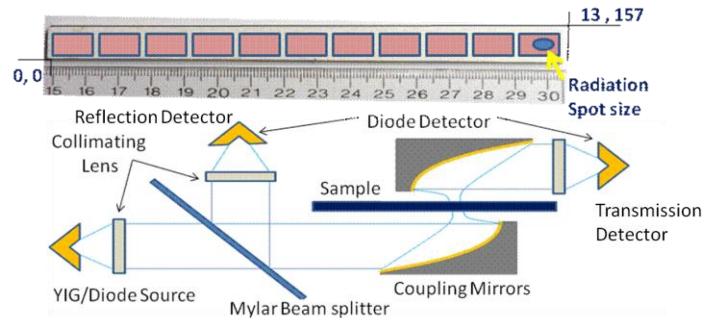

Figure 3: 600-GHz reflectance/transmittance optical system, essentially this system was the original 200 GHz reflection system without the transmission measuring components. Top of figure shows one complete sample with all 11 spots identified. All sample measurements were made of free standing samples.

location and angle of the sample in the Gaussian beam, also known as sample walk-off. By measuring free standing samples the step of de-convolving the sample measurement from reflections of a backing material were avoided, thereby reducing a point of error in the analysis process. The mm wave source was comprised of a YIG oscillator that was swept from 22 to 40 GHz by a control voltage that was swept from 5.5 to 10 volts. This drove a VDI multiplier chain (6x) that emitted radiation in the 132 to 240 GHz frequency range with an output power of ~5 mW. The frequency sweep occurred over a 10 second time period, and the frequency resolution of this system was ~7.5 MHz.

The goal of these measurements was to characterize the front surface reflectance of the CMC materials. To best do this and successfully handle the sample front surface variation, the sample front surface was located at the Gaussian beam waist of the optical system, also known as the

center of the Rayleigh region. As published by the horn manufacturer, 84% of the beam is a fundamental Gaussian mode [31]. Determining the beam spot diameter required measuring the beam width as a function of location by using the knife edge technique. The knife edge technique consists of cutting into the radiation beam with a thin reflector at multiple locations and measuring the reflected power intensity. The derivative of these measurements is taken resulted in the Gaussian beam profile at a particular cut as seen in Figure 4 inset. Taking the *1/e* point of this curve, designated at 33% of the height of this curve, results in the expected Gaussian beam diameter at a particular longitudinal location. Using this method, measurements were made every 0.13 mm in the transverse beam direction, and every 0.50 mm in the longitudinal beam direction. This series of measurements resulted in identifying the Gaussian beam focal point for this system at 140 and 200 GHz as seen in Figure 4.

For the 200 GHz measurements, placing the material at the beam waist virtually assured that the full sample was within the Rayleigh range of the focused Gaussian beam propagated off of the focusing mirror. The estimated Rayleigh range of the 200 GHz system was 3.5 mm. At 600 GHz, this type of beam characterization was not completed and was assumed that the beam focus point did not move, though the length of the Rayleigh range would be roughly a third of that seen in the 200 GHz system. Thus, it is very likely that the full thickness of the Oxide sample was not in the beam's Rayleigh range, meaning that there was a large amount of beam divergence as the beam traveled through the sample, a precursor of low material standing wave visibility. A standing wave in a continuous wave system is the result of the interference between two waves at a slight phase difference. Visibility of the standing wave relates to the coupling of this interference through the optical system, and is exhibited in the depth of these standing waves. These effects were not expected to influence the reflected signal from the SiC/SiNC material. The reflectance was a result of averaging over the system standing waves inherent in all measurements. Due to this averaging the placement of the sample had no influence on the

measured reflectance from this material. Figure 4 shows the Gaussian beam profile for the 200 GHz system, one can see the effects of beam diffraction off of the knife edge especially at the Gaussian beam focus point.

In an attempt to better understand the complex index of refraction for the Oxide/Oxide CMC, a separate system was built at 600 GHz. This system was designed to measure the reflection and transmission spectra over a frequency sweep from 580 to 660 GHz. This system used the same optical setup as the first reflection system, but included a second off-axis parabolic mirror placed

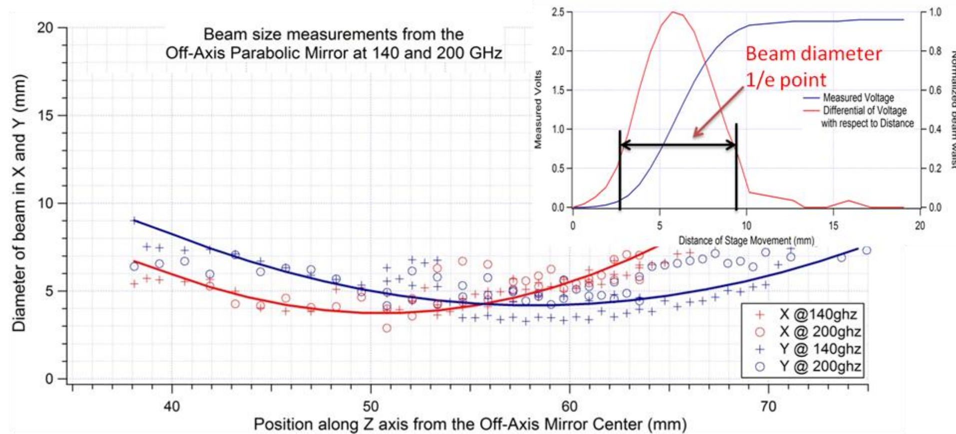

Figure 4: Beam waist measurements from using the knife edge technique. The inset shows one longitudinal measurement, and the accompanying derivative. The points in the larger plot are the *1/e* points of the Gaussian beam. The line of best fit is based on the combination of both frequency measurements (140 & 200 GHz) along each axis (X or Y).

behind the sample to couple the transmitted beam to a second detector diode, as seen in Figure 3. The desire for the transmission spectra was to further develop the optical constants of these CMC materials that were responsible for the reflection spectra. In the case of the SiC/SiNC CMC, the samples were so absorptive that there was literally no transmission spectrum to be recorded using this system. Further measurements of this material with a multimeter resulted in a measured resistance on the order of 200K ohms, thus this material was definitely a conductive dielectric. Understanding the large changes in the measured reflection and transmission spectra for the Oxide/Oxide CMC across many samples was very difficult to understand, especially when compared to the reflection spectra measured in the 200 GHz system. As mentioned in the last

paragraph, this system had a much shorter Rayleigh range, meaning that the sample was not fully located at in this range. This meant that there was a large amount of beam divergence as the beam traveled through the sample, which explains the lack of depth in the material standing wave in these measurements. Also, a feature found in the Oxide/Oxide transmission spectra developed with a separate system further describes why the spectra from this system were so erratic. This system was powered by a VDI multiplier chain (48x) which was supplied by an Agilent synthesizer supplying a FM sweep in frequency centered at 9 GHz. The FM sweep was based on 3 second time window, and had a frequency resolution of 25 MHz. This system had a peak power output of 0.80 mW at 610 GHz.

The 600 GHz measurements provided more insight into the Oxide/Oxide material, but were not enough to fully determine the complex index of refraction due to the limited frequency ranges available from this system. Consequently, a laser driven Teraview CW400 continuous-wave THz system was used at IDCAST in Dayton, OH to generate a sweep in frequency from 200 to 1,000 GHz. This frequency generation was accomplished through the use of photo-mixing technology [29]. This system had two optical heads which were used to generate and detect the continuous wave (CW) radiation through the sample. The specification sheet for this system stated that the beam profile was Gaussian [29]. These two heads were placed 10 cm apart, with the spherical lenses 3 cm above the metal optical table. A profile of the beam propagated by this system was not verified other than to find the maximum beam diameter midway between the heads or 5 cm from the

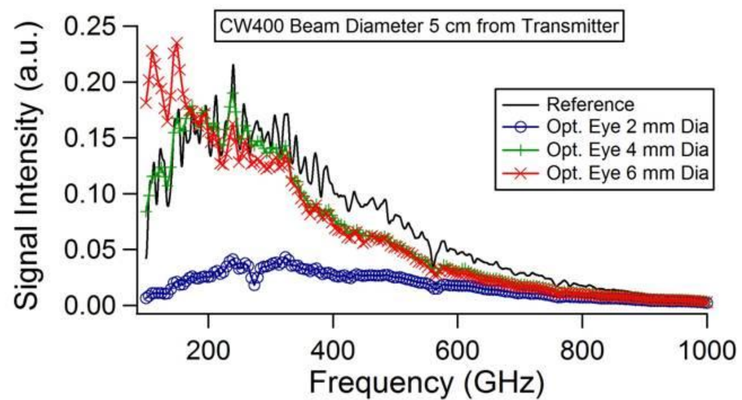

Figure 5: CW400 Beam diameter power measurements. Any power not propagating through the eye either diverged or reflected out of the system.

generation head. This was done using an adjustable iris diaphragm to measure the diameter of the beam midway between the heads. Multiple measurements at different iris diameters show similarity between iris diameters 4 and 6 mm and the reference sweep, seen in Figure 5. The design of this system incorporated a spherical collimating lens as the radiation leaves the source/detector heads. In actuality, it is probable that the beam continued to slightly diverge once the radiation left the head. Also there was the possibility of interference with the beam and the optical table. What was measured by the adjustable iris was the diameter of the radiation midway between the heads that made it into the receiver head. This assumption is evidenced by the very low amplitude of the material standing wave measured with this system through a reference piece of high density polyethylene (HDPE) as well as through the Oxide/Oxide CMC material.

One of the issues with this system was the apparent lack of static discharge protection for these source/detector heads. To avoid damaging this equipment when making these measurements, a tent was placed around the heads and the humidity was elevated using a humidifier. Due to the distance of the beam from the optical table, and not having lenses and mounts to correctly handle this spacing to the table, no external coupling optics were added to this system to improve the propagation of the radiation in free space. To make these measurements the Oxide/Oxide samples were placed midway between the optical heads. This system was setup for measuring transmission, thus the system would need to be reconfigured if reflection measurements were desired. As a result of time constraints, and setup issues no measurement of the SiC/SiNC sample was made. Most of the scans made with this system had a frequency resolution of 150 MHz.

In all of the three measurement systems, the sample measurement was compared to a reference. For transmitted signals, this reference was simply a measure of the power through the optical system without any sample in place. The reflection measures were compared to a metal reference that replaced the sample. Early on, two alternative metal references were purchased from the Wright State University Instrument shop, one aluminum, and the other copper. These reflectors

were machined to the same dimensions as the CMC samples and care was taken to assure that the reflecting surfaces of these references were as smooth as possible based on the capabilities of the shop. This meant Scotchbrite was used to further smooth these surfaces. These references were routinely compared with the standard reference obtained from the Materials Directorate. At the start of the project there was very good agreement between these references. As the project continued and the standard reference was continually used, the reflecting surface became marred, and a slight bend was found at location 10. Thus the eleven spots were not as consistent as at the start of the project. In these cases, the alternative references were more consistent than the standard reference. On any given day, the most consistent reference was used as the reflection reference. Several reasons for deviations of the measured reflectance of the reference material were specular reflections from the reflecting surface, oxide forming on the material surface, or the surface of the reference not being held normal to the optical system as a result of a warp in the metal plate. In most cases these deviations were minor, and will be quantified in the results chapter. On any given day these deviations could be compared thus allowing the error from a reference to be tracked in relation to the other metal references. Lastly, all data from the 200 and 600 GHz systems were measured using a Lock-in amplifier. This technique reduced the amount of noise gathered in the spectra, and was referenced to the internal modulation of the Lock-in device for the 200 GHz measurements, and the internal modulation of the Agilent synthesizer for the 600 GHz measurements. Chapter 4 will discuss how this equipment affected our measurement interpretation.

III. Modeling

It is one thing to make a measurement; it is another to understand the underlying fundamental properties which cause the behavior. To understand the phenomena behind the CMC transmission and reflection spectra in the context of the different optical systems, a series of mathematical models were developed based on physical theory. Adjusting the optical constants used in these models made it possible to emulate the material measurements. The understanding gained with these models allowed limits to be placed on the material properties used to fit the measured data ensuring physically tenable results. Two models based on the Fresnel equations were developed for the materials. To accurately model the Oxide/Oxide CMC spectra, in particular the depth of the standing wave (etalon) pattern (also known as the fringe or standing wave visibility), a separate system dependent Gaussian beam propagation model was developed. Both the system model and the material model were used to form a general model which was used to fit the measured Oxide/Oxide spectra allowing the determination of the complex index of refraction. A material model was derived for the SiC/SiNC material but the measured spectra was etalon free and thus this model had little meaning other than to reaffirm the derivation of the reflectance from the measured spectra.

3.1. MATERIAL MODELING

The SiC/SiNC material can be modeled as an absorbing dielectric. This statement stems from the fact that the material had a measurable conductivity between 100 - 200 K-ohms and did not transmit radiation at the measured frequencies. It reflected roughly 30% of the radiation directed at it. Using the standard Fresnel equations identified in any optics book, one finds the following equations for the reflection coefficient:

$$r_{para.} = \frac{n_{com}-1}{n_{com}+1} A_{para.} \qquad \textbf{Eqn. 1}$$

$$r_{perp.} = -\frac{n_{com}-1}{n_{com}+1} A_{perp.} \qquad \textbf{Eqn. 2}$$

In these equations, A is the complex magnitude of the incident electric field containing both the magnitude and the phase of the field, n_{com} is the complex index of refraction of the material divided by the index of refraction of air (the surrounding material) [4]. The mm-wave sources used in this study were linearly polarized meaning the radiation was oriented "vertically" in relation to the sample, but at normal incidence Equations 1 and 2 become equivalent. Thus these measurements could be described as S, or P polarized. The parallel (r_{para}) and perpendicular (r_{perp}) reflection components become the material reflectivity by [4]:

$$R = \left|\frac{r_{para}}{A_{para}}\right|^2 = \left|\frac{r_{perp}}{A_{perp}}\right|^2 = \left|\frac{n_{com}-1}{n_{com}+1}\right|^2 = \frac{P_{mat}}{P_{ref}} \qquad \textbf{Eqn. 3}$$

In this thesis, the reflectivity (R) that is recorded for the SiC/SiNC material is the reflected power (P_{mat}) off the front material surface divided by the reflected power from the reference metal (P_{ref}).

The reflection and transmission spectra from the Oxide/Oxide material were not as easily understood. From the first transmission measurements, a material standing wave was detected. At any surface there is a reflected and a transmitted beam. A standing wave will be detected when the absorption coefficient of the material is not large

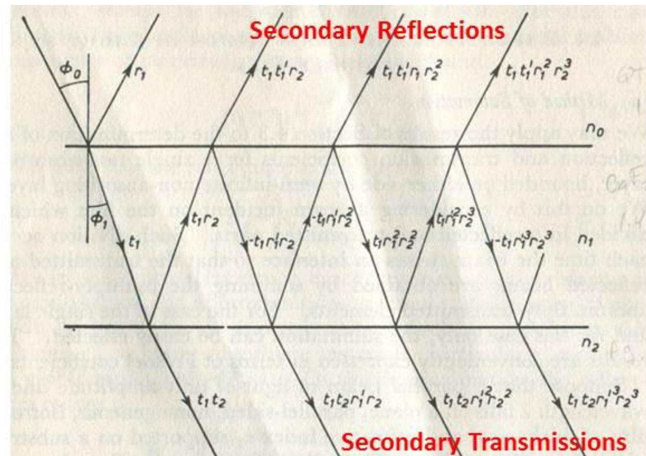

Figure 6: Figure 4.3 in O.S. Heavens book showing the multiple reflected and transmitted waves, r_1 and t_1 are the initial reflected and transmitted waves. The samples in this study were surrounded by air ($n_0 = n_2$).

enough to absorb this secondary reflected radiation traveling back through the material. These secondary waves are propagated back through the sample from the rear material surface. When these waves reach the front surface a second time, a portion is transmitted out of the sample, and the rest is reflected back into the sample. These reflected internal waves eventually are released out of the sample, or absorbed. This reflected radiation is released, at a phase difference from the initial transmitted or reflected beam leading to an interference pattern, or standing wave based on the material thickness. Figure 6 shows this process very succinctly [15]. The interference patterns have fringes based on the material thickness and the real part of the material index by the following relation:

$$v_{fs} = c/2nt \qquad \textbf{Eqn.4}$$

In this equation c is the speed of light, n is the real part of the material complex index of refraction, t is the thickness of the material, and v_{fs} is the frequency of fringe separation. Two methods of modeling such a material are a model based on a lossy Fabry-Perot cavity or a derivation from the Fresnel equations.

Fabry-Perot cavities are used quite often in laser systems as regenerative cavities and components for the mode locking in pulsed laser systems. They are also used for spectroscopy to allow for multiple passes through a gas or liquid sample. In this model, the material side walls are viewed as the cavity mirrors, and the material between the walls is the lossy dielectric cavity [26].

$$t_{fp} = \frac{-t_1\, t_2 e^{-\alpha d - i\omega d/c}}{1 - r_1 r_2 e^{-2\alpha d - 2i\omega d/c}} \qquad r_{fp} = \frac{r_1 - r_2 e^{-\alpha d - i\omega d/c}}{1 - r_1 r_2 e^{-2\alpha d - 2i\omega d/c}} \qquad \textbf{Eqn. 5}$$

In these equations, t_1, t_2, r_1, and r_2 represent the reflected and transmitted portion of the beam at the material surfaces. In these equations, α is the absorption coefficient of the material, d is the material thickness, and ω is the frequency. The absorbance coefficient was found from the CW400 system measurements or derived from the extinction coefficient found via the reflection /

transmission measurements from 580-660 GHz. The first and second reflections and transmissions are based on the Fresnel equations at the material / air interfaces. These quantities were measured in all of the spectra gathered from the Oxide/Oxide material but are combined. Thus the measured reflected spectra contain of t_1, r_1, and r_2 and the transmitted spectra consisted of t_1, t_2, and r_2. Also, as both the reflected and transmitted spectra were on the same order, and had significant depth it was difficult to make an assumption that any term was insignificant. Instead of attempting to de-convolve these quantities, a separate model was developed based on the Fresnel equations.

To derive the Fresnel equation model, one must start with the equations at the front and rear surfaces of the material and require that there is continuity at these interfaces between the material and the surrounding material (air for a free standing sample). There are many papers which reference these equations [19, 20, 24, 25]. The difficulty with these articles, as it related to our measurements, is they deal with transmission measurements; the majority of measurements for this work were reflections. Also, a number of these articles used identical equations with differences in the method of simplification causing the presented equations to have a different appearance. Noted sources which derived these equations were Heaven's text, Ward's text, Abele's article and Girard and Delisle's article [1, 6, 11, 15, 33]. Girard and Delisle's description is noteworthy in that the equations derived are for a material with a thickness of the same order as the radiation wavelength thus the phase difference between the first and secondary reflection/transmission waves are included in the model. Using these sources as references, the following models were developed which base the material reflectance and transmittance on the complex index of refraction and the material thickness:

$$T(v) = \frac{16(k^2+n^2)/((n+1)^2+k^2)^2}{\exp(\delta k)+\rho^4 \exp(-\delta k)+2\rho^2\cos(2\phi-\delta n)} \quad \textbf{Eqn. 6}$$

$$R(v) = \frac{2\rho^2(\cosh(\delta k)+cos(\delta n))}{\exp(\delta k)+\rho^4\exp(-\delta k)+2\rho^2\cos(2\phi-\delta n)} \quad \textbf{Eqn. 7}$$

$$\delta = \frac{4\pi d v}{c} \quad \textbf{Eqn. 8}$$

$$\rho^2 = \frac{(n-1)^2+\kappa^2}{(n+1)^2+\kappa^2} \quad \textbf{Eqn. 9}$$

$$\phi = tan^{-1}(-2\kappa/(n^2+\kappa^2-1)) \quad \textbf{Eqn. 10}$$

Where: *c* is the speed of light
d is material thickness
n is the real part of the material complex index of refraction
κ is the imaginary part of the material complex index of refraction
ν is the frequency of the measurement

These formulas were independent enough that either reflected or transmitted spectra would have sufficed to properly use these formulas, but this research worked out in such a way that both types of spectra was gathered. Thus, a form of each of these models was used to fit the material standing wave, allowing the complex index of refraction for the Oxide/Oxide CMC to be based on all the measured spectra. Figure 7 shows this model as a function of frequency.

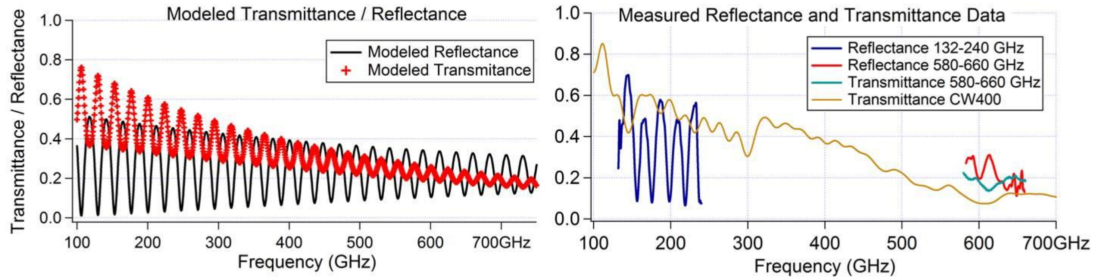

Figure 7: Modeled (left) and Measured Spectra (right) for the Oxide/Oxide sample.

All of the material models that were discussed did not consider scattering. It is known from scattering theory that surface roughness on the order of a tenth of a wavelength will generate a significant amount of scatter [35]. At a surface roughness below this threshold scattering becomes insignificant. During this project, measurements were made of the material surface

roughness using a surface profilometer. These values ranged from about 1.6 μm for the Oxide/Oxide material to 2.2 μm for the SiC/SiNC material. Several measures made of the C/SiC material produced a material roughness of 4.9 μm. The wavelengths used for sample evaluation ranged from 2.3 to 0.5 mm. This left two orders of magnitude between the surface roughness of the material and the measurement wavelength well within the Rayleigh scattering regime. The profilometer measurements were made by averaging the movement of the needle of this device over several periods of the surface weave. These measurements were made both along the length of the sample, and across the width of the sample, with insignificant differences between these directional measures. Figure 8 shows what the surfaces of the SiC/SiNC sample looked like after various treatments, the inset spots are estimated beam diameters of the 200 and 600 GHz systems.

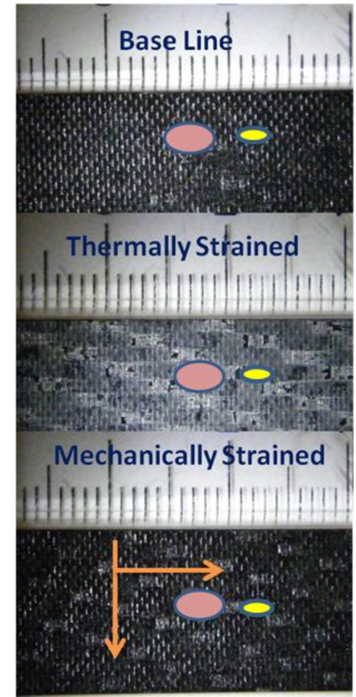

Figure 8: View of the SiC/SiNC material surfaces. Arrows represent the directions of the surface profilometer measurements. The stressed sample weaves stands out more than the baseline sample weaves. Red spots are the approximate 200 GHz radiation spot size, yellow spots are the 600 GHz approx. spot size.

3.2. SYSTEM MODELING

As seen in Figure 7, there were major discrepancies in the depth of the modeled Oxide standing waves, or visibility, versus the measured standing waves for this material. The Gaussian power coupling coefficient was used to correctly understand the visibility of the standing waves in the Oxide/Oxide measurements. This coefficient will be described in the following paragraphs as it relates to a simple transmission measurement system for a sample of high density polyethylene (HDPE). By adjusting the material model to include a visibility coefficient, a single model was built that could be used on the three different Oxide/Oxide spectra that were measured.

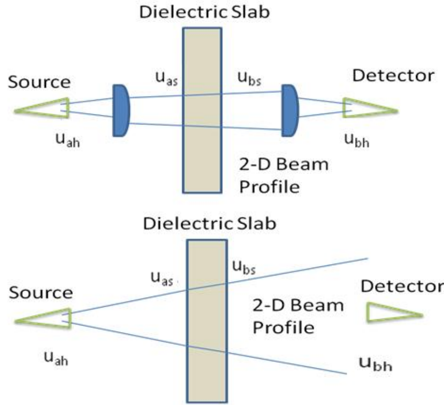

Figure 9: Transmission system

To better understand system effects on the standing wave visibility, a simple transmission system was built. In this system, two cases were tested and modeled. The first case included a set of collimating lenses between the horns with the sample being placed between these lenses. This system attempted to conserve all of the power and consequently maximized the signal to noise ratio. As a result, measurements from this system were sensitive to all possible standing waves in the system. In this system, two primary standing waves were expected; one associated with the horn to horn measurement, and the other associated with the HDPE material. The second case did not include the collimating lenses, but instead allowed the Gaussian beam to diverge through the sample. Without these lenses, it was expected that both standing waves would be reduced due to a diverging beam propagating through the system. This second system was similar to the setup used for the measurements made of the Oxide/Oxide CMC using the CW400 Teraview system. Figure 9 depicts this simple transmission system.

To model these effects, optical system ABCD matrices were assembled for all of the components between the horns of the transmission system. Various sources discuss the ABCD matrix construction notably a paper by Halbach entitled 'The matrix representation of Gaussian optics'[14, 16]. In this paper, similar to other sources, a Gaussian vector was 'propagated' through the standard optical matrix system. This Gaussian propagation vector q consists of two components: a real component for the radius of curvature of the spherical beam front defined as R, and an imaginary component of the radius of the beam defined as r.

$$\frac{1}{q} = \frac{1}{R} - \frac{i\lambda}{\pi r^2} \quad \textbf{Eqn. 11}$$

$$q = \begin{bmatrix} 1/Re(q) \\ 1/Im(q) \end{bmatrix} = \begin{bmatrix} Im(q)/Re(q) \\ 1 \end{bmatrix} \quad \textbf{Eqn. 12}$$

Multiplying the matrix of the system by this vector, one can find the Gaussian beam parameters throughout the system. With this information, the coupling of the Gaussian beam between system elements could be determined via use of the power coupling coefficient (Eqn 13). This coefficient is actually the square of the overlap integral or coupling coefficient (Eqn 14), and describes how similar the Gaussian beam components are at two distinct locations in the optical system. An example of using Equation 13 would be to determine the power coupling from either side of the HDPE slab, or at the source and detector horns. To determine the power coupling coefficient one must determine the Gaussian beam components at both locations in the optical system using the ABCD matrices and the Gaussian propagation vector. These Gaussian beam fronts are referenced as u_a, and u_b in Figure 9. These components are then placed into Equation 13. Very similar beam components have a unity coupling coefficient (C_{ab}~1); whereas a low coupling coefficient is evidence of divergence of the Gaussian beam through that portion of the optical system [12, 13, 21]. In Eqn. 14 the u represents the Gaussian beam as a function of radius.

$$K_{ab} = |C_{ab}|^2 = \frac{4}{(\pi r_a r_b/\lambda)^2(1/R_a - 1/R_b)^2 + (r_a/r_b + r_b/r_a)^2} \quad \textbf{Eqn. 13}$$

$$C_{ab} = \int_0^\infty u_a * u_b \, 2\pi r dr \quad \textbf{Eqn. 14}$$

This coupling is related to the amplitude of the standing wave, thus a poorly coupled standing wave has lower amplitude than a strongly coupled standing wave as evidenced in Figure 10. Using Equation 13 the coupling coefficients between the source/detection horns and both sides of the slab were calculated. In Table 1, 'Average Output Volts' is the detector output from the Lock-in Amplifier averaged over one full frequency sweep from 72 to 120 GHz.

	K_{ab} Coupling Horn/Horn	K_{ab} Coupling Slab front /Slab rear	Average Output Volts
Coll. Lenses	0.868	0.996	2.84
No Optics	0.044	0.990	0.14

Table 1: Result of the system coupling model (72-120 GHz).

From Table 1, the ratio of the horn to horn coupling with and without the collimating lenses was a factor of 19.8. Comparing this calculated number to the measured average detector voltage, we find a measured factor of 20.2 times, thus the horn to horn coupling is a true measure of the power that the detector is measuring. Looking at the unsmoothed transmission data measured with this system (Fig. 10), many interesting things are noticeable. First, the horn to horn standing waves really drown out the material etalon in the collimated lens system. This is due to the similarity between the two coupling coefficients for this system setup, 0.86 (horn to horn) and 0.99 (dielectric slab). Looking at the un-collimated system measurement with no focusing optics, one can readily see the material etalon in the raw transmittance data in the regions associated with high diode power output only, 95 to 110 GHz. These regions seen in both raw transmission data plots correspond to the peak power output of the diode system. Thus much of the 'noise' associated with the horn to horn standing waves below 95 GHz, as opposed to the material standing wave, which was not readily sensed by the detector. The frequency period of the horn to horn standing wave was ~375 MHz which corresponds to a horn to horn distance of 40 cm, and ~13 GHz for the Black HDPE which corresponds to a material thickness of 19 mm.

In order for either of these standing wave patterns to be fit using the material models discussed in the last section, a data smoothing technique is necessary. By using a simple box smoothing technique, the horn to horn standing waves are readily washed away leaving the smoothed transmission wave with the material etalon, as seen in Figure 10.

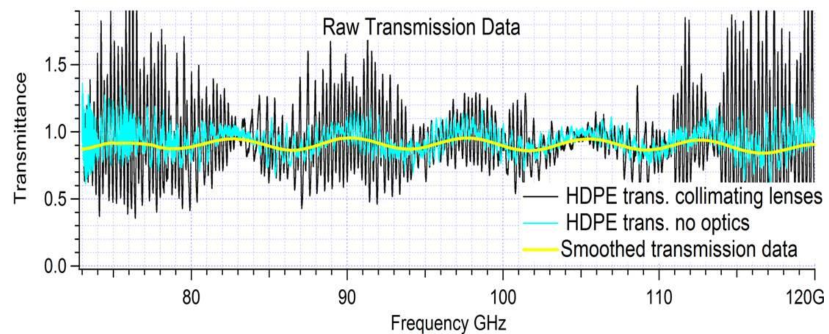

Figure 10: Transmission data from the HDPE transmission measurements. The center thick line is the smoothed collimated lens data.

3.3. COMBINED MODELS

With this understanding of system visibility turning to the Oxide/Oxide material measurements, all of these effects become clearer. In both the 200 and 600 GHz measurement systems, the sample was placed to maximize the reflected signal from the front material surface by placing the CMC front surface at the Gaussian beam focal point. The Oxide/Oxide materials varied in thickness up to 0.15 mm. This variation can be translated to nearly 30% of the sampling wavelength at the 600 GHz system. Just the thickness variation of the sample alone would lead to a variance in the sample placement in the 600 GHz system's Rayleigh range of more than 20%. Using Equation 13 at 600 GHz the estimated power coupling coefficient through the Oxide sample is $0.32 \pm .04$ with the deviation due to the material thickness variation. This led to a ~30% phase shift, and a loss in the amplitude of the material standing wave between the spot to spot measurements as shown in the next chapter. The CW400 system measurements which made use of no focusing optics thus a significant portion of the signal was lost due to the diverging beam. The method of dealing with these varying system characteristics was to multiply the material reflectance and transmittance equations (Eqns. 6 and 7) by a coupling coefficient, similar to those calculated in the last section. Thus the adjusted model used to fit these varying measurements is found in equation 15.

$$R_{mea}(v) = V/2 + V * R(v) \qquad T_{mea}(v) = V/2 + V * T(v) \qquad \textbf{eqn. 15}$$

A decrease in standing wave visibility does not decrease the material reflectance/transmittance but does decrease the amplitude of the material standing wave. The added term, $V/2$ maintains this relationship by returning the reflectance/transmittance to its true value. When using this model to fit the measured Oxide/Oxide data, empirical estimates were made for V, or the visibility of the system. In the case of the 600 GHz system with simultaneous reflectance and transmittance measures, the same visibility factor was used for both the transmission and reflection measurements. Thus, these values ranged from 0.6 to 0.3. For the CW400, the system

visibility ranged from 0.2 to 0.5. Finally, for the 200 GHz measurements a visibility of 1 was used. In this case the added constant was not used.

By modeling the Fresnel equations at the material interfaces, understanding of the reflection and transmission spectra was gained. The model for the Oxide/Oxide material developed the relationship between the measured reflection as a function of frequency, sample thickness, and the complex index of refraction. By modeling the Gaussian beam coupling throughout an optical system, one can determine the amplitude of the standing waves. The three different optical systems used to measure the Oxide/Oxide material each exhibited different standing wave amplitudes. This amplitude change was due to varying coupling coefficients of the Gaussian beam components on either side of the material. By choosing a visibility factor and adding this factor to the Fresnel model for the Oxide/Oxide material, one model could be used to fit all three data sets. For the SiC/SiNC CMC, the measurement system did not detect the interference due to the multiple reflections in this material, thus this material was able to be modeled using the Fresnel equation from the front surface only. The next chapter discusses the error in these measurement systems.

IV. Measurement Technique

With the background of the optical system used and the models used to interpret our results, this chapter will discuss the methodology used to interpret the errors in our system and how the quantities of interest were determined from these measurements. Following is a brief description of how each system was used to determine the CMC optical properties.

The 200 GHz system, shown in Figure 3, was used to make our first reflectance measures for these materials. This system was used to collect the bulk of the data presented in this thesis. Having a large amount of power compared to the other systems, this system was the easiest to use and the data was relatively noiseless. Many of the base line samples were measured three times in this system, with minor adjustments being made with each measure to improve the fidelity of the results.

Desiring more information about the CMC optical properties the 600 GHz reflection/transmission system was constructed. There were two motivations for building this system. It was hoped that the complex index of refraction for the material could be extracted from the reflection and transmission spectra. Our second motivation was Dr. Deibel's group saw interesting signatures in the reflection spectra from the samples at 600 GHz. It was hoped to find similar signatures in the CW spectra. At this point in the study, the true absorptive nature of SiC/SiNC had not been fully realized, thus at the time, there was the hope that transmission spectra could be measured from this material as well. After setting up this system and making measurements, a few things became apparent. First, the diodes which powered this system had roughly a third of the power of the 200 GHz system. As a result, this data had drastically more noise than that found with the 200 GHz measures as the optics of the system did not change. Prior transmission measurements

of the SiC/SiNC material showed that this material had an absorptive nature, but it was hoped that with focusing optics that a small amount of transmission could be detected. With the reduced power of the 600 GHz diode chain, it quickly became apparent that there was no hope of seeing transmission through this material even with focused optics. Second, the 600 GHz diode chain exhibited a 50% decrease in power during the frequency sweep [32]. For the SiC/SiNC reflection measurements, this meant very little. For the Oxide/Oxide, it made things very difficult. It was anticipating a continuous standing wave pattern for the full 80 GHz sweep in frequency sweep of this diode chain could be measured. Prior measurements had a material standing wave period of roughly 20 GHz. Due to the low power from this diode and the power drop, a continuous standing wave pattern over 32 GHz, or roughly 1.6 periods of the standing wave pattern was possible. Once the CW400 measurements were completed for the Oxide/Oxide material, it became apparent from features in these spectra that the associated drop in the 600 GHz reflectance/transmittance values was actually associated to an absorption/scattering feature at 600 GHz and not the drop in diode power. As a result of these difficulties, this system was not as easy to operate as the 200 GHz system, and only resulted in one set of complete data for all the samples.

The last attempt to gather spectra for the Oxide/Oxide sample occurred using the Teraview CW400 system at IDCAST. As mentioned in Chapter 2, this continuous wave (CW) source was able to generate CW frequencies from 100 GHz to 1.5 THz. For the Oxide/Oxide samples, the usable portion of this span was 200 to 800 GHz. This system, while cumbersome to use, provided enough data to develop κ for this CMC, the imaginary part of the complex index. Also the data from the Oxide/Oxide CMC included many features which only became apparent after studying all the spectra. Due to the absorptive nature of the SiC/SiNC CMC and the length of time necessary for these measurements, no attempt was made to measure the SiC/SiNC material on this system.

4.1. ERROR PROPAGATION

In order to increase the signal to noise ratio of the system, a Lock-In amplifier was used. The Lock-In was referenced to its own internal AM modulation for the 200 GHz measurements and AM modulation from the Agilent synthesizer for the 600 GHz measurements. This device greatly reduced the *1/f* noise in these measurements to such a level that much of the initial data, gathered with the 200 GHz diode chain, did not even have to be smoothed to get rid of this noise. For most measurements, the time constant (τ) was left at 1 mS enabling the use of a 1 kHz sampling rate. The AM modulation frequency was 10 kHz. The time constant is the length of time the measurements were integrated over by the amplifier. This integration constant, as well as the length of time for measurement ($T_{meas.}$), determined the number of independent points in the collected data. Equation 16 describes this relationship. In the 200 GHz system T_{meas} was 10 seconds. For the 600 GHz measures, this quantity was 3 seconds.

$$Ind. Points = T_{meas.}/\tau \qquad \textbf{Eqn. 16}$$

Using Equation 16, the number of independent points for the 200 GHz measures was 1000, and 300 for the 600 GHz measures. By using a box smoothing technique, the data was effectively smoothed, further reducing the true amount of independent points, but effectively getting rid of unwanted standing wave system noise. The Oxide data was fitted with a program in IGOR Pro which enabled the use of the model described in the last chapter. These model fits were based on the complex index of refraction and the material thickness. As a result of this fitting function, one set of parameters was determined for each spectrum of data, the complex index of refraction. Thus this data was not reduced in any way to reflect systematic deviations of the independent points in the data. The SiC/SiNC measures were initially smoothed to a lesser degree due to the lack of noise in the data using the box smoothing technique. Eventually, the SiC/SiNC reflectance was further down sampled to a point every 2 GHz. This was done to reflect the

number of independent points in the data due to the relatively featureless reflectance spectrum, but also to deal with the remaining standing waves that were inherent in all of the data. As a result of this re-sampling the SiC/SiNC 200 GHz data, 51 points are presented. For the 600 GHz data, 36 points are presented. This down sampling in both cases maintained the trends of the data but reduced the standing wave effects that dominated the oversampled data.

Each measurement set included a set of metal reflector measures. There were many reasons for doing this. First, the diodes used are known to have minor power variations from day to day. Comparing the sample spectra to a metal reference gathered the same day removed the need to determine the degree of power variation for the measurements. A second reason for using such a reference is that it gave a quick check as to the alignment of the system. A change in the incidence angle would greatly reduce the reflectance from the metal reference, a quick check of the alignment of the system. The variation in the measured reflectance was coupled to the flatness of the sample. By having multiple metal references that were evaluated throughout the project, it was assured that if one reference was damaged due to reference flatness or surface defect another reference which had been continuously characterized could take its place. When determining the calculated reflectance, the sample measurement of a spot was compared to the same spot on the metal reference. This helped to further reduce the angular error as sample and the metal reference were held in the same jig, and being the same size they both would have a similar angular relationship to the reflection system. Due to this fact, no attempt was made to quantify the measurable affect angular changes had on the measured reflectance. Figure 11 shows all of the metal references

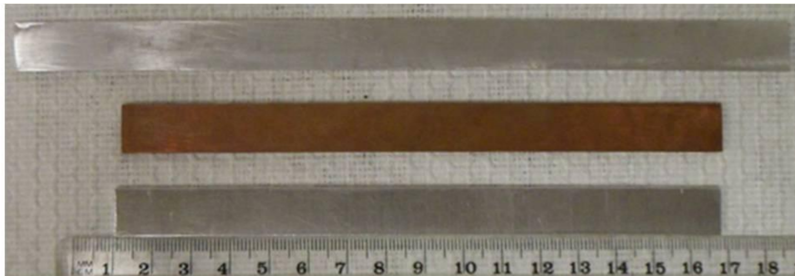

Figure 11: Metal references evaluated for this project. Bottom is the original supplied aluminum reference, middle is copper, and top is the aluminum reference.

that were characterized during this project. As the project progressed, it was noticed that spot 10 from the original reference was returning less radiation than at the project start. Evaluation on a flat surface revealed a slight bend at this location. Figure 12, below, shows the reflectance measured from all references shown in Figure 11. These plots were made with the 200 GHz system at the relative start of the project. A measure of the variance of the provided aluminum reference was 3.8% while the two purchased references had variances of 1.7% for copper, and 0.3% for the new aluminum reference. These drastic differences were due to the surface treatments of the copper and aluminum reference dealing with surface roughness, also when these references were made they showed less than 0.2 mm variation in flatness over their entire length. The 600 GHz measurements, seen in Figure 12, were made with the final data set used in this thesis. These reference power curves show the expected power curves from VDI diode chains used in these systems. In these plots, both y-axis's have similar arbitrary units based on a 1 mV lock-in sensitivity. The large amount of deviation in the 600 GHz reflection measures was due to angular variation in sample placement. As mentioned earlier, the 600 GHz diodes transmitted roughly a third of the power that the 200 GHz diodes propagated.

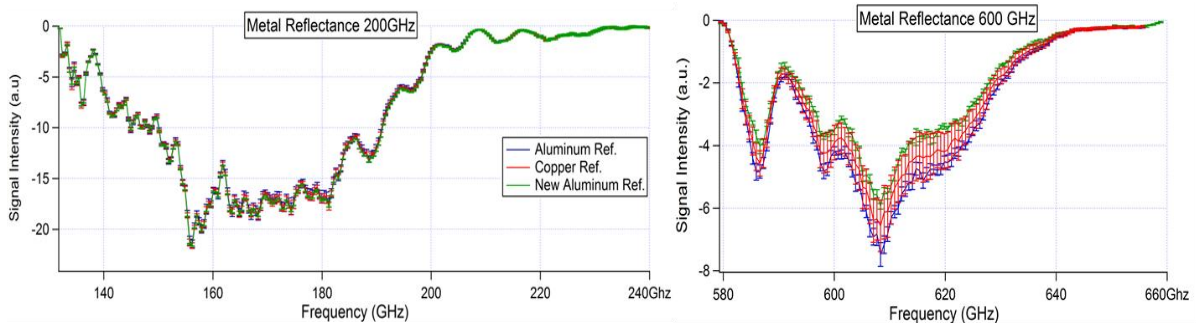

Figure 12: Measured reflectance from the metal references used in this project with one standard deviation error bars. As mentioned earlier the power from the 600 GHz diode chain was one third of the 200 GHz chain according to the VDI data sheets.

The project statement was to find the front surface reflectance of these materials. In Chapter 3, Equation 3 showed that front surface reflectance at normal incidence as:

$$R = P_s/P_M \qquad \textbf{Eqn. 3}$$

with R as the reflectance, P_s as the power reflected by the sample and P_m as the power reflected by the metal reflector. The standard deviation of R found using error propagation techniques is described via Equation 17[34]:

$$\sigma_R = R\sqrt{\left(\frac{\sigma_S}{P_S}\right)^2 + \left(\frac{\sigma_M}{P_M}\right)^2} \qquad \textbf{Eqn. 17}$$

In this equation, σ is the standard deviation of the sample or reference measurement depending on the subscript. To determine this, standard deviation equation 18 was used:

$$\sigma_x = \sqrt{\left(\sum_i^n (x_i - \bar{x})^2/(n-1)\right)} \qquad \textbf{Eqn. 18}$$

Equation 18 is required for finding the sample standard deviation based on the fact that $\bar{x}$, the sample average, was found by averaging the sample set. This decreases the overall degrees of freedom of this measure [34, 3]. When evaluating the measures, it is assumed that the index of refraction was equivalent across a single sample. As a result of this assumption, $\bar{x}$ is the average value determined from the 11 spot measurements made on one day from one sample. The standard deviation, calculated from Equation 18, is calculated from this $\bar{x}$ for the same sample. The standard deviations calculated for a sample provided a measure of the system error inherent in this measurement system. A comparison of the different sample means over multiple samples provided an understanding of the variance of the variations in the samples' optical properties. Equation 19 was used to define error in these situations. This $\sigma_{\bar{x}}$ is also called standard error.

$$\sigma_{\bar{x}} = \sigma_x/\sqrt{m} \qquad \textbf{Eqn. 19}$$

In Equation 18 n represents the number of measures made on one sample, and m in Equation 19 represents the number of samples being combined. For the stressed sample cases, this comparison of multiple sample means was not possible due to having one stressed sample. In these cases, the system error (Eqn. 18) was used as the treatment standard deviation. It is now possible to discuss

the analysis of the Oxide/Oxide and SiC/SiNC CMC materials with this understanding of the error propagation.

4.2. SiC/SiNC MEASUREMENTS

As used in all measures, the reflectance was defined as the power reflected from the sample divided by power reflected from the metal reference, or P_s/P_m. Figure 13 shows the raw reflected reference signal that was recorded from the 200 and 600 GHz systems. Following this is Figure 14 which shows the calculated reflectance using this formula. To remove the noise inherent in this calculation, the data was smoothed and then down sampled to reflect independent measurement points. The noise at the start and end of the Figure 14 is due to the low power from the diode chain. The variations seen at the ends of the sweep are not real and the effect of dividing a small number by an even smaller number, in essence noise over noise. The ends of the data were chopped off when they could not be smoothed.

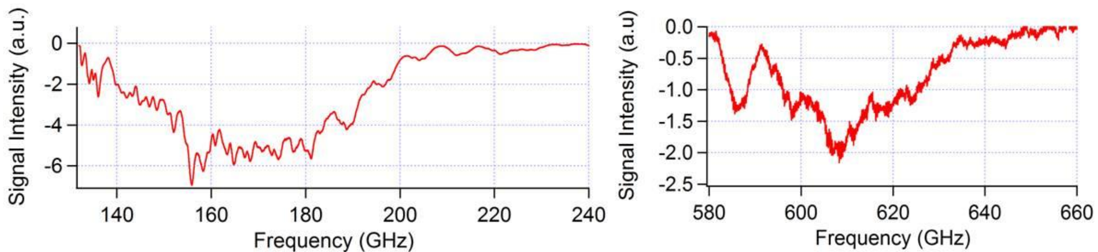

Figure 13: Raw reflectance measures from a SiNC sample at 200 GHz (left), and 600 GHz (right).

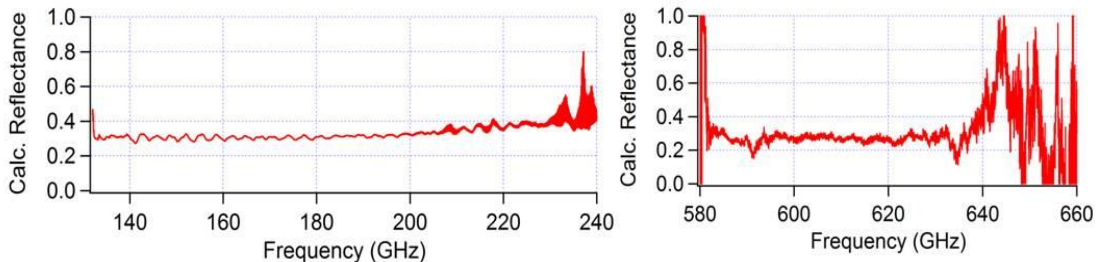

Figure 14: Calculated reflectance from a SiC/SiNC sample at 200 GHz (left) and 600 GHz (right).

As mentioned in the Error Propagation section, these waves were smoothed to mitigate the remaining standing wave effects seen in Figure 14. Once these waves were smoothed they were

down sampled to 51 points for the 200 GHz measures and 36 points for the 600 GHz measures. Figure 15 shows these smoothed / down sampled waves with the averaged data plotted. The standard deviation was calculated using Equation 18. When combining multiple sample measures together Equation 19 was used, as in the case of the baseline measurements. As seen in Figure 15, the increased signal to noise ratio of the 200 GHz system is apparent. Spot 11 in the 200 GHz system was considered an outlier, but this same spot in the 600 GHz system had to be considered part of the sample set due to larger sample variation.

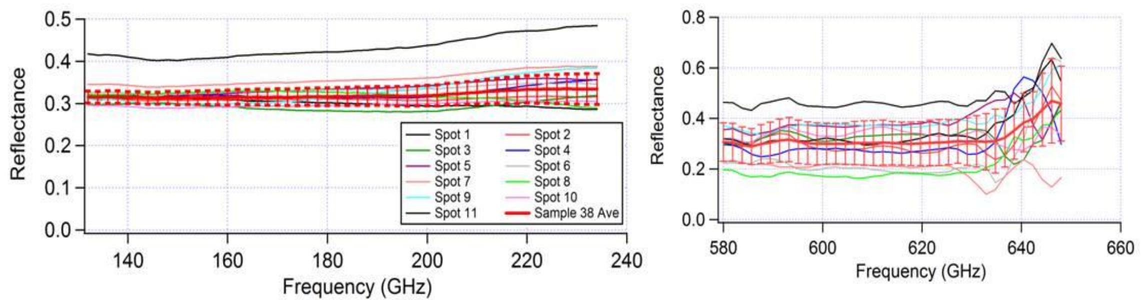

Figure 15: Finalized reflectance plots for SiC/SiNC sample 38; 200 GHz measures (left), 600 GHz measures (right). Notice the scale change between the two plots, the 200 GHz measures had less variation than the 600 GHz measures.

For the SiC/SiNC CMC, the front surface reflectance was found. The fact that this material has the more absorptive carbon causes these materials to be fairly absorbing meaning there was no chance of seeing a material standing wave with this material.

4.3. OXIDE/OXIDE MEASUREMENTS

In the initial transmission measurement of the Oxide/Oxide sample a very strong material standing wave was observed. This material etalon was so strong that an FFT of the measured signal from this material showed the presence of this wave over the system noise of the measurement for the 200 GHz system. This section will present the measurements from the three different systems and discuss how they were used to derive the complex index of refraction for the Oxide/Oxide CMC material using this inherent standing wave. Initial measurements were made of this material using the 200 GHz reflection and 600 GHz reflection and transmission

system. Figure 16 shows the measured spectra for the Oxide/Oxide material using the 200 and 600 GHz system. Figure 17 depicts the calculated reflectance / transmittance found by dividing the spectra from the material by reference spectra as referenced in Equation 3. Fitting the material standing wave seen in these figures with Equation 15 enabled the determination of the complex index of refraction for this material. Figure 18 shows some of the final fits of this Oxide/Oxide material using the adjusted material model, Equation 15.

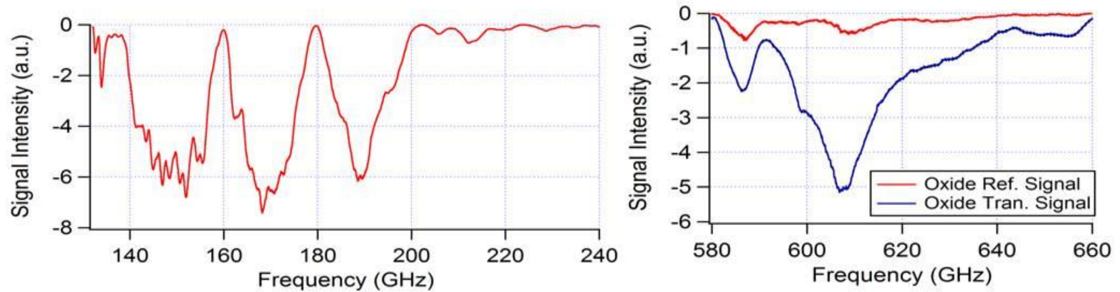

Figure 16: Raw Oxide/Oxide reflection (red)/transmission (blue) spectra from the 200 GHz system (left), and the 600 GHz system (right). The 200 GHz system exhibited a much higher standing wave visibility than the 600 GHz system.

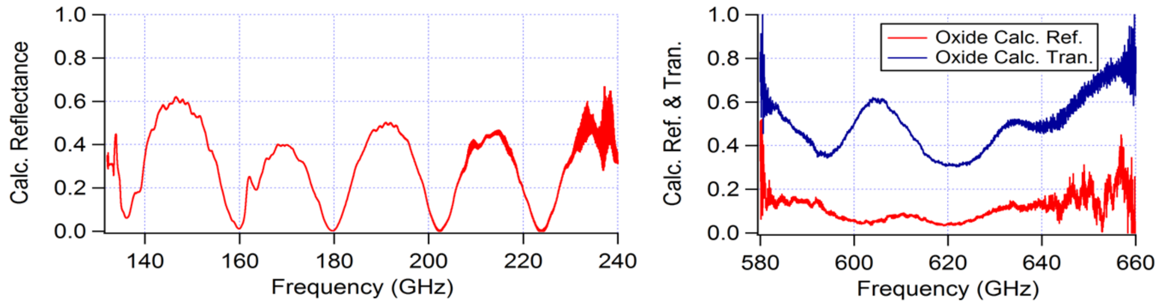

Figure 17: Plot of calculated reflectance/transmittance for the Oxide/Oxide CMC. These plots were smoothed using a box smoothing technique to enable the fitting formula to better fit the standing wave.

Initial attempts were made to determine the complex index from only the 200 and 600 GHz spectra. These attempts did not consider the visibility term in the fitting formula, and there was no initial guess to use for the complex refractive index. Thus these fits were made without any predetermined understanding of what to expect. Using the 600 GHz data provided some difficulties which must be explained, beyond the small usable frequency sweep of data. First, the transmission and reflection scans showed inconsistencies. The spectra for a sample sometimes

exhibit a large transmittance (~.60), and other times a low transmittance (~.20). The macro structure of the CMC material and spot size of the system provide possible explanations for this phenomena. It is possible that the radiation spot size was small enough to fit in between the initial weave layer, as evidenced in Figure 8. If this was the case, the measures were actually optically sampling the different components of the composite material, instead of the optical properties of the complete composite macrostructure, or just simply a thinner sample. Another possible reason for these inconsistencies could be the expansion of the beam size in the material. The reflectance system was designed to reflect off the front surface of the material, thus this location was always at the same location in the Gaussian beam profile. Depending on the thickness of the material, the back surface of the material could have very well been outside the Rayleigh range of the Gaussian beam waist leading to a very low coupling of the power off of the front and back material surfaces. As mentioned in the last chapter, expansion of the beam in a material would lead to a decrease in the visibility of the sample's standing wave. It is probable that these effects, as well as others discussed in the next few paragraphs, contributed to the inconsistency of these measurements. Figure 18 shows the fitted waves. It was expected that the reflection and transmission waves would be 180° out of phase. The fitting formula did not track phase thus the data fits did not necessarily reflect this phase shift.

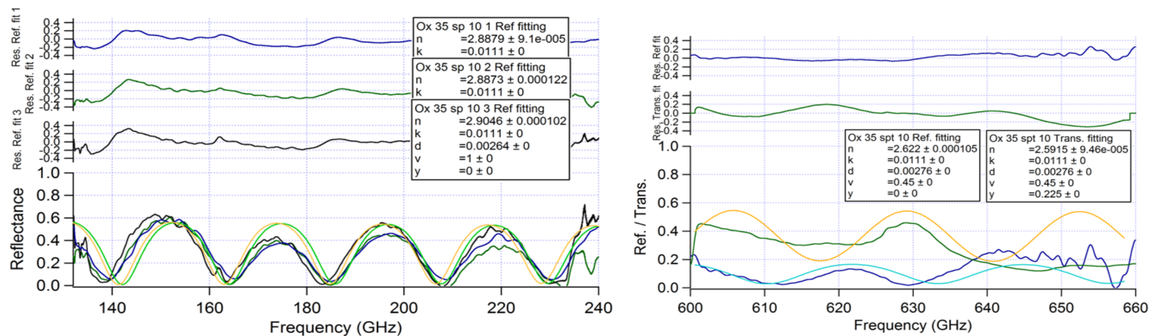

Figure 18: Oxide/Oxide fitting results with residuals. For the 200 GHz system there were 4 to 5 periods to fit. For the 600 GHz system the reflected beam usually had 2 to 3 periods to fit, for the transmitted beam it was usually less. In both cases the residuals for the 600 GHz fits were of the same order.

The CW400 results, shown in Figure 19, presented their own set of difficulties. This system was used to collect transmission spectra from 100 to 800 GHz on multiple days. Initial measurements

were made with a frequency resolution of 275 MHz while the remaining measures were made with a frequency resolution of 150 MHz. The resulting FFT of these scans show the presence of the standing waves between the Tx/Rx heads and the sample, but not the material standing wave as seen in similar FFT's for the 200 and 600 GHz systems. As seen in the modeling chapter, the amplitude of the material standing wave was greatly reduced as a result of the poor coupling of the Gaussian beam traveling through the material. The result of this reduced standing wave visibility made fits using the adjusted transmittance model nearly impossible and provided very divergent results when they were made.

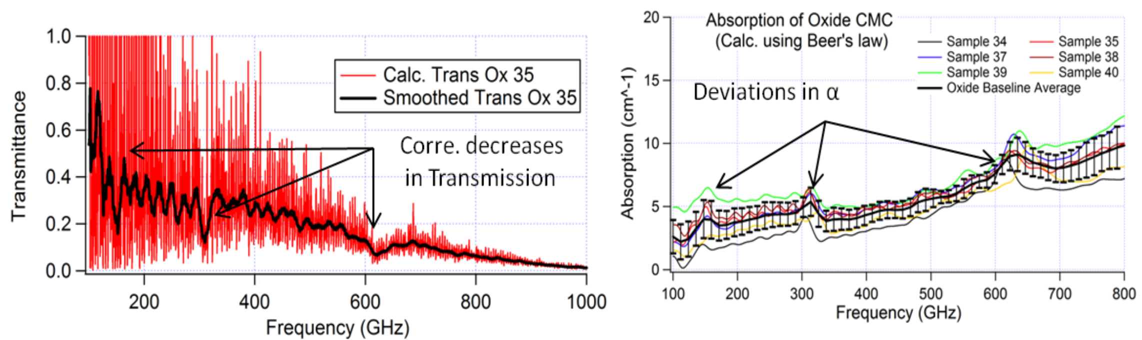

Figure 19: Transmission and corresponding absorbance (α) values for the baseline samples. One interesting feature of these measures was the decrease in transmittance at 160, 300, and 600 GHz. These drops in transmission did not occur in similar measures of HDPE, or other reference measures leading one to believe these features are real in the Oxide/Oxide spectra.

Transmittance was found by dividing the material transmitted spectra by the system measured spectra as seen in Figure 19. As with the rest of the spectra gathered for this project, a box smoothing technique was used to decrease the noise in these measurements. As a first order approximation to the value of kappa (κ), the imaginary index of refraction, the absorption coefficient (α) found using Beer's law from this transmittance data was used. The relationship between κ and α is found in Equation 20. The problem with this approximation is that Beer's law does not take Fresnel's loss, or the material's reflectance into account, thus the α found using this relation was artificially high. Subsequent steps were used to understand the true absorbance of the material in terms of κ the imaginary part of the complex index of refraction.

Thus, finding the complex index of refraction was an iterative process. This was because there were three different sets of data. Also, it was found that the fitting formula was very sensitive to the real index changes, but very insensitive to changes in kappa. When fitting data for both quantities with limits on both n and κ, it was found that the fitted κ had values ranging over an order of magnitude. There are many papers which discuss pulling these quantities from transmission and reflection data [28, 17, 5]. Many of these methods deal with known material properties or apply the spectra to an existing solid state model, none of which apply to these materials. The method of solving for the complex index is as follows:

1.) Beer's law without the Fresnel correction was used to find the absorption coefficient for the Oxide measured spectra. The relationship relating absorption coefficient (α) and wavelength (λ) to κ is found in Equation 20 [4].

$$\kappa = \lambda\alpha/4\pi \qquad \textbf{Eqn. 20}$$

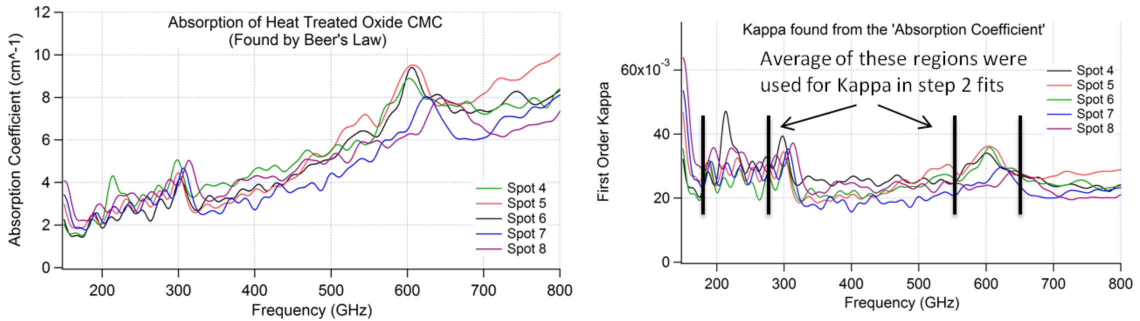

Figure 20: First order approximation of the kappa for the heat treated Oxide/Oxide sample. As noted this absorption was found from the CW400 transmission using Beer's law. This method resulted in a first order approximation of κ (Eqn. 20). Averages of this 'κ' waves near 200 and 600 GHz were used for κ in step 2.

2.) Using the κ wave found in step 1, a segment around 200 and 600 GHz was averaged and selected as the κ value to be utilized in the modified reflection and transmission formulas (Eqn. 15). These formulas were applied on a small subset of the data from 200 and 600 GHz system data. This small subset coincided with the scanned samples measured in the CW400 system. From these fits, the real part of the index for 200 GHz and 600 GHz

were found. In this fitting, everything was held fixed except for the real part of the complex index.

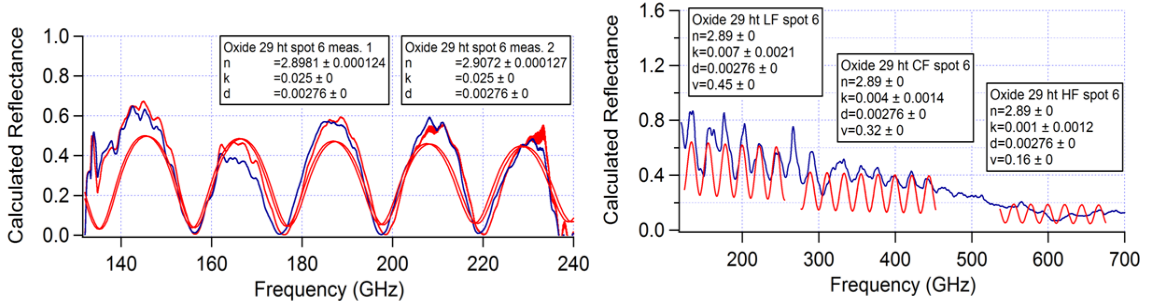

Figure 21: Fitting of the 200 GHz reflection and the CW400 transmission data. The 200 and 600 GHz data was used to determine the real part of the index of refraction and the CW400 spectra was used to find the imaginary part of the index of refraction (κ). In this process it was found that the reflectance and transmittance models reacted very little to changes in κ. This process was completed on the 27 spots sampled with the CW400.

3.) Using the real index of refraction values found in step 2, the modified transmittance formula was used to fit the CW400 data over the 200 and 600 GHz region of data. In this fitting everything was held fixed except the κ (kappa) values. These κ's were compared to the κ's found in step one. After this step, if the two κ values were found to be statistically different, the process required going back to step two with the new κ values. This happened a couple times until the two κ's were found to be insignificantly different. Table 2 shows the evolution of kappa as a result of these steps. As seen in Figure 21, fitting for kappa proved difficult due to the reduced visibility of the standing wave at high frequencies. Due to this effect fitting for kappa was not possible beyond 300 GHz. As stated earlier the Oxide material model was very insensitive to changes in κ, and making these fits required placing limiting values on κ. If a fit for κ resulted in this limiting value that wave was no longer used in the process.

		Step 1 1st step	Step 3 -1 3rd step	Step 3 - 2 3rd step 2
Heat treat	200 GHz	0.028 (003)	0.062 (028)	0.019 (010)
	600 GHz	0.027 (003)	0.078 (044)	
Dwell	200 GHz	0.052 (007)	0.033 (011)	0.017 (010)
	600 GHz	0.032 (003)		
Strain	200 GHz	0.033 (003)	0.087 (067)	0.011 (004)
	600 GHz	0.028 (004)		
Baseline	200 GHz	0.041 (011)	0.027 (021)	0.012 (009)
	600 GHz	0.029 (003)		

Table 2: Kappa (κ) values from the CW400 spectra 1st step data was found using Beer's Law, 3rd step found using the adjusted transmittance formula (Eqn 15). In most cases these fits resulted in a pre-determined minimum value. These values were thrown out reducing the sample size of κ values.

Because of this rule the number of κ's in the final iteration of this process was the minimum possible, three, leading to the aborting of this process. The general trend that was noted in making these fits was that κ settled to the minimum value in this fitting process, meaning that this value was very insignificant and could easily have been set to zero.

4.) Once a κ value was found it was used in the modified reflectance and transmittance models to fit all of the samples. In this fitting, as before, a visibility was chosen and everything was held fixed but the real part of the index. These are the results that will be reported for the Oxide/Oxide CMC sample.

One question that is often asked when examining these spectra is why there was not another material standing wave associated with the ply thickness. The CMC's studied were made of a stack of eight woven ceramic matrices that were joined together using a separate material. It is expected that the refractive index of the ceramic matrix will be different than that of the joining material, but the magnitude of this index change will be much lower than that of the air / material surface. Thus the Fresnel reflection (Eqn. 3) at these interfaces will be much weaker than at the exterior material interface. It is expected that the visibility of this wave will be very weak when compared to the full material standing wave that was detected. Also if such a standing wave was visible it would be over a much longer frequency, as the etalon formula (Eqn. 4) would still hold. The only system that could fully resolve such a wave would be the CW400 system, but the visibility of these spectra was so low that such a standing wave would have been hidden by system noise. Another reason may stem from the fact that the baking / pressurizing process utilized in making the CMC is actually a chemical process. As such the plys are forming bonds, and the materials are actually joining to form one material. The most probable reason stems from the fact that these measurements were with long wavelength light, thus the phase shift from a multiple reflected beam is very small and the interference pattern is not seen. It is expected that

changes in the etalon pattern will occur once these materials start to separate or have sharp and distinctive boundaries. This was seen in the initial measures made on the initial broken samples provided at the start of this project. Also, as the ply's separate a different optics problem forms as one would then see two thin samples with a void in between. One very interesting thing to note is in all of the 200 GHz Oxide spectra the visibility of the material standing wave is greatly decreased at ~160 GHz, for example see Figure 21 left side. The expected standing wave for one ply is 160 GHz, as the ply thickness is on the order of 0.34 mm. This decrease in reflection at 160 GHz does not correspond to an increase in transmission at 160 GHz, as would be expected with a Fabry-Perot model of this material. It is expected that this noted decrease in reflection is due to absorption / scattering behavior related to the weave density and will be further analyzed in the next chapters.

With this understanding of these materials and our measurement techniques, the next chapter will discuss the measurement results for each material, and if the differences are statistically significant.

V. Measurement Results

The last chapter went into detail as to how these results were determined from the reflectance and transmittance measurements. This chapter discusses the results of these measurements, and compares the various treated CMC samples to the CMC sample baseline measurements. In this analysis, a series of hypothesis tests were used to evaluate if the means associated with the treated samples were different than the baseline samples. To complete these tests, the Student T-test was used. This test allows one to compare statistics from two different sized sample sets (Devore, 2004). This style of test results in a calculated t-value seen in Equation 21. The t value has an associated degree of freedom, and corresponds to a normalization of the set to a Gaussian distribution [3, 9]. A standard Gaussian distribution has a mean centered at zero, thus the t-test takes the data which has a mean at value A, and transforms it to zero. Thus α is the location of one mean related to another in terms of the standard Gaussian distribution. Alpha (α) describes the probability of the two means used in the test are different in terms of the normalized Gaussian curve. For a t-test with an α value of greater than 0.05, the separation between the two means is not significant, leading one to accept the hypothesis that $\mu_A = \mu_B$ otherwise this hypothesis would be rejected [3, 9].

$$t_\nu = \frac{\bar{x}-\bar{y}}{\sigma_{\bar{y}}+\sigma_{\bar{x}}} \quad \textbf{Eqn. 21}$$

In Equation 21, $\bar{x}$ and $\bar{y}$ are the average values for the two datasets to be compared; $\sigma_{\bar{x}}$ and $\sigma_{\bar{y}}$ are the standard error, seen in Equation 19, associated with the above average values. Finally, t_ν is the t-test value with the associated degree of freedom [3]. To use Equation 21 $\bar{x}$ would be the mean associated with the baseline samples, and $\bar{y}$ the mean associated with the stressed sample.

Equation 19 was used to compare multiple samples together and equals Equation 18 for a single sample. Thus the calculation of $\sigma_{\bar{x}}$ is based on multiple samples, and $\sigma_{\bar{y}}$ is based on the single stressed sample. The test degree of freedom for a t-test was determined summing the number of measures in each group and subtracting two [3, 9]. For the SiC/SiNC measures the t-value was calculated based on the measured material front surface reflectance. For the Oxide/Oxide t-value the comparisons were made using the calculated material front surface reflection, using the Fresnel reflection coefficient seen in Equation 3. Thus these calculations were made after finding the material complex index of refraction.

The three specific stressed treatments were applied to a subset of the samples that were then compared to the baseline measures. One treatment was applying a thermal load to a sample where a CMC sample was heated for a number of hours; introducing a thermal stress into the sample. Another treatment was made by applying a bending stress to the length of the sample with this load reversed for a number of repetitions, introducing a strain into the sample. Lastly, a dwell test was completed. This test consists of applying a stress and holding that stress while heating the sample. Due to the nature of this test the heat was maintained to the specified heat value at the central spot of the sample, but was not constant over the entire length of the sample also termed as a thermal gradient. When looking at the dwell treated spots no specific trends were detected due to this thermal gradient. If there was an effect due to the thermal gradient it would be expected that the central spot would have the least reflectance, and the outside spots would have higher reflectance's which was not seen in the sample that was tested. For this analysis the central nine spots were combined and viewed as one sample even though they received slightly different amounts of thermal load. The following table described the particulars about these different treatments. Most of these stressed samples were evaluated in the 600 GHz system due to the dates the stressed samples were returned to Wright State.

	Oxide/Oxide	SiC/SiNC
Heat Treat	1000˚C & 1100˚C for 100 Hrs	1000˚C for 10 & 100 Hrs
Strain Treat	280 MPa for 1000 rep.	225 MPa for 1000 rep.
Dwell Treat	1100˚C & 40 MPa for 40 rep. 15 min dwell time each repetition	1200˚C & 150 MPa for 40 rep. 15 min dwell time each repetition

Table 3: Table of treatment amounts applied to the Oxide/Oxide and the SiC/SiNC CMC samples

The front surface reflectance was found for these stressed samples with the null hypothesis being that the means of the stressed sample were the same as the baseline sample. These tests would be rejected if α associated with these t-tests were ≤ 0.05. Otherwise this null hypothesis would be accepted meaning that this level of stress would be insignificant to measure as a NDE technique.

5.1. SiC/SiNC Results

For the baseline SiC/SiNC measurements the base reflectivity was found to be 0.320 ± 0.005 at 200 GHz, and 0.33 ± 0.03 for the 600 GHz measures. A plot of the baseline reflectivity is shown in Figure 22. Figure 23 shows the stressed samples. The averages and standard deviations found in Table 4 were gathered using average of the flat portion of these curves. For the 200 GHz data this extended from 135 to 230 GHz, and 580 to 630 GHz for the 600 GHz system. As expected these values change very little with frequency, evidenced in Table 4. The only deviation from the frequency invariance of the reflectance is seen in the strained SiC/SiNC sample. The strained sample measured at 200 GHz was different then the strained sample measured at 600 GHz. This particular case shows the importance of having continuous spectra for a sample throughout the life of the CMC part. Lastly, it was very interesting to see the effects on the dwell treated sample. As this sample received both treatments one could expect the reflectance to be greatly decreased since reflectance decreases for the thermal and strain stress type separately. This did not occur; leading one to ask if the mode of failure due to heat stress is the same as for mechanical stress. Looking at the stressed samples in Figure 23, it is evident that there was a reduction in the signal to noise ratio for the 600 GHz system. To quantify differences

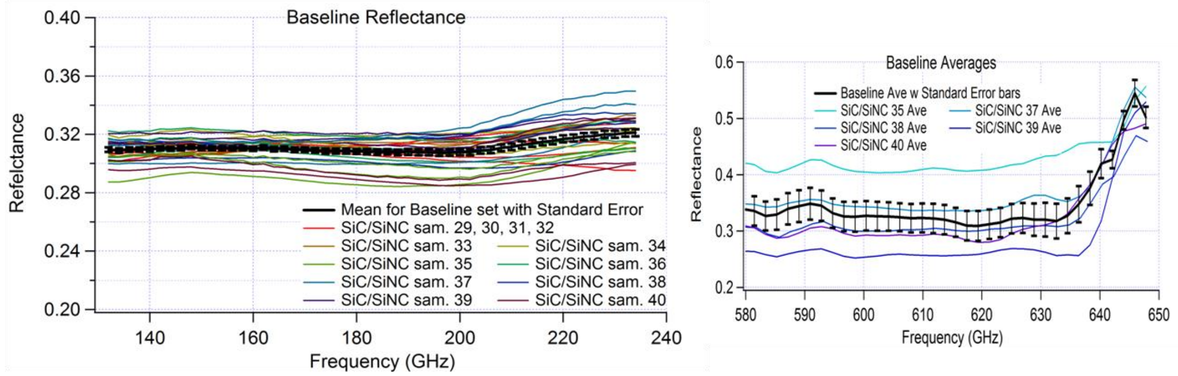

Figure 22: Plots of the baseline reflectance for the SiC/SiNC CMC material.

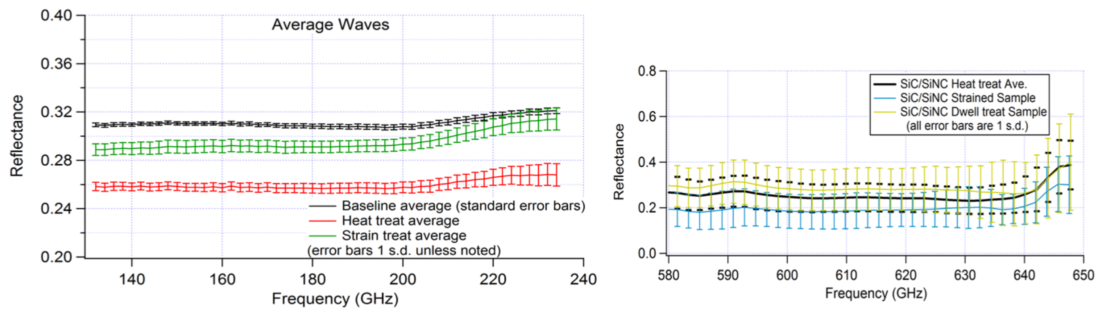

Figure 23: Stressed sample waves for the 200 GHz system (left), and the 600 GHz system (right).

between the stressed samples and the baseline samples, a series of hypothesis tests were made. In all these tests, the assumption was that the stressed and the baseline measures were considered equal. Using Equation 21 on the data in Figure 23 and 22, the t-values were found and shown in Figure 24. For the SiC/SiNC sample, all of the results were beyond the threshold of $\alpha < 0.05$ meaning the hypothesis $\bar{R}_s = \bar{R}_B$ would be rejected. The hypothesis tests that were evaluated were:

1. Heat treated average reflectance = Baseline average reflectance
2. Strain treated average reflectance = Baseline average reflectance
3. Heat treated average reflectance = Strain treat average reflectance (valid for 200 GHz only). This was not evaluated for the 600 GHz samples due to the similarity in values evidenced in the right side of Figure 23.
4. Dwell treat average reflectance = Baseline average reflectance (valid for 600 GHz only)
5. Heat treat average reflectance = Untreated sample reflectance (valid for 200 GHz only)
6. Heat treat 100 hrs = Heat treat 10 hrs (valid for 600 GHz only)

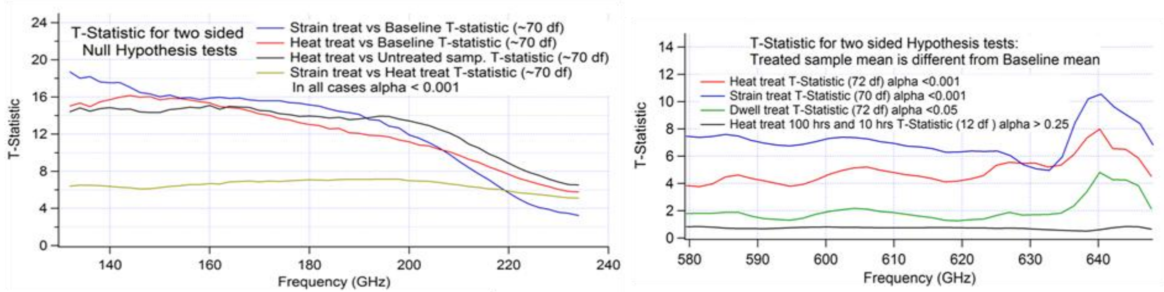

Figure 24: T-values for the five hypotheses tests completed on SiC/SiNC comparing the baseline and stressed samples. This test says nothing of the actual difference of these values, but if they are statistically similar or not.

In every one of these cases, the t-value was found to have a significant α associated with the exception of test 6. The significance of α is also a measure of how significant the difference between the means are. One definition of α is this variable tells how near, in Gaussian distribution terms, the two means are. By choosing an alpha value of ≤ 0.05 means the two Gaussian curves associated with the two means overlap in the tail regions of the distribution, thus for a significant α we must reject the hypotheses that the values are equal. From this analysis, it is shown that there is a significant difference between the stressed samples and the baseline samples. In the case of test 6, relating the 10 and 100 hour heat treated samples a non-significant α was found meaning that a NDE technique probably could not detect any difference between these values.

From this analysis, it appears NDE techniques may work for this material. Further work is necessary to determine how much these materials were stressed and if the reflectance will further decrease with further stressing, and if similar results are found with more samples. These results are based on one set of samples only. Figure 24, above, shows the t-values as well as the degree of freedom associated with this test. The associated α value can be found at the right end of the plot legends.

Average SiC/SiNC Reflectance				
	200 GHz		600 GHz	
	R_{ave}	σ_R	R_{ave}	σ_R
Baseline	0.311	0.002	0.326	0.027
Heat treated	0.260	0.005	0.248	0.063
Strain treated	0.296	0.006	0.191	0.078
Dwell treated			0.285	0.098

Table 4: Condensed SiC/SiNC results. Empty cells are for measures that did not occur. Strain treated samples were different for 200 and 600 GHz.

5.2. Oxide/Oxide Results

The Oxide/Oxide reflectivity was based on the complex index of refraction that was found for this material. By using Eqn. 3 the front surface reflectance could be determined. This reflectance excludes the effects of interference from the rear material surface. These samples had a front surface reflectance of 0.231 ± 0.003 in the 200 GHz region, and 0.201 ± 0.002 in the 600 GHz region. Table 5 and 6 show the 200 and 600 GHz measurements respectively. Similar hypothesis testing was completed to determine the significance in the shift between the stressed Oxide reflectance metric to the baseline Oxide metric. From these tests, it was found that the claim that the stressed and baseline reflectance's were equal had to be accepted. This statement is based on the fact that α has a value greater than 0.05. One caveat to this statement is that the residuals of the fitted model, which were non-negligible, were not included in determining the variance in the complex index of refraction and including these in the analysis could change this conclusion.

Oxide/Oxide 200 GHz Reflectance

	Reflectance:		Real part of index			Null Hypothesis $R_{Base} = R_{Treat}$		
	Value	σ_R	Ave:	σ_n	Kappa:	T-statistic	df	$\alpha_{Two\text{-}tailed}$
1st Heat treat	0.240	0.003	2.921	0.023	0.0193	1.44	70	< 0.20
2nd Heat treat	0.236	0.001	2.886	0.005	0.0193	1.12	< 100	< 0.30
Baseline	0.231	0.003	2.854	0.024	0.0111			
Sample 29	0.237	0.010	2.895	0.076				

Table 5: Front surface reflectance values for the Oxide/Oxide CMC at 200 GHz.

Oxide/Oxide 600 GHz

	Reflectance:		Real part of index			Null Hypothesis $R_{Base} = R_{Treat}$		
	Value	σ_R	Ave:	σ_n	Kappa:	T-statistic	df	$\alpha_{Two\text{-}tailed}$
Heat Treat	0.210	0.005	2.689	0.033	0.0193	1.47	12	< 0.40
Strain Treat	0.194	0.002	2.575	0.015	0.0109	1.71	25	< 0.10
Dwell Treat	0.208	0.003	2.674	0.019	0.0173	1.63	18	< 0.15
Baseline	0.201	0.002	2.623	0.012	0.0111			

Table 6: Front surface reflectance values for the Oxide/Oxide CMC at 600 GHz.

One aspect of the Oxide/Oxide spectra that has not been considered was the decrease in transmission seen in the CW400 measured results at ~160, 300, and 600 GHz. These features were not expected and could be results of resonant scattering (i.e. a diffraction grating) set up by the fiber grid in the material. The reasoning for this explanation stems from the sub-wavelength spacing of the weave pattern, and the fact that these decreases in transmission are evenly spaced, 140, and 300 GHz apart. Therefore the 160 to 300 GHz 'absorption' is associated with distance between the weaves, and the 300 to 600 GHz absorption is associated with the distance between the plys. These effects are shown in Figure 25 to 27 which show these features measured in the stressed and the baseline data and include the statistics of these features. It is hoped that these features maybe useful for possible NDE feature characterization. Initial scans with the CW400 system characterized the 100 GHz region. Subsequent scans in an effort to save time did not make measurements of this frequency region. As a result of this choice, the 160 GHz feature is not defined in the baseline and the dwell treated sample measurements. Again, the stressed sample results are based on one sample where the baseline samples are based on multiple samples thus the smaller variance in the stressed samples could be due to this fact alone. The fact that these features exist in this spectra explains many of the interesting features seen in the 200 and 600 GHz measurements. First, the 160 GHz feature explains the decrease in the standing wave amplitude measured in the 200 GHz reflection spectra. This decrease in the reflection was seen at approximately 160 GHz, thus it was most likely due to this feature. Also the erratic spectra gathered with the 600 GHz system is due to the widely varying feature which was centered at 612 GHz and varied by ~15 GHz.

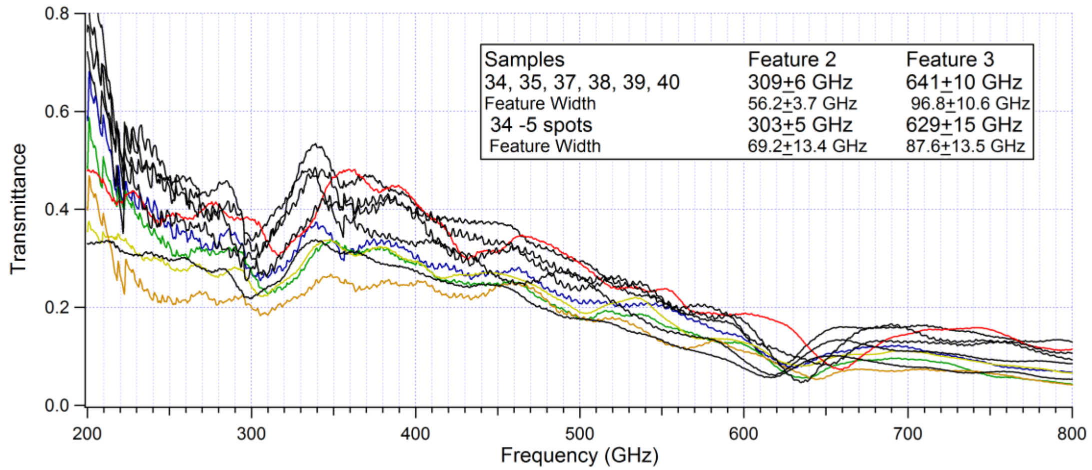

Figure 25: Baseline samples with the statistics of the features. All figures show the first line with the average central frequency, and the standard deviation of the frequency, the second line has the average width of the feature, and the standard deviation of the feature width.

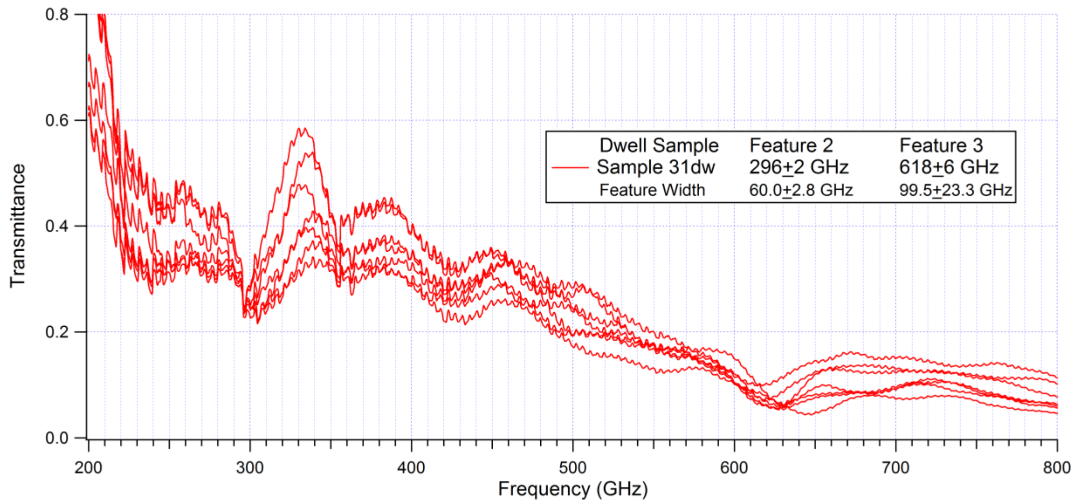

Figure 26: Dwell treated sample with the features defined.

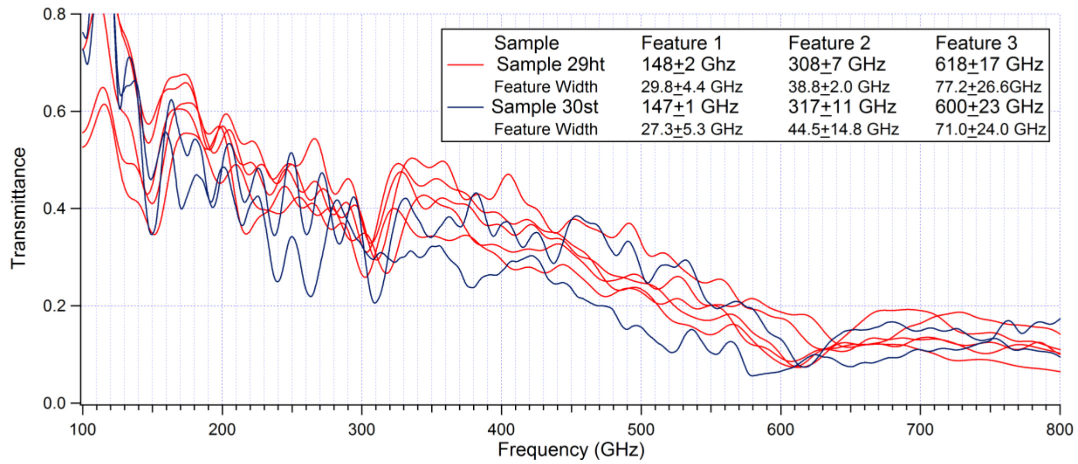

Figure 27: Strained and heat treated features defined measurement made with ~300 MHz resolution.

5.3. Discussion

From the hypothesis testing, the SiC/SiNC stressed samples were found to be significantly different than the SiC/SiNC baseline samples. For the Oxide/Oxide samples, this was not found to be the case. Possible reasons for this could be the result of errors inherent in the refractive index fitting process in its inability to capture the salient changes. Features found in the CW400 show promise in the further development of NDE techniques for these materials. Appendix A shows a complete set of SiC/SiNC reflectance plots, and a complete set of the fitted Oxide/Oxide real index values, and a list of the reflectance values sorted by sample.

VI. Summary and Conclusions

This thesis discussed measuring the optical properties from two CMC materials: Oxide/Oxide and SiC/SiNC. Both of these materials had a weave pattern on the material surface with a structure repetition rate of approximately 4 mm. These materials were characterized in a 200 GHz reflectance measuring system and a 600 GHz reflectance/transmittance measuring system. These systems propagated a collimated radiation beam to an off-axis parabolic mirror which was used to focus the radiation on to the material surface. The beam spot size for the 200 GHz system was ~4 mm, and ~1.2 mm for the 600 GHz system. The location of the front material surface was located at the focal point of these radiation beams. From the 200 GHz system measurements, it is assumed that the sample was fully in the Rayleigh range of this system which resulted in a highly coupled standing wave (etalon) pattern in the data. The reduced visibility of the etalon in the 600 GHz measurements show that there was poor Gaussian beam coupling between the front and back material surfaces. The reason for this poor coupling was the material's thickness was larger than the systems Rayleigh range. Using this system, reflectance measurements were made at 200 GHz and reflectance/transmittance measurements were made at 600 GHz for the Oxide/Oxide CMC material, and reflectance spectra were collected for the SiC/SiNC CMC material. Lastly, a continuous wave system was used to collect transmission spectra from the Oxide/Oxide materials from 200 to 800 GHz. Using all the spectra from these systems, the complex index of refraction for the Oxide/Oxide material was found and the front surface reflectance of the SiC/SiNC material was found.

In this thesis, models were discussed to describe the reflectance off the front surface of the SiC/SiNC material, the front and rear surfaces of the Oxide/Oxide material and to describe the

visibility of sample standing waves in an optical system with varying coupling optics. Using these models, the material standing wave of the measured Oxide/Oxide spectra was fit for the complex index of refraction. The material model of the SiC/SiNC material, which consisted of dividing the material spectra by a system reference, described the measured reflectance of this material. After propagating error through the system, it was found the baseline SiC/SiNC reflectance to be 0.33 ± 0.03 for both the 200, and 600 GHz measures. The Oxide/Oxide material had a front surface reflectance of 0.231 ± 0.003 at 200 GHz, and 0.201 ± 0.002 at 600 GHz. The reflectance was determined by using the Fresnel equation for normal incidence on the front material surface using the fitted complex index of refraction that was found. When comparing the baseline reflectance's to the stressed samples, the Oxide/Oxide stressed samples were found to be insignificantly different from the baseline sample by a series of hypothesis tests using the Student t-test. This null result could very well be due to the fitting procedure that was necessary to implement due to the significant etalon patterns present in the data. Further analysis of the Oxide/Oxide residuals may result in the difference from the baseline to the stressed samples being significant; in the analysis that was completed for this thesis these residuals were not included in the variance of the refractive index. Using a similar t-test method, the reflectance from the SiC/SiNC stressed samples was found to be significantly different from the baseline reflectance. Also, a series of 'absorption' or 'scattering' features were identified in the CW400 transmission spectra of the Oxide/Oxide material at 160, 300, and 600 GHz. It is possible that these features are due to diffraction/scattering off of the CMC materials fiber matrix.

From these results, there is a possibility that reflection electro-magnetic NDE techniques can be developed for the SiC/SiNC material. Further work is needed to verify the relationship between the material fatigue or the remaining material life and the material reflectance. It is very interesting that there appears to be a trend of a stressed material having a lower material reflectance. Possibilities for this relationship could be a result of changes in the material

microstructure. No understanding as to the modes of failure for a heat stressed sample and a mechanical stressed sample were provided or found experimentally, but based on the results given, they very well could be similar. If these modes are similar then using reflection measuring method described in this thesis may prove to be a very interesting method to determine the in-situ state of the material due to both stressing factors, heat and strain, and thus provide an additive measure of material state. If these modes are different, further work is needed to understand why and if the measured reflectance drop will continue until material failure, or if this reflectance drop is a onetime phenomenon that happens with the first applied material stress.

APPENDIX A

Complete set of CMC data

SiC/SiNC Plots…………………………………………53

Oxide/Oxide Fit Data……………………………………67

Definition of the materials: (name on provided packages)

SiC/SiNC:

SiNC
S200H [0/90] 8 ply Hi-Nicalon SiNC
SS:L157 W12.5 for NDE study
17Q0001750 – xx | 11-Byy

- xx is the referenced sample number: 2, 29 to 40
- yy is sequential ranging from 60, 87 to 98
- Sample number '2st' was a mechanically strained sample supplied to WSU. We do not have a baseline measure of this sample.

Oxide/Oxide:

N610/AS [0/90] S
SS:L157 W 12.7
ATKC01C 1445-7-A-xx | 11-6yy

- xx is the referenced sample number: 29 to 40
- yy is sequential ranging from 12 to 23

SiC/SiNC 1st Heat Treat (1200° C for 100 Hrs.)

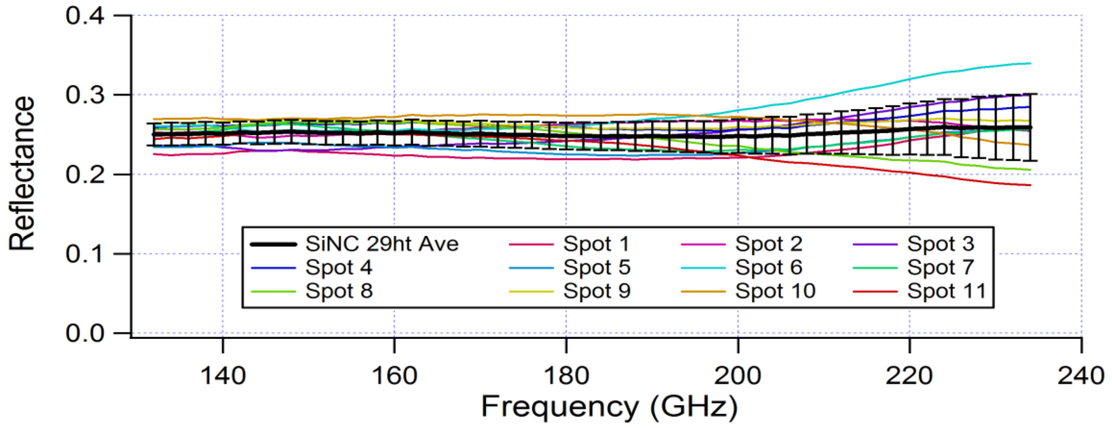

Figure A- 1: Heat treated SiC/SiNC sample 29 (B87) 1st measure 200 GHz

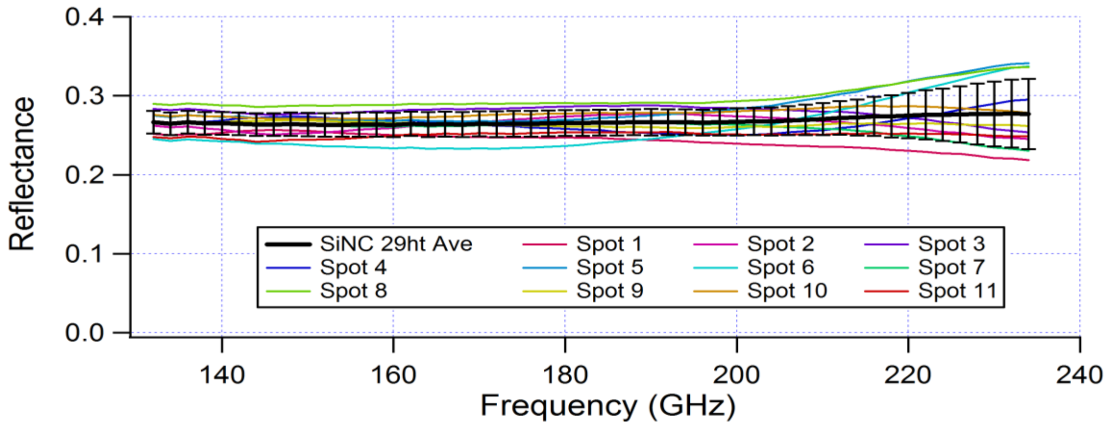

Figure A- 2: Heat treated SiC/SiNC sample 29 (B87) 2nd measure 200 GHz

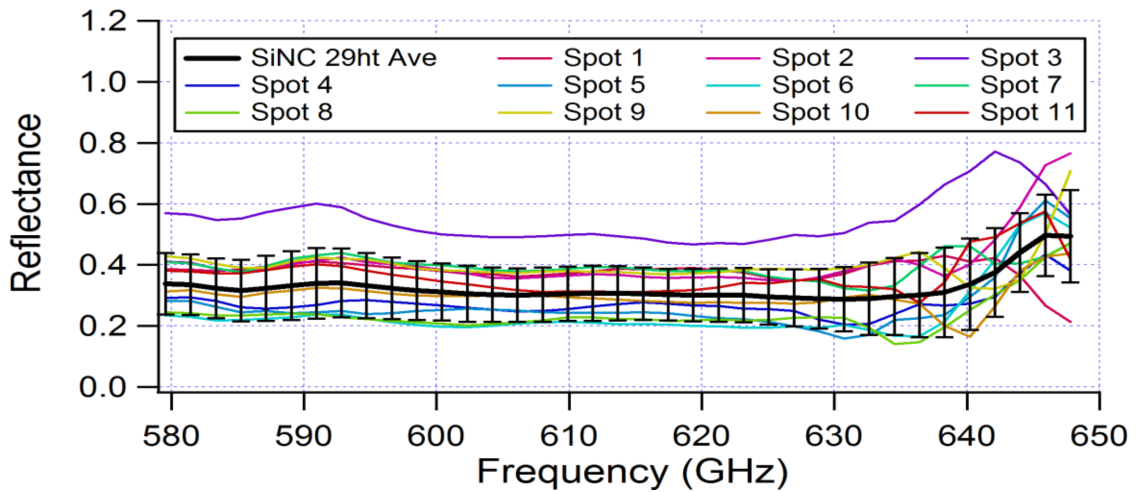

Figure A- 3: Heat treated SiC/SiNC sample 29 (B87) 600 GHz

SiC/SiNC 2nd Heat Treat (1200˚ C for 10 Hrs.)

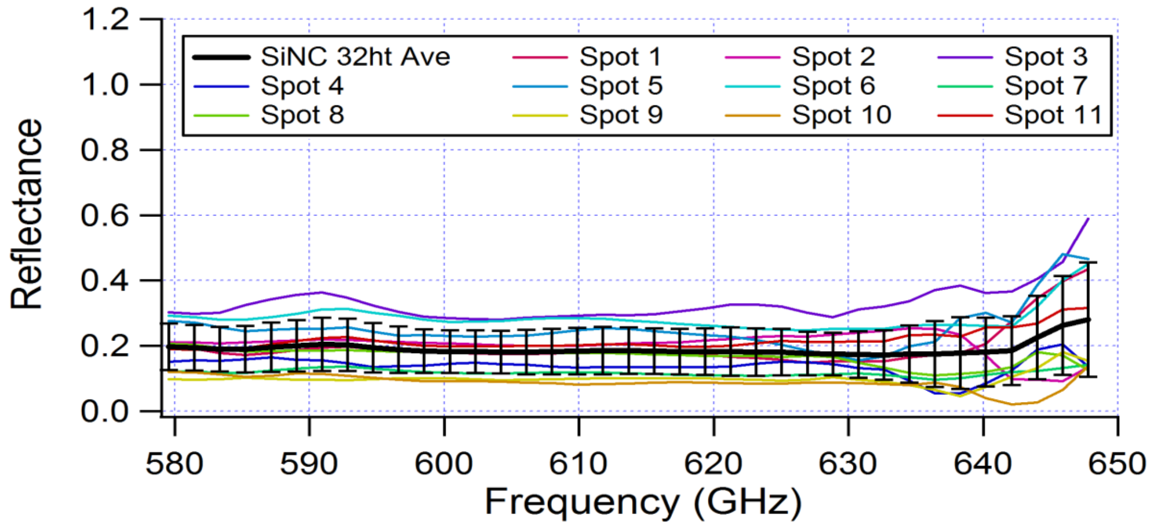

Figure A- 4: 2nd Heat treated SiC/SiNC sample 32 (B90) 600 GHz

SiC/SiNC Dwell Treated (Max. Stress = 150 MPa, R = 0.05, f = 1Hz, 1200˚ C 40 cycles for 10 hrs 15 min. dwell)

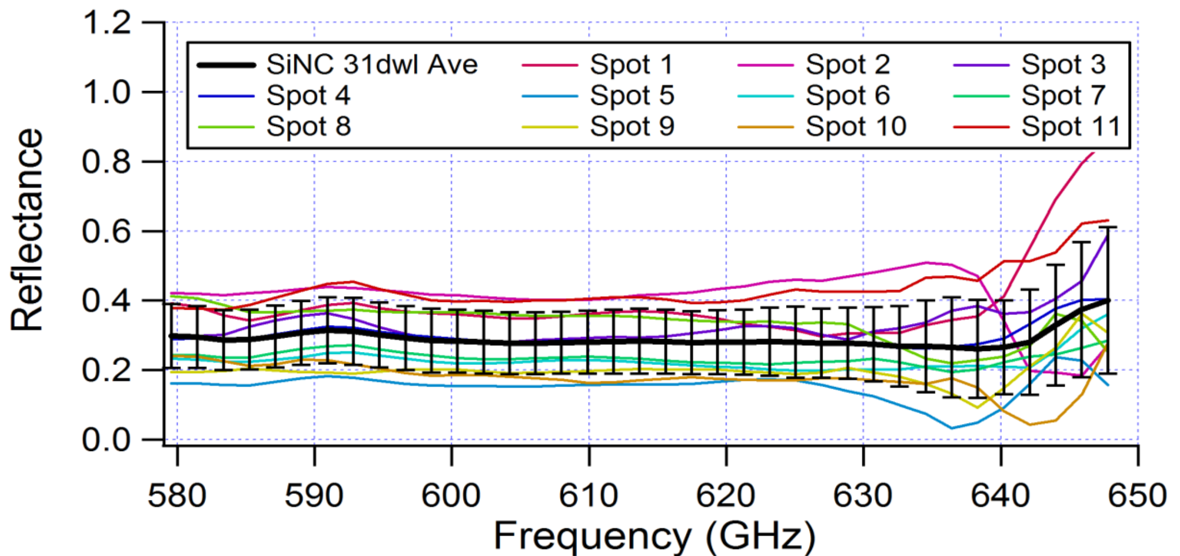

Figure A- 5: Dwell treated sample 31 (B29) 600 GHz

SiC/SiNC Mechanically Strained (Max. Stress = 225 MPa, R=0.05, N=1000, f = 1Hz)

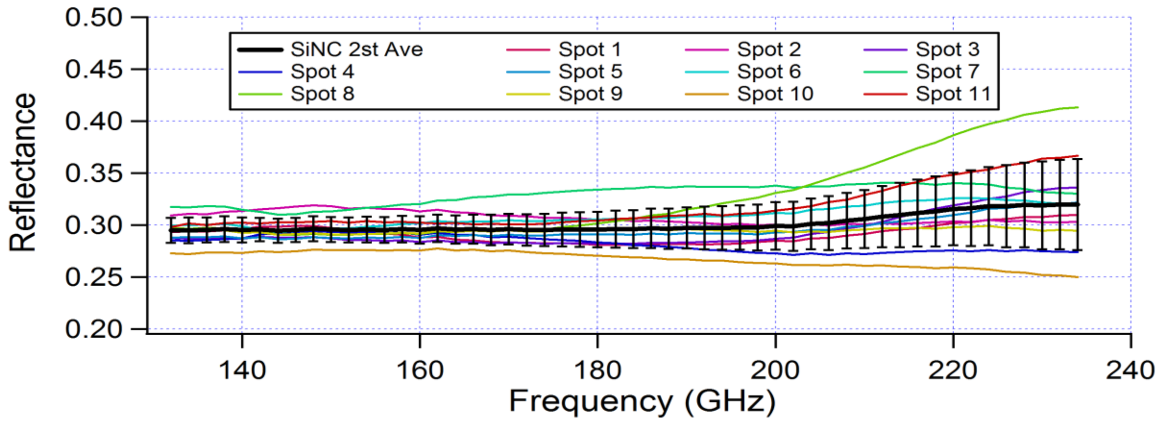

Figure A- 6: Strain treated SiC/SiNC sample 2 (B60) 1st measure 200 GHz

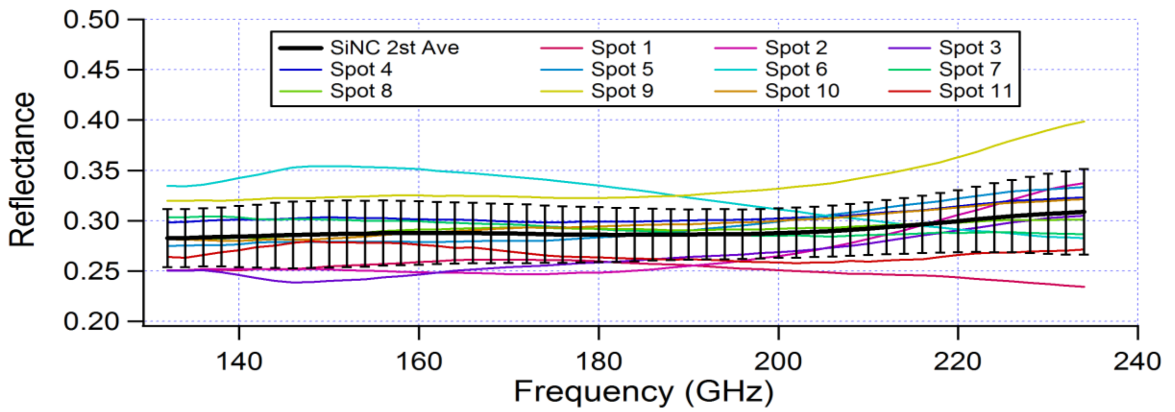

Figure A- 7: Strain treated SiC/SiNC sample 2 (B60) 2nd measure 200 GHz

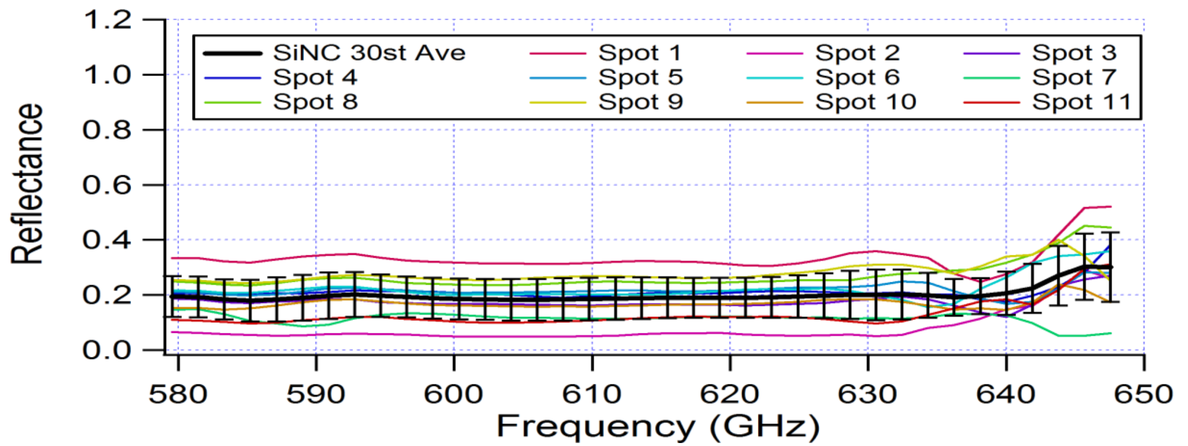

Figure A- 8: Strain treated SiC/SiNC sample 30 (B88) 600 GHz

Baseline SiC/SiNC Samples

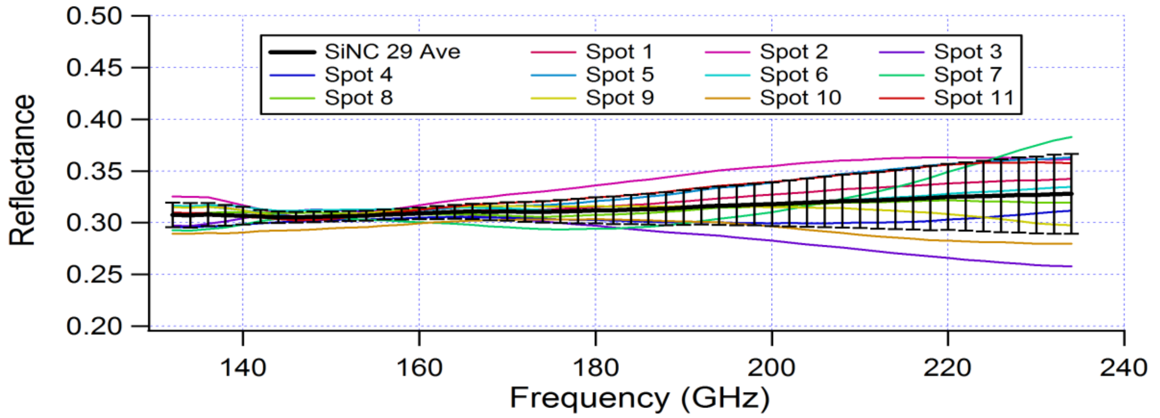

Figure A- 9: Baseline SiC/SiNC sample 29 (B87) 200 GHz

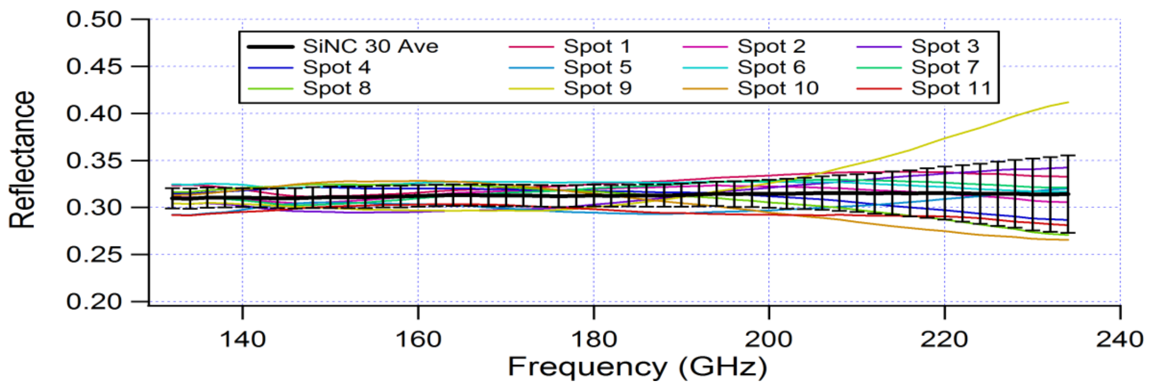

Figure A- 10: Baseline SiC/SiNC sample 30 (B88) 200 GHz

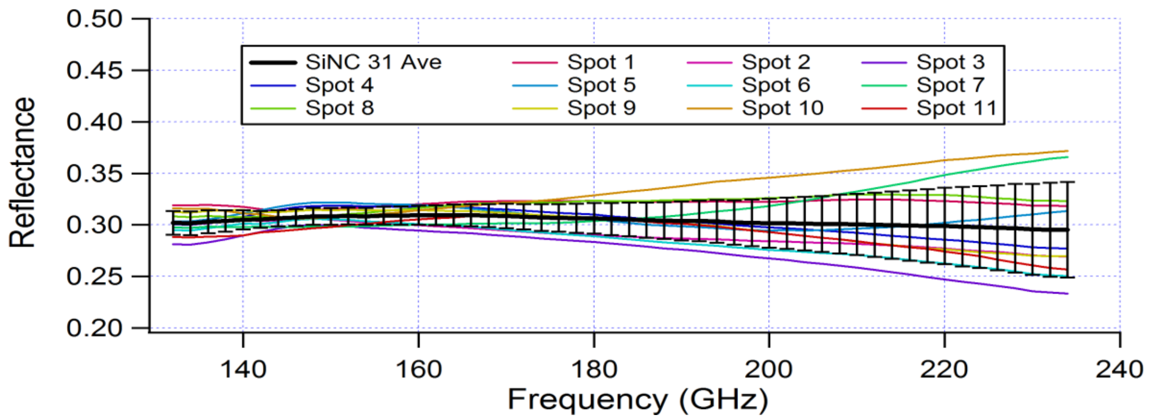

Figure A- 11: Baseline SiC/SiNC sample 31 (B89) 200 GHz

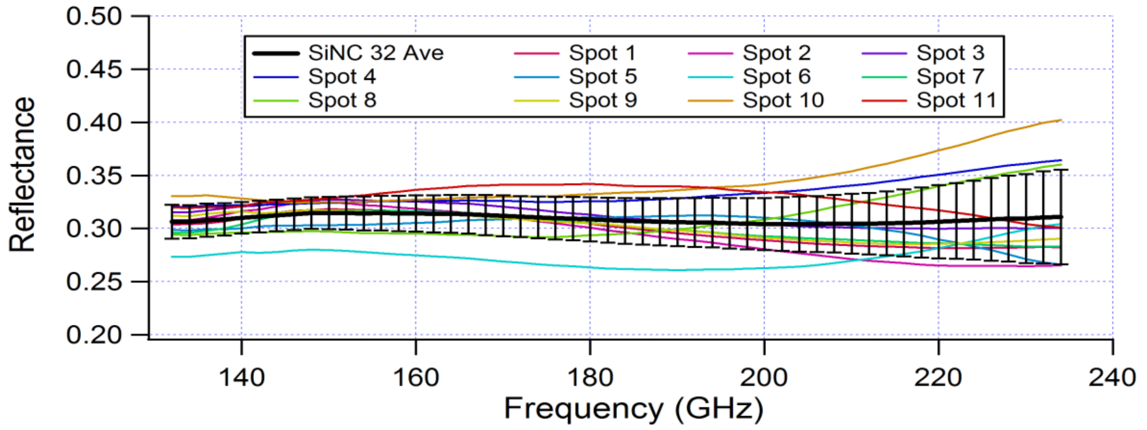

Figure A- 12: Baseline SiC/SiNC sample 32 (B90) 200 GHz

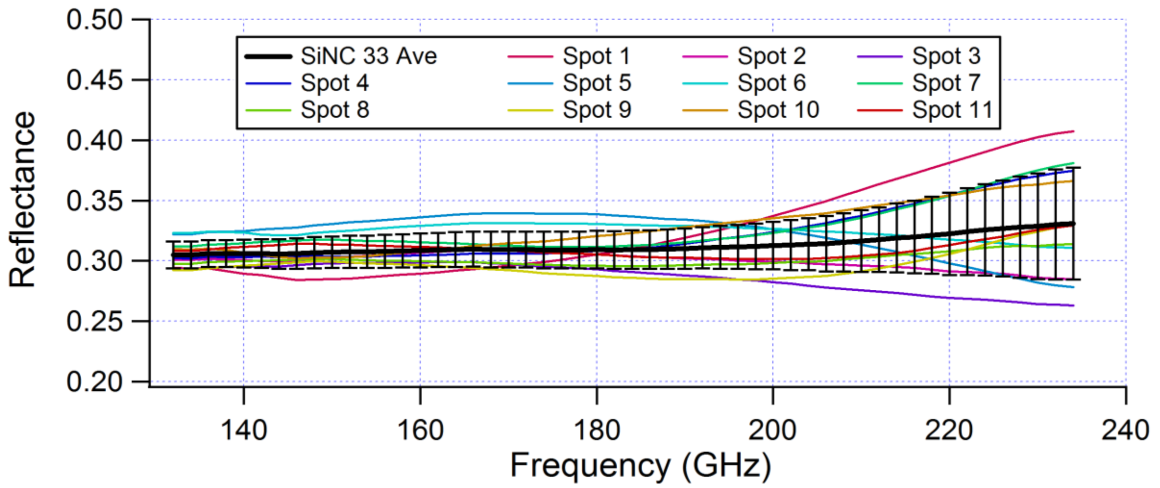

Figure A- 13: Baseline SiC/SiNC sample 33 (B91) 200 GHz 1st measure

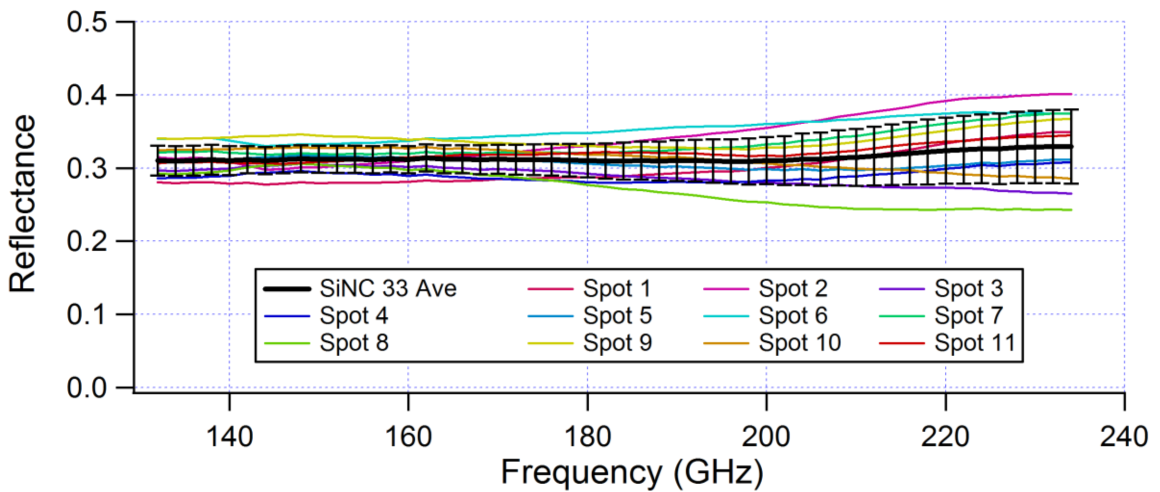

Figure A- 14: Baseline SiC/SiNC sample 33 (B91) 200 GHz 2nd measure

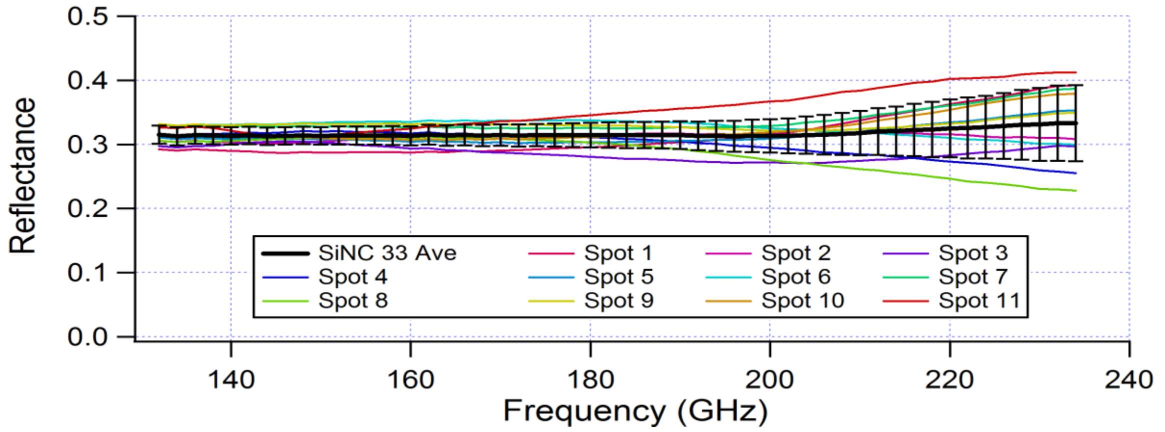

Figure A- 15: Baseline SiC/SiNC sample 33 (B91) 200 GHz 3rd measure

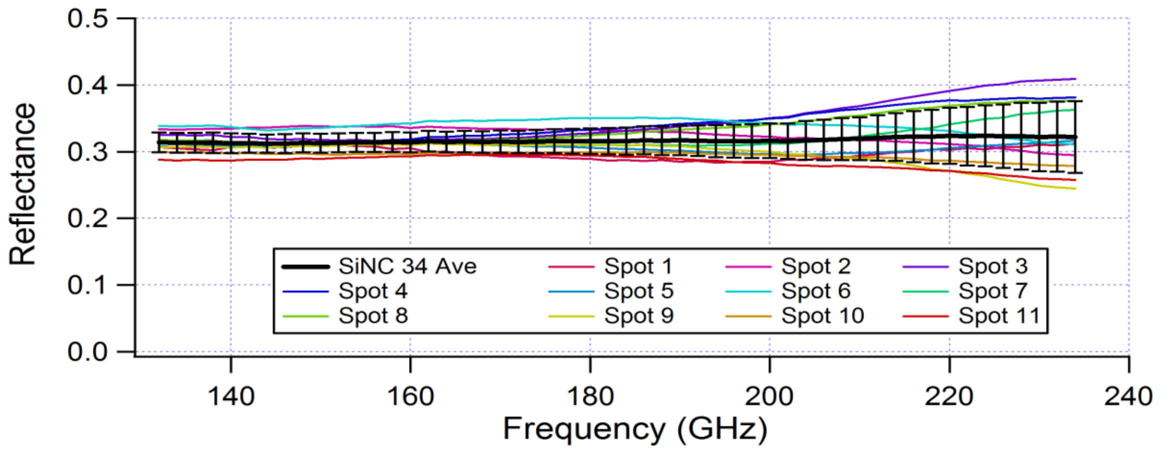

Figure A- 16: Baseline SiC/SiNC sample 34 (B92) 200 GHz 1st measure

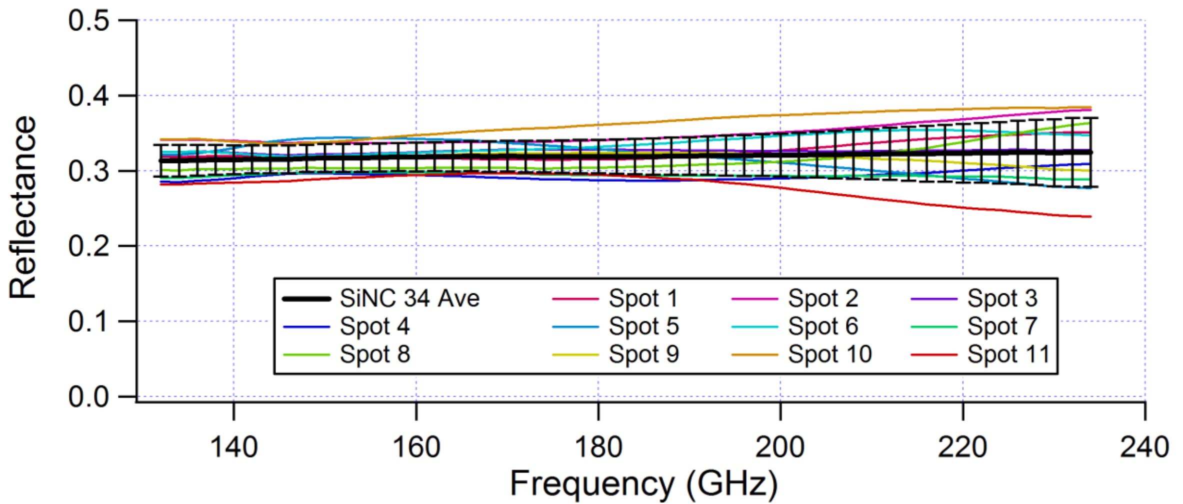

Figure A- 17: Baseline SiC/SiNC sample 34 (B92) 200 GHz 2nd measure

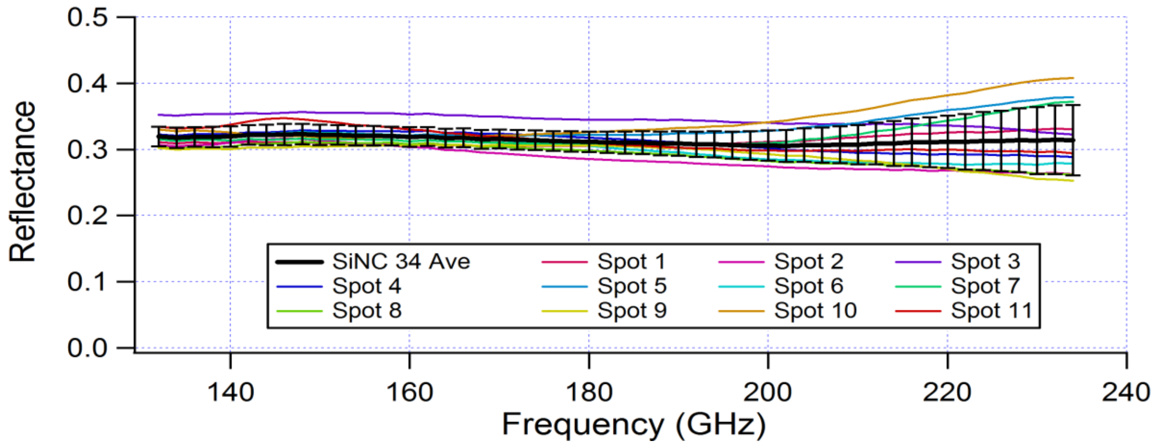

Figure A- 18: Baseline SiC/SiNC sample 34 (B92) 200 GHz 3rd measure

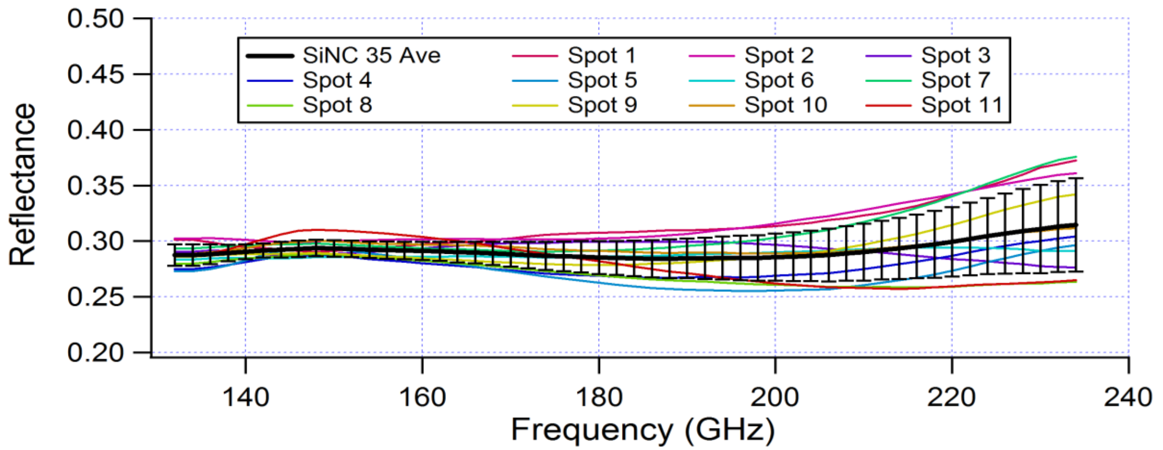

Figure A- 19: Baseline SiC/SiNC sample 35 (B93) 200 GHz 1st measure

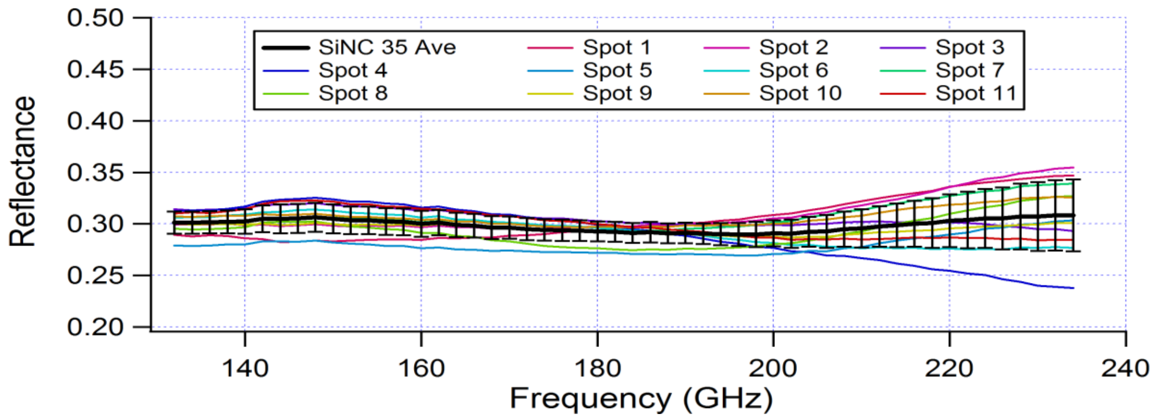

Figure A- 20: Baseline SiC/SiNC sample 35 (B93) 200 GHz 2nd measure

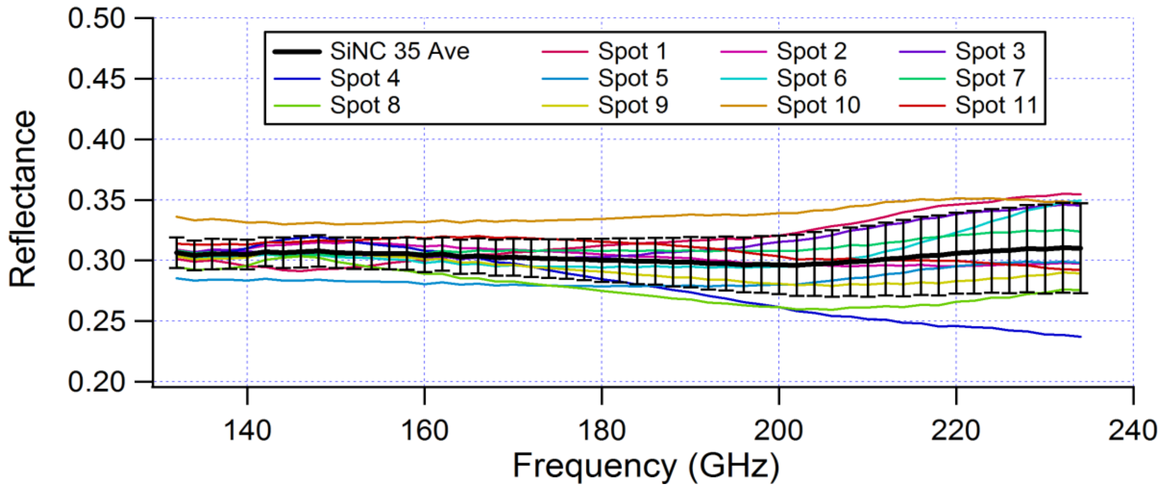

Figure A- 21: Baseline SiC/SiNC sample 35 (B93) 200 GHz 3rd measure

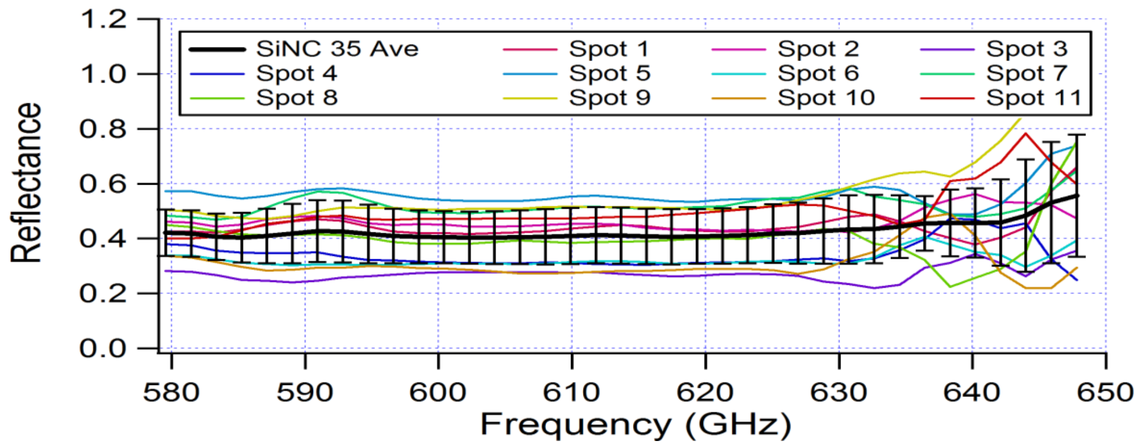

Figure A- 22: Baseline SiC/SiNC sample 35 (B93) 600 GHz

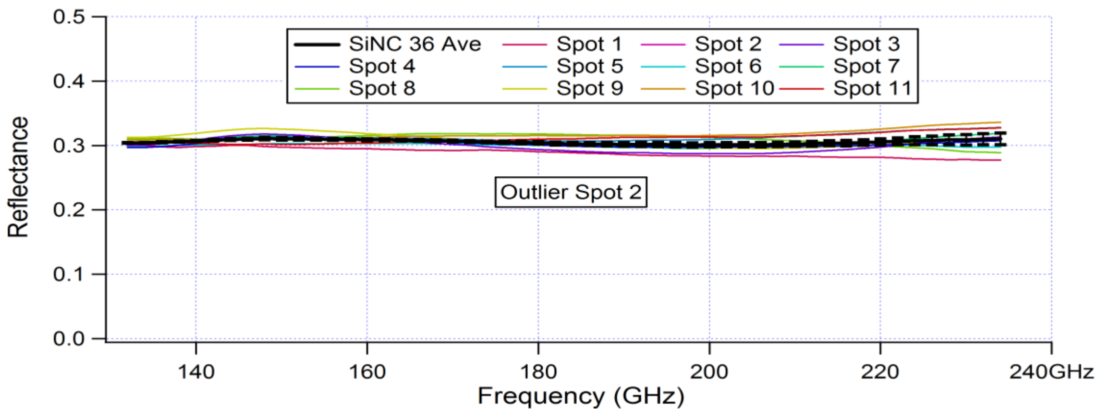

Figure A- 23: Baseline SiC/SiNC sample 36 (B94) 200 GHz 1st measure.

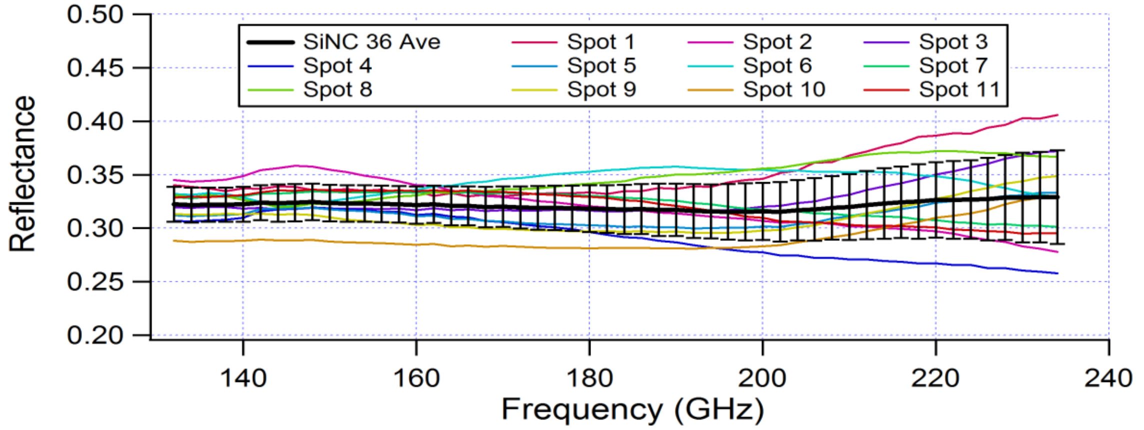

Figure A- 24: Baseline SiC/SiNC sample 36 (B94) 200 GHz 2nd measure

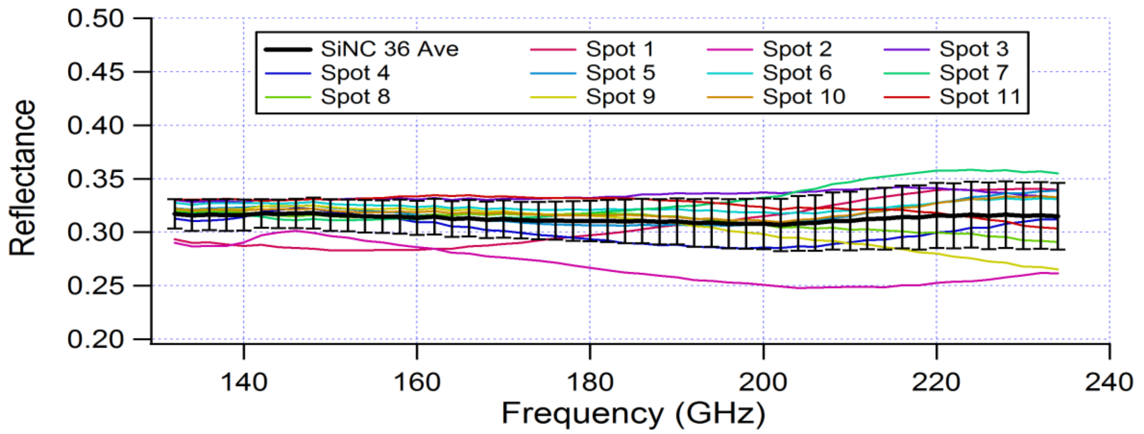

Figure A- 25: Baseline SiC/SiNC sample 36 (B94) 200 GHz 3rd measure

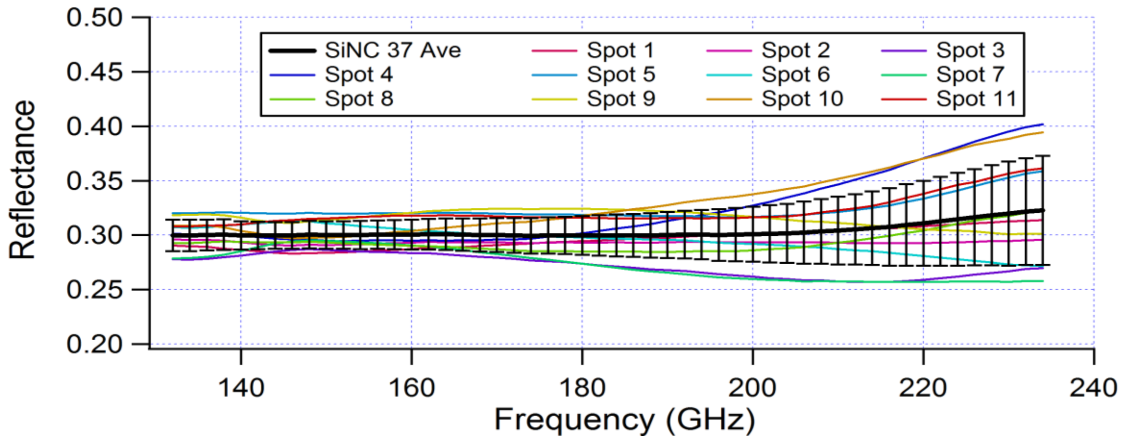

Figure A- 26: Baseline SiC/SiNC sample 37 (B95) 200 GHz 1st measure

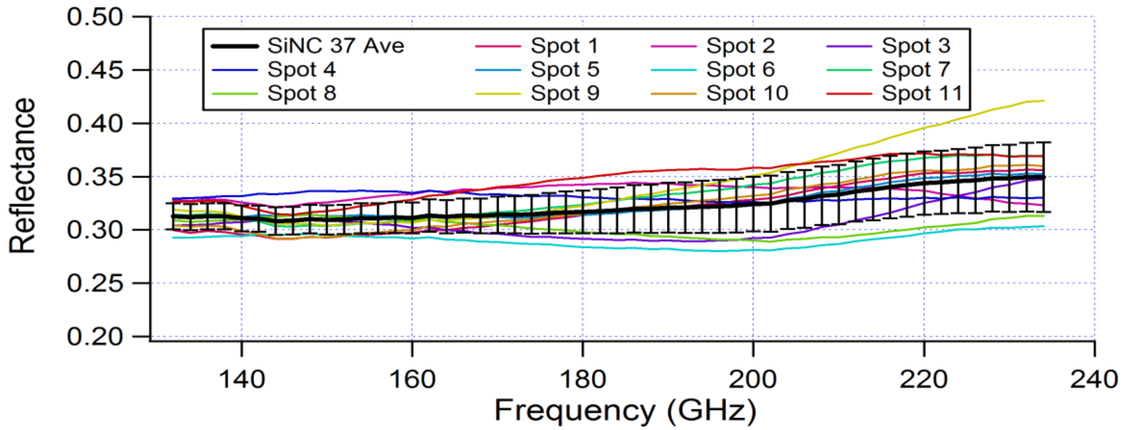

Figure A- 27: Baseline SiC/SiNC sample 37 (B95) 200 GHz 2nd measure

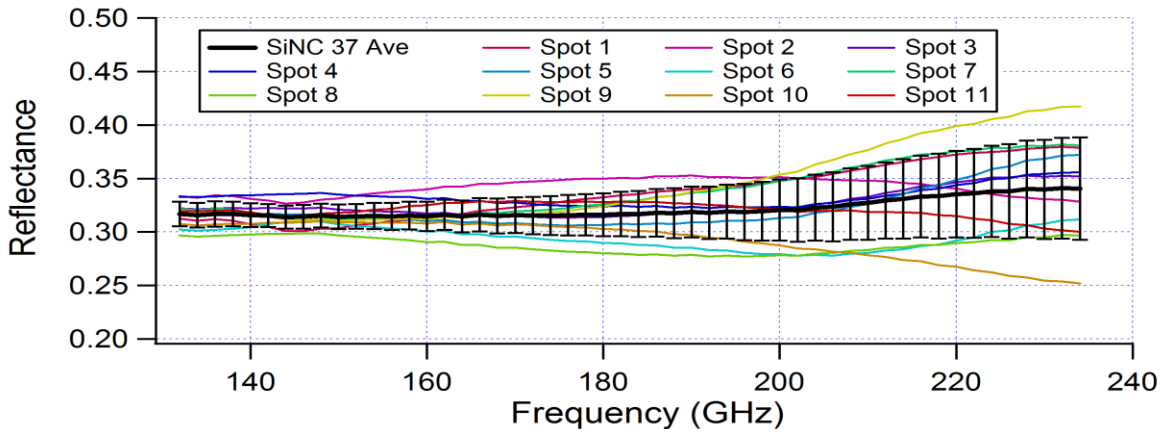

Figure A- 28: Baseline SiC/SiNC sample 37 (B95) 200 GHz 3rd measure

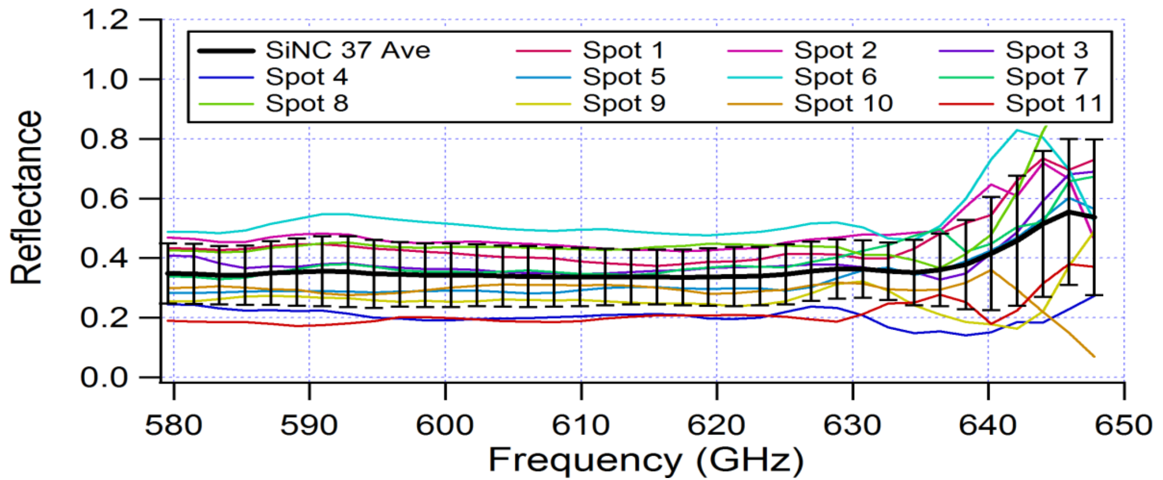

Figure A- 29: Baseline SiC/SiNC sample 37 (B95) 600 GHz

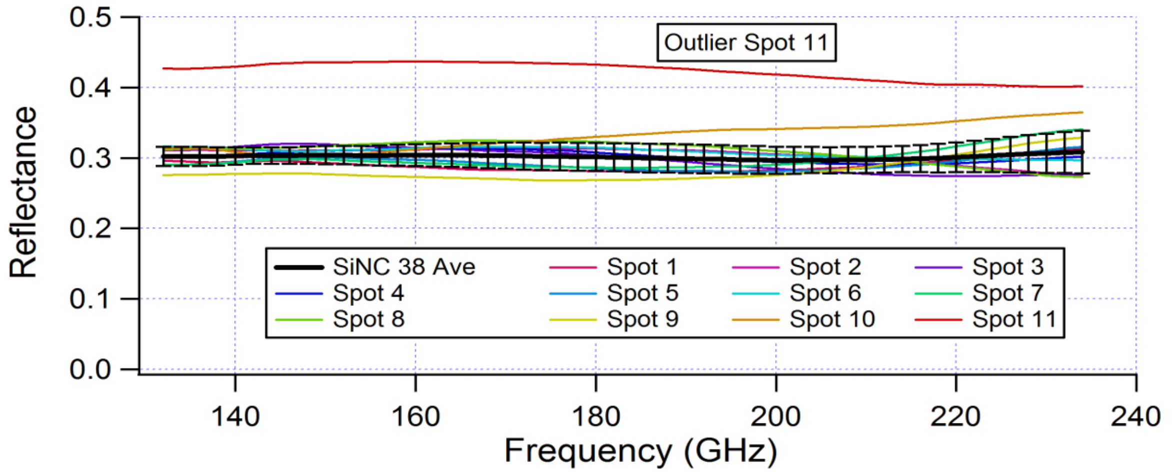

Figure A- 30: Baseline SiC/SiNC sample 38 (B96) 200 GHz 1st measure

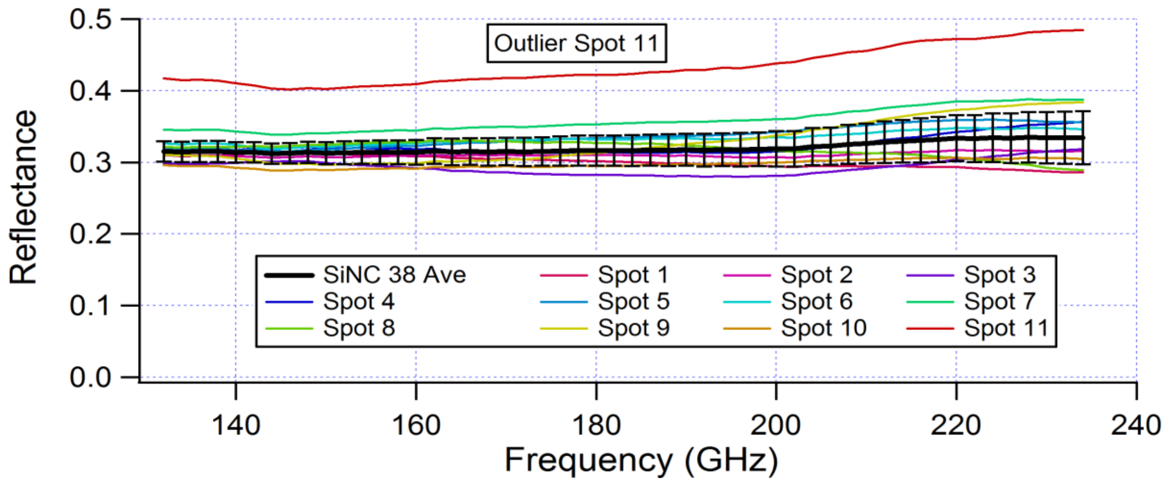

Figure A- 31: Baseline SiC/SiNC sample 38 (B96) 200 GHz 2nd measure

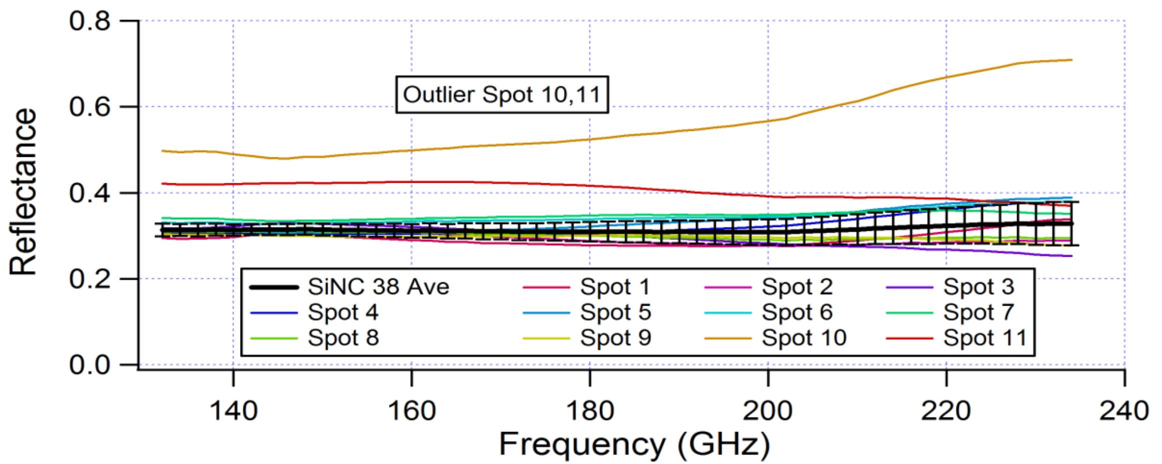

Figure A- 32: Baseline SiC/SiNC sample 38 (B96) 200 GHz 3rd measure

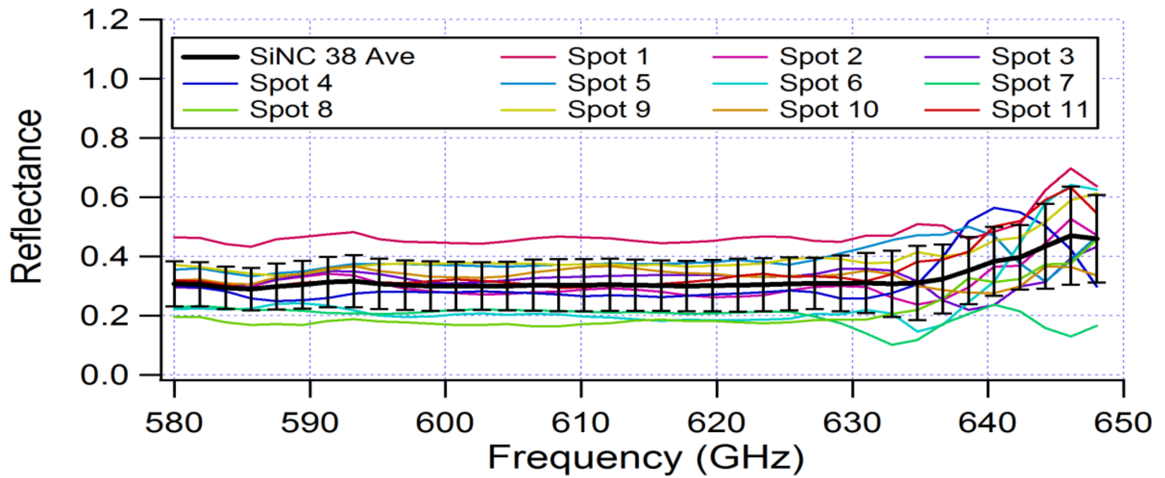

Figure A- 33: Baseline SiC/SiNC sample 38 (B96) 600 GHz

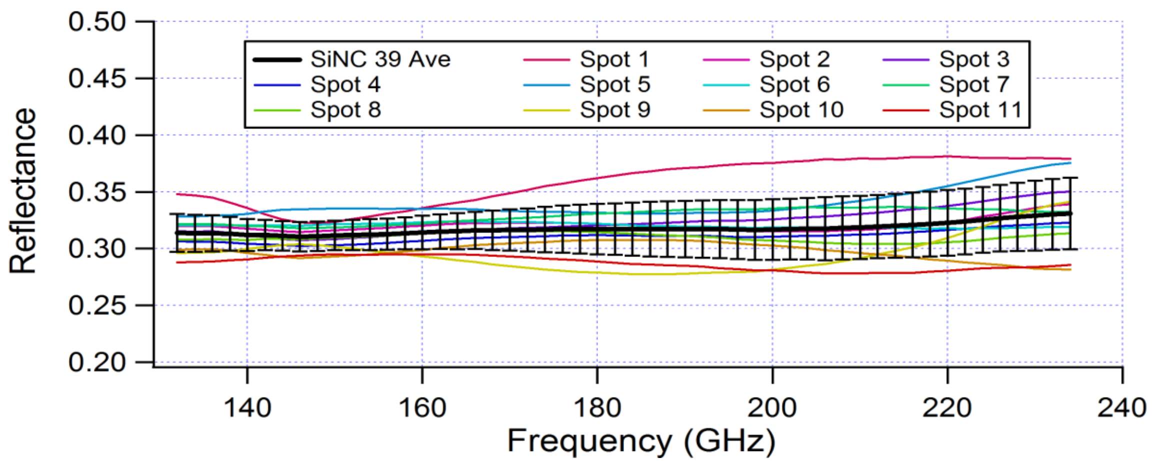

Figure A- 34: Baseline SiC/SiNC sample 39 (B97) 200 GHz 1st measure

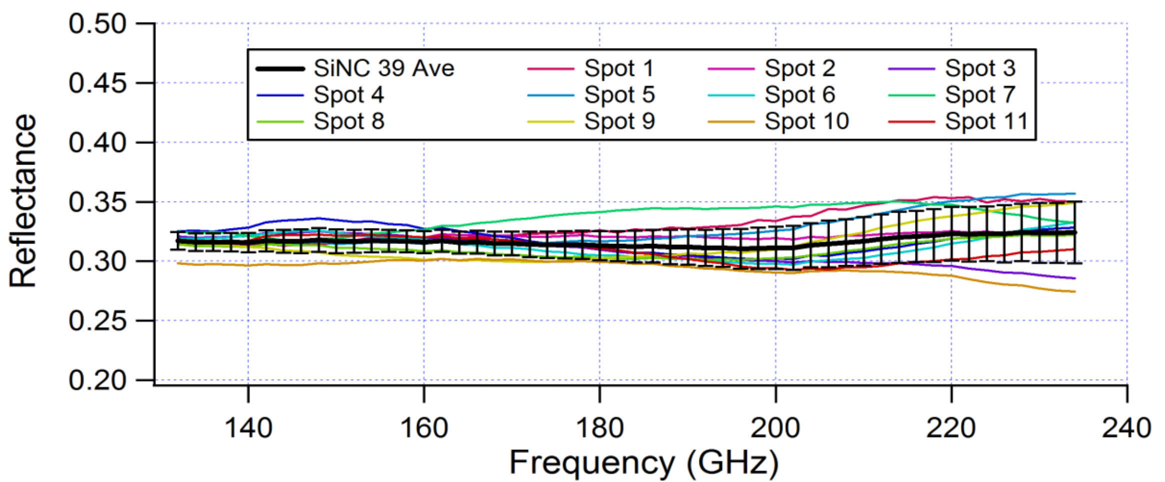

Figure A- 35: Baseline SiC/SiNC sample 39 (B97) 200 GHz 2nd measure

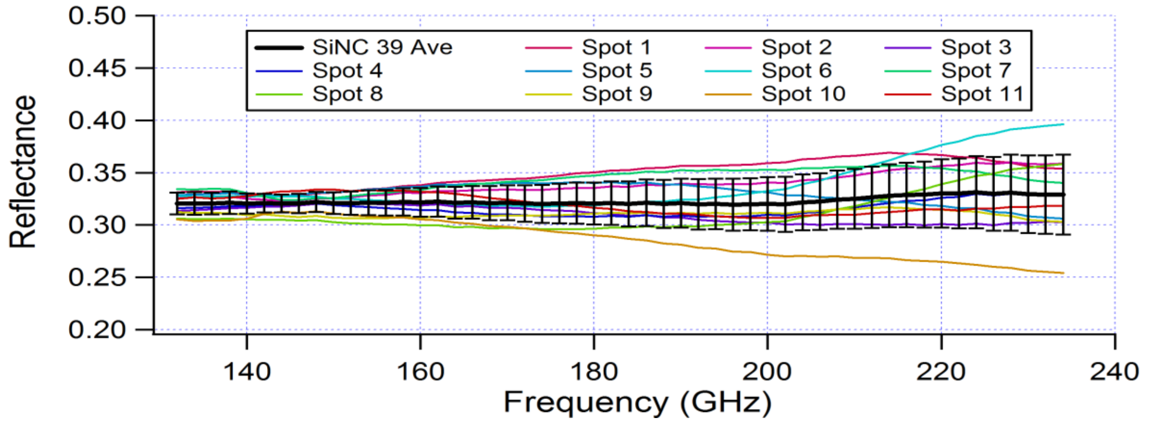

Figure A- 36: Baseline SiC/SiNC sample 39 (B97) 200 GHz 3rd measure

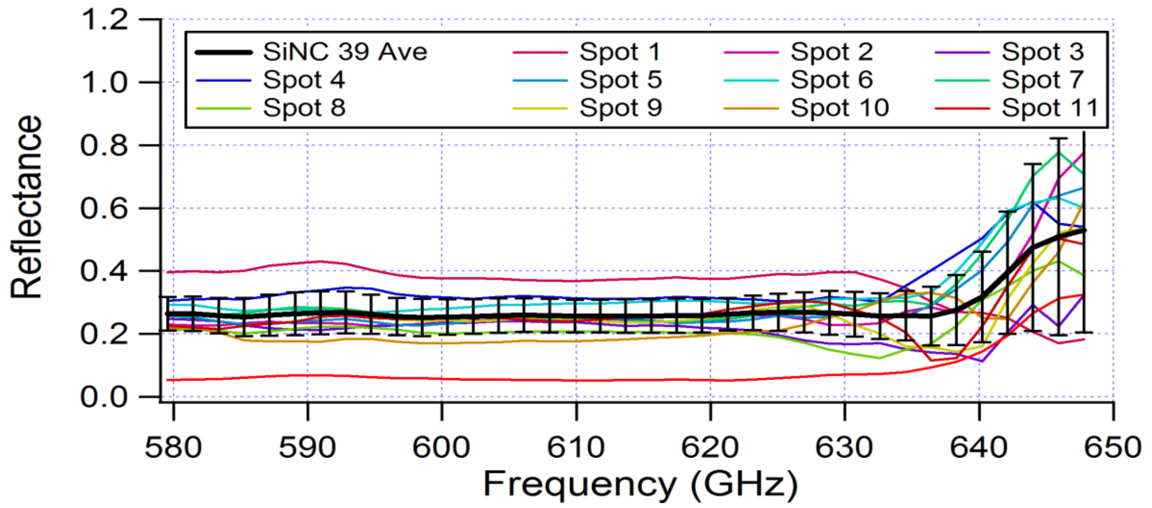

Figure A- 37: Baseline SiC/SiNC sample 39 (B97) 600 GHz

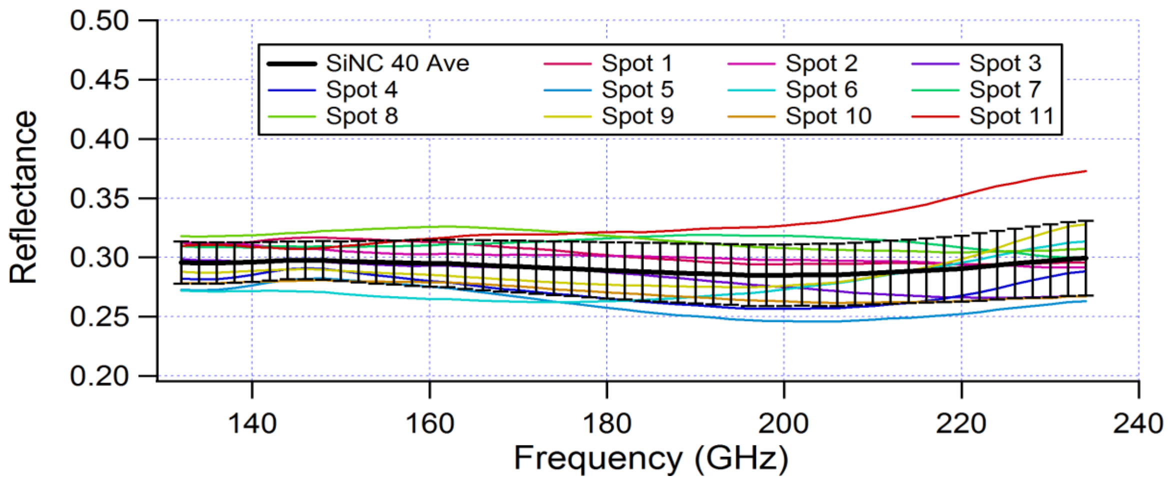

Figure A- 38: Baseline SiC/SiNC sample 40 (B98) 200 GHz 1st measure

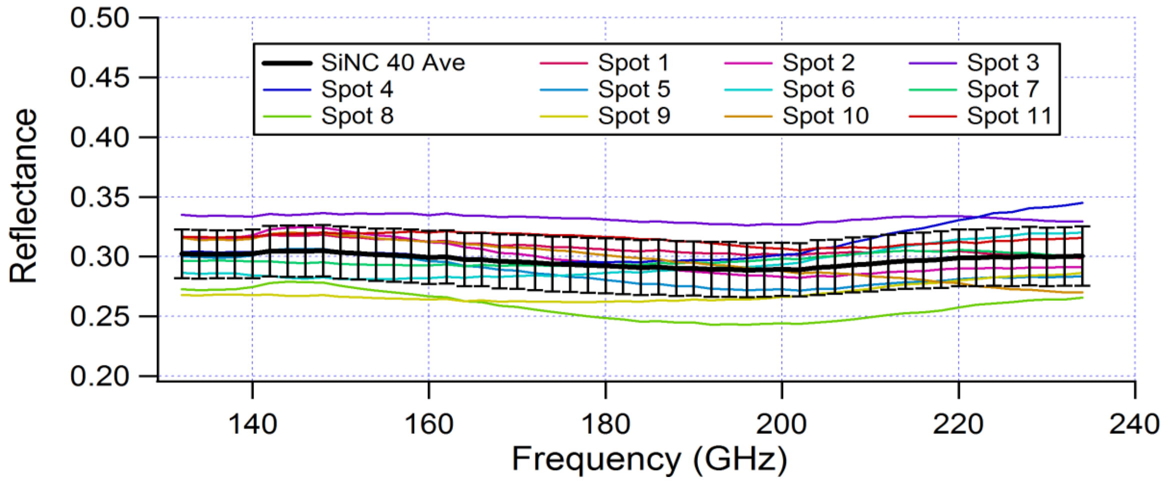

Figure A- 39: Baseline SiC/SiNC sample 40 (B98) 200 GHz 2nd measure

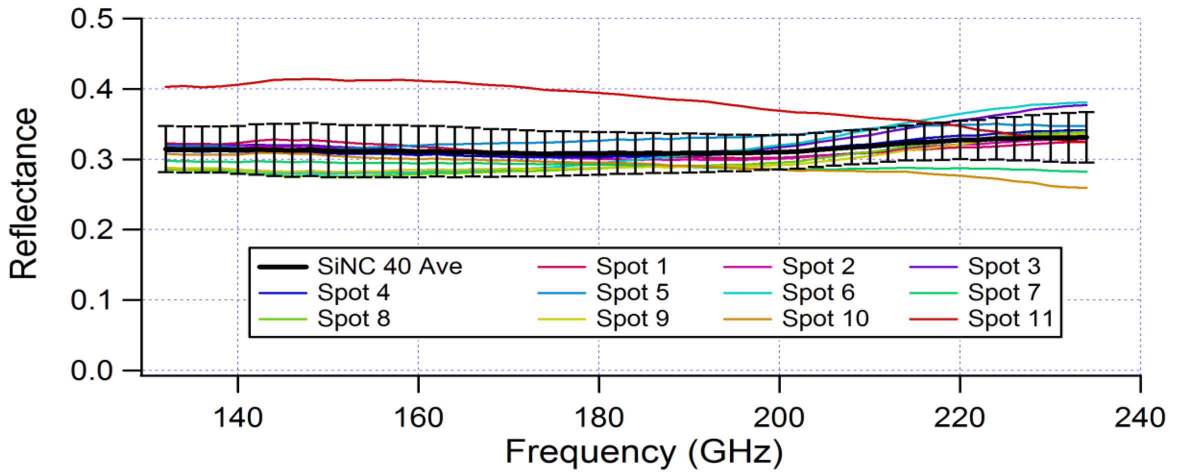

Figure A- 40: Baseline SiC/SiNC sample 40 (B98) 200 GHz 3rd measure

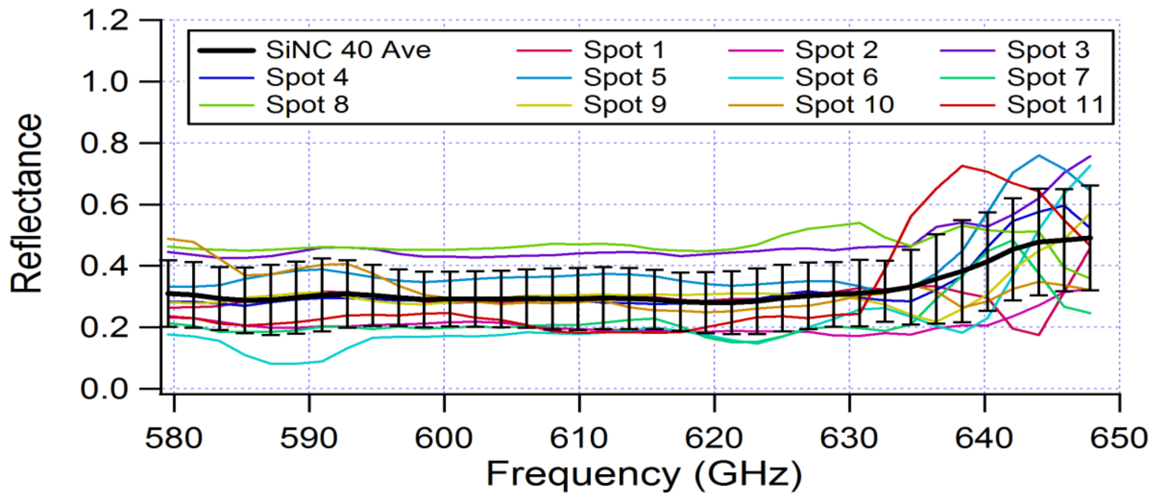

Figure A- 41: Baseline SiC/SiNC sample 40 (B98) 600 GHz

Oxide/Oxide CMC reflectance data

Baseline Oxide/Oxide 200 GHz fit results for the real index

	Measure number	Spot 1	Spot 2	Spot 3	Spot 4	Spot 5	Spot 6	Spot 7	Spot 8	Spot 9	Spot 10	Spot 11	Average by sample	St. Dev. by sample	St. Error
Sample 29	1	2.8511	2.7050	3.0160	3.0010	2.9790	2.9780	2.9690	2.9610	2.9390	2.9340	2.9490			
	2	2.8499	2.8565	2.8420	2.8283	2.8794	2.8274	2.8303	2.8427	2.8540	2.8716	2.9321	2.8953	0.0756	0.0161
Sample 30	1	2.8615	2.8501	2.8491	2.8084	2.7528	2.8188	2.8930	2.8601	2.8584	2.8713	2.9239	2.8498	0.0450	0.0136
Sample 31	1	2.8481	2.8321	2.8127	2.8146	2.7958	2.8402	2.8206	2.8609	2.8467	2.8492	2.9225	2.8403	0.0335	0.0101
Sample 32	1	2.8522	2.8423	2.8224	2.8073	2.7850	2.8470	2.8430	2.8494	2.8753	2.8946	2.9102			
	2	2.8462	2.8332	2.8147	2.8150	2.7900	2.8373	2.8439	2.8384	2.8663	2.8627	2.9033			
	3	2.8490	2.8340	2.8323	2.8157	2.8178	2.8326	2.8372	2.8490	2.8981	2.8540	2.8977	2.8454	0.0308	0.0054
Sample 33	1	2.8300	2.8195	2.8305	2.8249	2.8213	2.8341	2.8144	2.8514	2.8522	2.8587	2.8630			
	2	2.8129	2.8127	2.8524	2.8253	2.8411	2.8358	2.8254	2.8947	2.8592	2.8539	2.8612			
	3	2.8533	2.8351	2.8514	2.8520	2.8622	2.8639	2.8398	2.8981	2.8800	2.8823	2.8968			
	4	2.8483	2.8471	2.8577	2.8516	2.8650	2.8671	2.8372	2.9056	2.8720	2.8631	2.8869	2.8521	0.0237	0.0036
Sample 34	1		2.8276	2.8249	2.8253	2.8698	2.7935	2.8191	2.8359	2.8245	2.8171	2.8328			
	2	2.8083	2.7928	2.8228	2.8220	2.8730	2.8064	2.8251	2.8439	2.8419	2.8211	2.8261			
	3	2.8364	2.8329	2.8554	2.8130	2.8995	2.8389	2.8024	2.8199	2.8760	2.8455	2.8506			
	4	2.8336	2.8302	2.8581	2.8474	2.8857	2.8619	2.8447	2.8665	2.8659	2.8453	2.8476	2.8375	0.0239	0.0036
Sample 35	1	2.8399	2.8552	2.8531	2.8470	2.8673	2.8387	2.8028	2.7897	2.8031	2.9046	2.9425			
	2	2.8388	2.8495	2.8426	2.8507	2.8637	2.8348	2.7945	2.8232	2.7871	2.8873	2.9437			
	3	2.8178	2.8251	2.8259	2.8384	2.8524	2.8268	2.7691	2.7946	2.7913	2.8879	2.9345			
	4	2.8175	2.8243	2.8292	2.8413	2.8493	2.8161	2.7908	2.7640	2.7718	2.8852	2.8112	2.8369	0.0428	0.0065
Sample 36	1	2.8520	2.8333	2.8376	2.8158	2.8136	2.8269	2.8042	2.7743	2.8741	2.8829	2.8990			
	2	2.8702	2.8562	2.8638	2.8533	2.8428	2.8350	2.7943	2.8060	2.8828	2.9017	2.9321			
	3	2.8776	2.8530	2.8667	2.8452	2.8434	2.8474	2.8354	2.8011	2.9023	2.9104	2.9375			
	4	2.8623	2.8331	2.8355	2.8041	2.8251	2.8393	2.8246	2.7871	2.8668	2.8911	2.9096	2.8511	0.0383	0.0058
Sample 37	1	2.8385	2.8664	2.8404	2.8676	2.8604	2.8323	2.8396	2.8537	2.8360	2.8935	2.9188			
	2	2.8383	2.8559	2.8333	2.8690	2.8616	2.8296	2.8382	2.8486	2.8237	2.8807	2.9033			
	3	2.8243	2.8410	2.8376	2.8520	2.8453	2.8072	2.8242	2.8329	2.8346	2.8610	2.8664			
	4	2.8190	2.8230	2.8535	2.8454	2.8450	2.8170	2.8214	2.8288	2.8260	2.8461	2.8451	2.8461	0.0229	0.0035
Sample 38	1	2.8438	2.8328	2.8365	2.8335	2.8542	2.8444	2.8596	2.8111	2.8738	2.8565	2.8932			
	2	2.8480	2.8364	2.8563	2.8381	2.8463	2.8476	2.8613	2.8043	2.8768	2.8733	2.9032			
	3	2.8642	2.8607	2.8763	2.8550	2.8618	2.8600	2.8767	2.8172	2.8970	2.8855	2.9316			
	4	2.8660	2.8629	2.8779	2.8742	2.8768	2.8667	2.8628	2.8239	2.8971	2.8974	2.9243	2.8624	0.0271	0.0041
Sample 39	1	2.8559	2.8636	2.8647	2.8716	2.8785	2.8757	2.8452	2.8858	2.8814	2.8551	2.9120			
	2	2.8628	2.8483	2.8468	2.8649	2.9103	2.8705	2.7249	2.8413	2.8492	2.9213	2.6591			
	3	2.8610	2.8832	2.8762	2.8910	2.9107	2.8987	2.8730	2.9285	2.9165	2.8785	2.9137			
	4	2.8602	2.8808	2.8907	2.8947	2.9138	2.8931	2.8624	2.9169	2.9033	2.8714	2.5783	2.8656	0.0643	0.0097
Sample 40	1	2.8434	2.8541	2.8480	2.8276	2.8502	2.8435	2.8418	2.8843	2.9007	2.8771	2.9075			
	2	2.8574	2.8678	2.8538	2.8257	2.8460	2.8446	2.8577	2.8889	2.8703	2.8493	2.8975			
	3	2.8837	2.8779	2.8911	2.8740	2.8704	2.8735	2.8700	2.9096	2.8925	2.8975	2.5915			
	4	2.8776	2.8921	2.8781	2.8535	2.8773	2.8684	2.8811	2.9210	2.9025	2.8992	2.6047	2.8596	0.0620	0.0094

Table A- 1: Fitted baseline Oxide/Oxide CMC data from the 200 GHz system

Heat treated Oxide/Oxide 200 GHz fit results for the real index

	Measure number	Spot 1	Spot 2	Spot 3	Spot 4	Spot 5	Spot 6	Spot 7	Spot 8	Spot 9	Spot 10	Spot 11	Average by sample	St. Dev. by sample	St. Error
2nd Heat treat	1	2.7668	2.8187	2.8292	2.8720	2.8766	2.8980	2.9106	2.9534	3.0126	3.0478	3.1323	2.9198	0.1085	
	2	2.7566	2.8176	2.8315	2.8755	2.8745	2.9070	2.9218	2.9528	3.0104	3.0586	3.1318	2.9216	0.1107	
													2.9207	**0.1070**	**0.0228**
1st Heat treat	1	2.8750	2.8766	2.8638	2.8766	2.8857	2.8619	2.8762	2.8697	2.9019	2.8746	2.9361	2.8816	0.0210	
	2	2.8686	2.8712	2.8657	2.8649	2.8970	2.8762	2.8781	2.8898	2.9151	2.9229	2.9416	2.8901	0.0261	
													2.8859	**0.0235**	**0.0050**

Table A- 2: Fitted stressed Oxide/Oxide data 200 GHz

Oxide/Oxide Fitting 600 GHz for Baseline Samples

	real index values found from:	Spot 1	Spot 2	Spot 3	Spot 4	Spot 5	Spot 6	Spot 7	Spot 8	Spot 9	Spot 10	Spot 11	Average by sample	St. Dev. by sample	St. Error
Sample 34	Trans. Data	2.3611	2.6211	2.3102	2.2696	2.5952	2.3423	2.2663	2.3850	2.3648	2.5724	2.5655	2.4230	0.1369	
Sample 35	Trans. Data	2.8992	3.0165	2.7112	2.6552	2.6300	2.6775	2.6306	2.6426	2.8294	2.8351	2.8595	2.7624	0.1316	
Sample 37	Trans. Data	2.3547	2.4803	2.5669	2.6285	2.5320	2.5119	2.5431	2.5267	2.5382	2.5882	2.5645	2.5305	0.0703	
Sample 38	Trans. Data	2.5693	2.7974	2.6823	2.7734	2.5997	2.6064	2.6490	2.7206	2.3822	2.5498	2.8303	2.6509	0.1297	
Sample 39	Trans. Data	2.5152	2.3997	2.6902	2.5410	2.5294	2.5810	2.5267	2.5712	2.8229	2.7122	2.6343	2.5931	0.1155	
Sample 40	Trans. Data	2.6365	2.5646	2.4770	2.6536	2.8504	2.7485	2.7379	2.5341	2.5566	2.8245	2.6084	2.6538	0.1221	
	Ave. by Spot:	2.5560	2.6466	2.5730	2.5869	2.6228	2.5779	2.5589	2.5634	2.5824	2.6804	2.6771			
	St. Dev. by Spot:	0.2023	0.2261	0.1569	0.1723	0.1184	0.1412	0.1626	0.1141	0.2044	0.1288	0.1330	2.6023	0.1573	0.0194
Sample 34	Refl. Data	2.7156	2.6616	2.6656	2.4971	2.6519	2.6374	2.6408	2.7383	2.4051	2.4772	2.6781	2.6153	0.1065	
Sample 35	Refl. Data	2.7208	2.7463	2.7169	2.6192	2.7541	2.7211	2.7123	2.9465	2.7792	2.8076	2.9108	2.7668	0.0932	
Sample 37	Refl. Data	2.6112	2.4170	2.7886	2.5604	2.5919	2.5971	2.6209	2.6167	2.6788	2.7171	2.6907	2.6264	0.0959	
Sample 38	Refl. Data	2.7177	2.7209	2.7147	2.7189	2.7125	2.7145	2.7207	2.6247	2.6502	2.5588	2.6439	2.6816	0.0544	
Sample 39	Refl. Data	2.4436	2.6480	2.6140	2.5651	2.6156	2.5674	2.4650	2.4837	2.6410	2.6263	2.6261	2.5723	0.0748	
Sample 40	Refl. Data	2.5990	2.6246	2.5995	2.5987	2.5882	2.5779	2.6126	2.5848	2.5568	2.6242	2.6198	2.5987	0.0211	
	Ave. by Spot:	2.6347	2.6364	2.6832	2.5932	2.6524	2.6359	2.6287	2.6658	2.6185	2.6352	2.6949			
	St. Dev. by Spot:	0.1088	0.1168	0.0712	0.0743	0.0680	0.0678	0.0924	0.1599	0.1267	0.1161	0.1094	2.6435	0.1004	0.0124
													Set Ave:	Set St. Dev:	Set St. Err:
													2.6229	0.1331	0.0116

Table A- 3: Fitted baseline Oxide/Oxide CMC data from the 600 GHz system

Treatment		Spot 1	Spot 2	Spot 3	Spot 4	Spot 5	Spot 6	Spot 7	Spot 8	Spot 9	Spot 10	Spot 11	*Average by Sample*	*St. Dev. by Sample*	*St. Error*
Heat treated	Trans. data	2.7678	2.7049	2.7566	2.7606	2.3875	2.3844	2.7235	2.6153	2.8871	2.7589	2.5823	2.6663	0.1601	
Heat treated	Ref. data	2.8280	2.6731	2.8008	2.7889	2.7318	2.7922	2.7565	2.6378	2.8905	2.3097	2.625	2.7122	0.1563	
													2.6892	**0.1562**	*0.0142*
Strain treated	Trans. data	2.4515	2.5652	2.6525	2.5369	2.5285	2.4523	2.515	2.5891	2.4579	2.4908	2.5204	2.5236	0.0621	
Strain treated	Ref. data	2.6120	2.6029	2.6712	2.6510	2.6593	2.6469	2.624	2.5938	2.5586	2.6272	2.636	2.6257	0.0326	
													2.5747	**0.0712**	*0.0065*
Dwell treated	Trans. data	2.5211	2.6468	2.658	2.6226	2.6888	2.4793	2.6793	2.7093	2.5556	2.6549	2.6182	2.6213	0.0730	
Dwell treated	Ref. data	2.5557	2.692	2.7615	2.7719	2.7619	2.7781	2.74	2.8016	2.616	2.7701	2.7461	2.7268	0.0761	
													2.6740	**0.0906**	*0.0082*

Table A- 4: Fitted stressed Oxide/Oxide 600 GHz

Oxide/Oxide index fit result (from CW400 data)

	Spot 4	Spot 5	Spot 6	Spot 7	Spot 8	Spot 9	Spot 10	Set Ave.	Set St. Dev.
Heat treat -200 GHz	2.681	2.6894	2.6733	2.8002	2.7932			2.7274	0.0284
Heat treat -600 GHz	2.8013	2.8408	2.8367	2.8001	2.8713			2.83	0.0134
Strain treat -200 GHz		2.799	2.8002	2.9146	2.8696			2.8459	0.0253
Strain treat -600 GHz		2.7999	2.8788	2.8189	2.7993			2.8242	0.0168
Dwell treat -200 GHz	2.9106	2.9039	2.8738	2.8795	2.843	2.819	2.8335	2.8588	0.0131
Dwell treat -600 GHz	2.8187	2.8201	2.7995	2.79	2.7723	2.76	2.7681	2.785	0.0092
Sample 34 -200 GHz			2.8234	2.8479	2.8545	Baseline ~200 GHz		2.8666	0.0453
Sample 34 -600 GHz			2.7847	2.7967	2.7995	Baseline ~600 GHz		2.7984	0.0212
Sample 35 -200 GHz			2.8952						
Sample 35 -600 GHz			2.7649						
Sample 37 -200 GHz			2.8394						
Sample 37 -600 GHz			2.7988						
Sample 38 -200 GHz			2.8285						
Sample 38 -600 GHz			2.7987						
Sample 39 -200 GHz			2.9599						
Sample 39 -600 GHz			2.8408						
Sample 40 -200 GHz			2.884						
Sample 40 -600 GHz			2.8031						

Table A- 5: CW400 fit data for the Oxide/Oxide material.

Oxide/Oxide 200 GHz Baseline Reflectance

	Reflectance:		Real part of index			
	Value	St. Dev:	Ave:	St. Dev:	Kappa:	0.0111
Sample 29	0.2367	0.0021	2.8953	0.0161		
Sample 30	0.2309	0.0018	2.8498	0.0136		
Sample 31	0.2296	0.0013	2.8403	0.0101		
Sample 32	0.2303	0.0007	2.8454	0.0054		
Sample 33	0.2312	0.0005	2.8521	0.0036		
Sample 34	0.2293	0.0005	2.8375	0.0036		
Sample 35	0.2292	0.0008	2.8369	0.0065		
Sample 36	0.2310	0.0008	2.8511	0.0058		
Sample 37	0.2304	0.0005	2.8461	0.0035		
Sample 38	0.2325	0.0005	2.8624	0.0041		
Sample 39	0.2329	0.0013	2.8656	0.0097		
Sample 40	0.2321	0.0012	2.8596	0.0094		
Set Average	0.2314	0.0118				

Table A- 6: Oxide/Oxide baseline reflectance values 200 GHz

Oxide/Oxide 600 GHz Baseline						
	Reflectance:		Real part of index			
	Value	St. Dev:	Ave:	St. Dev:	Kappa:	0.0111
Sample 34	0.1864	0.0046	2.5192	0.0330		
Sample 35	0.2197	0.0031	2.7646	0.0237		
Sample 37	0.1946	0.0028	2.5784	0.0204		
Sample 38	0.2066	0.0028	2.6663	0.0210		
Sample 39	0.1952	0.0028	2.5827	0.0204		
Sample 40	0.2011	0.0026	2.6263	0.0192		
Set Average	**0.2006**	**0.0188**	2.6229	0.0120		

Table A- 7: Oxide/Oxide baseline reflectance values 600 GHz

CW400 Fitting for the Real Index Results									
	Spot 4	Spot 5	Spot 6	Spot 7	Spot 8	Spot 9	Spot 10	Set Ave.	Set St. Dev.
Heat treat -200 GHz	2.6810	2.6894	2.6733	2.8002	2.7932			**2.7274**	**0.0284**
Strain treat -200 GHz		2.7990	2.8002	2.9146	2.8696			**2.8459**	**0.0253**
Dwell treat -200 GHz	2.9106	2.9039	2.8738	2.8795	2.8430	2.8190	2.8335	**2.8588**	**0.0131**
Baseline -200 GHz			2.8717	2.8479	2.8545			**2.8666**	**0.0453**
	Spot 4	Spot 5	Spot 6	Spot 7	Spot 8	Spot 9	Spot 10		
Heat treat -600 GHz	2.8013	2.8408	2.8367	2.8001	2.8713			**2.8300**	**0.0134**
Strain treat -600 GHz		2.7999	2.8788	2.8189	2.7993			**2.8242**	**0.0168**
Dwell treat -600 GHz	2.8187	2.8201	2.7995	2.7900	2.7723	2.7600	2.7681	**2.7850**	**0.0092**
Baseline -600 GHz			2.7985	2.7967	2.7995			**2.7984**	**0.0212**

Table A- 8: Oxide/Oxide baseline reflectance values CW400 system

Appendix B.

Derivation of the Transmission and Reflection model for a thin dielectric film with thickness on the order of λ

It was originally thought that Abele's paper on the matrix method of thin film optics would describe the interference models described in chapter 2 of this thesis[1]. Further research into this paper on the reflections and transmission of thin films reveals that assumptions made in that paper rapidly degrade for films greater than λ/10 in thickness. By using this thin film approximation Abele's presentation was able to avoid the phase difference at the front and rear material surface. Realizing this model would not be sufficient further research eventually brought a paper by Girard and Delisle to light [11]. This paper describes the case of monochromatic radiation onto a material where the material thickness and wavelength are of the same order [11]. This paper also proceeds to discuss the case of a non-monochromatic source. Monochromatic light is the assumption that only one frequency is propagating in the material at a time. Our work made use of a swept frequency, but the sweep time was such that the coherence time meets this criterion by several orders of magnitude. Reference (11) assumes that a plane wave is propagating in the material. As noted in the thesis, this was valid approximation for the 200 GHz system but was not for the 600 GHz system (when comparing the thickness of the material to the Rayleigh range of the Gaussian beam). To use one model for all Oxide/Oxide spectra gathered for this thesis the power coupling coefficient was introduced to explain the variations in the etalon amplitude from the different optical systems. Adding this coupling coefficient to the multiple reflection / transmission model successfully described the differences between the Oxide/Oxide spectra's gathered with the different optical systems. With these caveats, the presentation of the derivation of the Fresnel equations to these models mirrors the derivation by Girard and Delisle, and will show how the models derived here are the same as presented in the thesis.

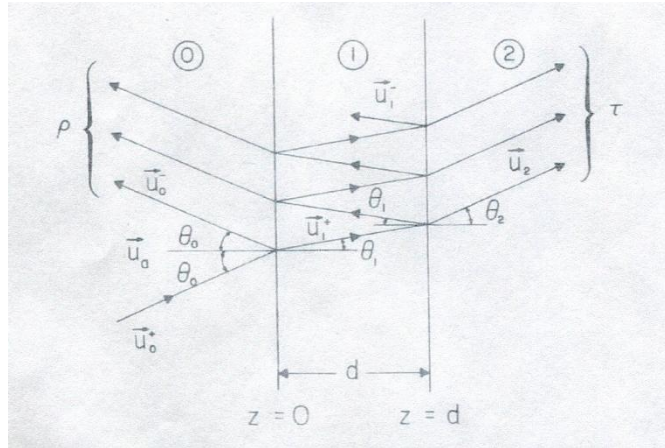

Figure B- 2: Image of problem materials 0, and 2 are air, material 1 is the absorbing dielectric.

The electric fields in the different regions of this material are as follows:

$$E_i = E_0^+ e^{[i(k_0 u_0^+ * r - \omega t')]} \qquad H_i = \frac{k_0}{\omega \mu_0} u_0^+ \times E_i \qquad \text{Eqn. B-1}$$

$$E_r = E_0^- e^{[i(k_0 u_0^- * r - \omega t')]} \qquad H_r = \frac{k_0}{\omega \mu_0} u_0^- \times E_r \qquad \text{Eqn. B-2}$$

$$E_1^+ = E_1^+ e^{[i(k_0 u_1^+ * r - \omega t')]} \qquad H_1^+ = \frac{k_1}{\omega \mu_1} u_1^+ \times E_1^+ \qquad \text{Eqn. B-3}$$

$$E_1^- = E_1^- e^{[i(k_0 u_1^- * r - \omega t')]} \qquad H_1^- = \frac{k_1}{\omega \mu_1} u_1^- \times E_1^- \qquad \text{Eqn. B-4}$$

$$E_t = E_2 e^{[i(k_2 u_2 * r - \omega t')]} \qquad H_t = \frac{k_2}{\omega \mu_2} u_2 \times E_t \qquad \text{Eqn. B-5}$$

At the interfaces Snell's law of reflection and refraction is:

$$\hat{n}_i \sin\theta_i = \hat{n}_j \sin\theta_j \text{ for } i,j = 0,1,2 \qquad \text{Eqn. B-6}$$

The vector field amplitudes must satisfy the boundary conditions. These measurements were made with a transverse electric wave with all systems thus $A_j = E_j$, where A is the modulus of the field vector. At z = 0, i.e. the 0 to 1 interface:

$$u \times (A_0^+ + A_0^-) = u \times (A_1^+ + A_1^-) \qquad \text{Eqn. B-7}$$

Similarly at the z = d, i.e. the 1 to 2 interface the following equation is:

$$u \times \left(A_1^+ \exp\left(i\frac{2\pi\widehat{N_1}}{\lambda}\right) + A_0^- \exp\left(-i\frac{2\pi\widehat{N_1}}{\lambda}\right)\right) = u \times A_2 \exp\left(i\frac{2\pi\widehat{N_2}}{\lambda}\right) \qquad \text{Eqn. B-8}$$

Where $\widehat{N}_j = n_j \cos\theta_j$ and n_j is the complex index of refraction. As these systems made use of normal incidence this relation reduces to: $\widehat{N}_j = n_j$. With this development the two boundary equations have forms like $u_a \cdot u_j$ which can be reduced to the form $u_a \cdot u_j = s$ where $j=0,1,2$. In this equation $s = \pm 1$ depending on if u_j is in the direction of u_a. These above relations reduce to:

$$A_0^+ + A_0^- = A_1^+ + A_1^- \qquad \text{Eqn. B-9}$$

$$(A_0^+ - A_0^-)s_0 = (A_1^+ - A_1^-)s_1 \qquad \text{Eqn. B-10}$$

$$A_1^+ \exp\left(i\frac{2\pi\widehat{N_1}}{\lambda}\right) + A_0^- \exp\left(-i\frac{2\pi\widehat{N_1}}{\lambda}\right) = A_2 \exp\left(i\frac{2\pi\widehat{N_2}}{\lambda}\right) \qquad \text{Eqn. B-11}$$

$$\left(A_1^+ \exp\left(i\frac{2\pi\widehat{N_1}}{\lambda}\right) + A_0^- \exp\left(-i\frac{2\pi\widehat{N_1}}{\lambda}\right)\right) \times s_1 = \left[A_2 \exp\left(i\frac{2\pi\widehat{N_2}}{\lambda}\right)\right] s_2 \qquad \text{Eqn. B-12}$$

The relations of the reflectance and transmittance from the measured material properties can be written as:

$$r = \frac{A_0^-}{A_0^+} \qquad t = \frac{A_2}{A_0^+} \qquad \text{Eqn. B-13}$$

Using the Fresnel equations at the interface:

$$r_{ij} = \frac{\widehat{N}_i \cos\theta_i - \widehat{N}_j \cos\theta_j}{\widehat{N}_i \cos\theta_i + \widehat{N}_j \cos\theta_j} \qquad t_{ij} = \frac{2\widehat{N}_i \cos\theta_i}{\widehat{N}_i \cos\theta_i + \widehat{N}_j \cos\theta_j} \qquad \text{Eqn. B-14}$$

Where: $i=0,1$ $\qquad j=i+1$

Note that $r_{ij} = -r_{ij}$ corresponds to a phase change of π when the incident beam moves from *j* to *i* we can therefore represent r_{ij} as:

$$r_{ij} = |r_{ij}| \exp\left(i\delta_{ij}\right) \qquad \text{Eqn. B-16}$$

$$\text{Where: } \delta_{ji} = \delta_{ij} + \pi$$

In this δ_{ij} is the phase change on reflection. The left-hand side equations have the N_j designation. The right-hand side equations assume normal incidence on the sample, a complex index for material 1, and non-absorbing material for materials 0, and 2 with a real index of 1. Similar equations are found in Born and Wolf's discussion of propagation in a homogeneous dielectric [4].

$$r = \frac{r_{01} + r_{12}\exp\frac{i4\pi d\hat{N}_1}{\lambda}}{1 + r_{01}r_{12}\exp\frac{i4\pi d\hat{N}_1}{\lambda}} = \frac{r_{01} + r_{12}\exp\frac{i4\pi d(n_1 - i\kappa_1)}{\lambda}}{1 + r_{01}r_{12}\exp\frac{i4\pi d(n_1 - i\kappa_1)}{\lambda}} \quad \text{Eqn. B-17}$$

$$t = \frac{t_{01}t_{12}\exp\frac{i4\pi d(\hat{N}_1 - \hat{N}_2)}{\lambda}}{1 + r_{01}r_{12}\exp\frac{i4\pi d\hat{N}_1}{\lambda}} = \frac{t_{01}t_{12}\exp\frac{i4\pi d((n_1 - i\kappa_1) - 1)}{\lambda}}{1 + r_{01}r_{12}\exp\frac{i4\pi d(n_1 - i\kappa_1)}{\lambda}} \quad \text{Eqn. B-18}$$

The material reflectance and transmittance can be written in the following forms:

$$\rho_\lambda = \left|\frac{\Phi_r}{\Phi_i}\right| = \frac{Re\int_a (u \cdot S_r)da}{Re\int_a (u \cdot S_i)da} = \left|\frac{Re(u \cdot S_r)}{Re(u \cdot S_i)}\right| = \left|\frac{(A_0^- \cdot A_0^{-*})}{(A_0^+ \cdot A_0^{+*})}\frac{(u_a \cdot u_0^-)}{(u_a \cdot u_0^+)}\right| = \left(\frac{A_0^-}{A_0^+}\right)\left(\frac{A_0^-}{A_0^+}\right)^* = rr^* \quad \text{Eqn. B-19}$$

$$t_\lambda = \left|\frac{\Phi_t}{\Phi_i}\right| = \frac{Re\int_a (u \cdot S_t)da}{Re\int_a (u \cdot S_i)da} = \left|\frac{Re(u \cdot S_t)}{Re(u \cdot S_i)}\right| = \left|\frac{(A_2 \cdot A_2^*)}{(A_0^+ \cdot A_0^{+*})}\frac{Re[s_2(u_a \cdot u_2)]}{Re[s_0(u_a \cdot u_0^+)]}\right| = \left(\frac{A_2}{A_0^+}\right)\left(\frac{A_2}{A_0^+}\right)^* \frac{Re[s_2(u_a \cdot u_2)]}{Re[s_0(u_a \cdot u_0^+)]} = tt^* \quad \text{Eqn. B-20}$$

Using the preceding equations the following relations develop:

$$\rho_\lambda = \frac{\rho_{01} + 2T_1\sqrt{\rho_{01}\rho_{12}}\cos(2\beta n_1 + \delta_-) + \rho_{12}T_1^2}{1 + 2T_1\sqrt{\rho_{01}\rho_{12}}\cos(2\beta n_1 + \delta_+) + \rho_{01}\rho_{12}T_1^2} \qquad \text{Eqn. B-21}$$

$$\tau_\lambda = \frac{\tau_{01}\tau_{12}T_1}{T_2\left[1 + 2T_1\sqrt{\rho_{01}\rho_{12}}\cos(2\beta n_1 + \delta_+) + \rho_{01}\rho_{12}T_1^2\right]} \qquad \text{Eqn. B-22}$$

Assuming normal incidence the following simplifications are made:

$$\delta_\pm = \delta_{12} \pm \delta_{01} \qquad \beta = \frac{2\pi d}{\lambda}$$

$$T_j = \exp\left(\frac{-4\pi d\kappa_j}{\lambda}\right) \qquad \rho_{ij} = \frac{(n_i - n_j)^2 + (\kappa_i - \kappa_j)^2}{(n_i + n_j)^2 + (\kappa_i + \kappa_j)^2} \qquad \tau_{ij} = \frac{4(n_i^2 + \kappa_i^2)}{(n_i + n_j)^2 + (\kappa_i + \kappa_j)^2}$$

$$\delta_{ij} = \tan^{-1}\left[\frac{2(\kappa_i - \kappa_j)}{(n_i^2 + \kappa_i^2) - (n_j^2 + \kappa_j^2)}\right]$$

Further simplification is possible by assuming a non-absorbing material for materials 0 and 2:

$$\rho = \rho_{01} = \rho_{12} = \frac{(1 - n_1)^2 + (\kappa_1)^2}{(1 + n_1)^2 + (\kappa_1)^2} \quad \tau_{01} = \frac{4}{(1 + n_1)^2 + (\kappa_1)^2} \qquad \tau_{12} = \frac{4(n_1^2 + \kappa_1^2)}{(1 + n_1)^2 + (\kappa_1)^2}$$

$$\tau_{01}\tau_{12} = \frac{16(n_1^2+\kappa_1^2)}{(1+n_1)^2+\kappa_1^2} = \tau$$

$$T_1 = \exp\left(\frac{-4\pi d\kappa_1}{\lambda}\right) \quad T_2 = 1 \quad \delta = \tan^{-1}\left[\frac{2\kappa_1}{(n_1^2+\kappa_1^2)-1}\right] \quad \delta_- = 0 \quad \delta_+ = 2\delta$$

Adding these to our ρ_λ and τ_λ equations above the following equations develop:

$$\rho_\lambda = \frac{\rho+2T_1\sqrt{\rho^2}\cos(2\beta n_1)+\rho T_1^2}{1+2T_1\sqrt{\rho^2}\cos(2\beta n_1+2\delta)+\rho^2T_1^2} = \frac{2\,\rho\cos(2\beta n_1)+\rho(T_1+T_1^{-1})}{T_1^{-1}+2\rho\cos(2\beta n_1+2\delta)+\rho^2T_1} = \frac{2\,\rho(\cos(2\beta n_1)+\cosh(2\beta\kappa_1))}{T_1^{-1}+\rho^2T_1+2\rho\cos(2\beta n_1+2\delta)}$$

Eqn. B-21

$$\tau_\lambda = \frac{\tau_{01}\tau_{12}T_1}{T_2\left[1+2T_1\sqrt{\rho_{01}\rho_{12}}\cos(2\beta n_1+\delta_+)+\rho_{01}\rho_{12}T_1^2\right]} = \frac{\tau}{T_1^{-1}+\rho^2T_1+2\rho\cos(2\beta n_1+2\delta)}$$

Eqn. B-22

The intermediate step was to multiply the both of these equations by a T_1^{-1}enabling the reorganization of the reflectance to include a *cosh* term, and reduce the transmission term numerator to remove the exponential term. These reflectance and transmittance equations match those found as equations 6 and 7 in the thesis.

Bibliography

1. Abeles, F. “Optical Properties of Thin Absorbing Films”. J. of the Optical Society of America Vol. 47, No. 6, (473-482). 1957.

2. Baker-Jarvis, J. Vanzura, E.J. Kissick, W.A. “Improved Technique for Determining Complex Permittivity with the Transmission/Reflection Method”. IEEE Trans. On Microwave Theory and Techniques, Vol. 38 No. 8. 1990.

3. Blevington, P. Data Reduction and Error Analysis for the Physical Sciences. McGraw Hill. Boston, MA. 2003.

4. Born, M. Wolf E. Principles of Optics 5th ed. Pergamon Press. Oxford. 1975.

5. Boughriet, A. H. Legrand, C. Chapoton, A. “Non-iterative Stable Transmission/reflection Method for Low-Loss Material Complex Permittivity Determination”. IEEE Trans. On Microwave Theory & Tech. Vol. 45, No. 1 (52-57). 1997.

6. Chantry, G. W. Long-wave Optics Volume 1 Principles. Academic Press Inc. London. 1984.

7. Cooney, A. ‘AFRL-WSU-UD Technical Research Meeting’. December, 2nd 2011.

8. Department of Defense. DOD Handbook Composite Materials Handbook Vol. 5. Ceramic Matrix Composites. MIL-HDBK-17-5, Dist. A. June 17, 2002.

9. Devore, J.L. “Probability and Statistics for Engineering and the Sciences 6th ed.” Brooks/Cole-Thompson Learning. Belmont, CA. 2004.

10. Gatesman, A.J. Giles R.H. Waldman, J. “High-Precision Reflectometer for Submillimeter Wavelengths.” J. Opt. Soc. Am. B. Vol. 12 No. 2 (212-219) 1995.

11. Girard, A. Delisle, C. “Reflectance and Transmittance of one optical material”. Optica Acta Vol. 29 No. 5. (611-626). 1982.

12. Goldsmith, P. Quasioptical Systems. IEEE Press. New York. 1998.

13. Goldsmith, P. “Quasi-Optical Techniques.” Pro. of the IEEE, Vol. 80. No. 11 November, 1992.

14. Halbach, K. “Matrix Representation of Gaussian Optics” American J. of Physics. (90-108) 1963.

15. Heavens, O.S. Optical Properties of Thin Solid Films. Dover Books. New York. 1965.

16. Kogelnik, H. Li, T. “Laser Beams and Resonators.” Proceeding of the IEEE, Vol. 54, No. 10. October, 1966.

17. Ju, Y. Inoue, K. Saka, M. Abe, H. "Contactless Measurements of Electrical Conductivity of Semiconductor Wafers using the Reflection of Millimeter waves." Applied Physics Letters Vol. 81 No. 19. (3585-3587). 2002.

18. Latyshev, A. B. Semenov, A.V. "A New Method for Complex Spectral Measurements in Millimeter and Sub-Millimeter Wave Ranges." Int. J. of Infrared and Millimeter Waves. Vol. 15, No. 11 (1781-1807) 1994.

19. Li, Z. Sharma, A. Ayala. A M. Asfar, M N. Korolev, K A. "Broadband Dielectric Measurements on Highly Scattering Materials." IEEE Transactions on Instrumentation and Measurement. Vol. 59, No. 5 (1397-1405) 2010.

20. Manifacier, J.C. Gasiot, J. Fillard, J.P. "A simple method for the determination of the optical constants n, k and the thickness of a weakly absorbing thin film". J. of Physics E: Scientific Instruments Vol. 9 (1002-1004) 1976.

21. Martin, D. Bowen, J. "Long-Wave Optics." IEEE Transactions on Microwave Theory and Techniques, Vol. 41, No. 10. October, 1993.

22. Orfanidis, S.J. <u>Electromagnetic Waves and Antennas</u>. Web published at: www.ece.rutgers.edu/~orfanidi/ewa. Accessed July 18, 2012.

23. Petkie, D.T. Kemp, I.V. Benton, C. Boyer, C. Owens, L. Deibel, J.A. Stoik, C.D. Bohn, M.J. "Nondestructive terahertz imaging for aerospace applications", Proceedings of SPIE: Millimetre Wave and Terahertz Sensors and Technology, **7485** [7485-13] 2009.

24. Pisarkiewicz, T. Czapla, A. Czternastek, H. "Influence of thickness inhomogeneity on the determination of optical constants of amorphous silicon thin films". Applied Surface Science 65/66 511-514. North-Holland. 1993.

25. Pronin, A. V. Goncharov, Yu. G. Fischer, T. Wosnitza, J. "Phase-sensitive THz Spectroscopy with BWO in Reflection Mode." Rev. of Scientific Instruments. Vol. 80 No. 123904. 2009.

26. Siegman, A. <u>Lasers 1st ed</u>. University Science Books. Mill Valley, CA. 1986.

27. Stockel, B. "Quasi-Optical Measurement of Complex Dielectric Constant at 300 GHz." Int. J. of Infrared and Millimeter Waves. Vol. 14, No. 10 (2131-2148) 1993.

28. Swanepoel, R. "Determination of the thickness and optical constants of amorphous silicon". Journal Physics E: Scientific Instruments. Vol. 16 (1214-1222). 1983.

29. TeraView LTD. "CW Spectra 400 Datasheet.pdf". Accessed July, 2012 at www.teraview.com.

30. Tompkins H. G. McGahan, W.A. <u>Spectroscopic Ellipsometry and Reflectometry A User's Guide</u>. John Wiley and Sons, Inc. New York. 1999.

31. VDI. "Tech notes on feed horns". VDI Inc. July, 2010.

32. VDI Work Order Document. "VDI User Guide Product: 290-330 GHz & 580-660 GHz Frequency Extension Module". VDI Inc. July, 2006.

33. Ward, L. The Optical Properties of Bulk Materials and Films 2nd ed. Inst. of Physics. London. 1994.

34. Wolfe, P. "Error Analysis for Physics Laboratories A Self-Study Guide". Wright State University. Dayton, OH.

35. Bohren, C. Huffman, D. Absorption and Scattering of Light by Small Particles. Wiley. New York. 1983.